



東北大学

WPI-AIMR

Volume 2
NEWS
April 30, 2008

Creative Development
Atomistic Characterization
Theoretical Understanding
Innovative Processing
New Device / System



World Premier International
Research Center Initiative

World Premier International Research Center
Advanced Institute for Materials Research

Tohoku University

Volume 2
WPI-AIMR NEWS
April 30, 2008

World Premier International Research Center
Advanced Institute for Materials Research

Tohoku University



Produced by the WPI-AIMR Communication Office

Director: Yoshinori Yamamoto
Editor, writer: Toshio Sakurai
Associate Editor, writer: Hiroshi Komatsu
Production coordinator: Yasunori Fujikawa

We welcome your comments, questions and involvement.
e-mail to: wpi-office@bureau.tohoku.ac.jp, or
sakurai@imr.tohoku.ac.jp

Contents

Preface	2
Research Prospect	
1. A. Inoue (WPI-AIMR) and D. V. Louzguine-Luzgin (WPI-AIMR)	5
2. M. G. Lagally (WPI-AIMR and Univ. of Wisconsin-Madison)	21
3. K. Nakajima (WPI-AIMR)	27
4. T. Hitosugi (WPI-AIMR)	39
5. R. M. Tromp (WPI-AIMR and IBM Thomas J. Watson Research Center)	47
The Salient Point of Research	65
Interviews	
Yoshinori YAMAMOTO (WPI-AIMR)	95
Masashi KAWASAKI (WPI-AIMR)	101
Announcement	
Staff/post-doctoral fellowship	121
Ph. D. student scholarship	122
International workshop guidelines	123
Appendix	
WPI & IFCAM Joint Workshop snapshots	X-1



Prof. Yoshinori YAMAMOTO

機構長 山本 嘉則

Preface

The first international workshop of WPI-AIMR

It is a pleasure for me to be able to deliver volume 2 of WPI-AIMR News to you. WPI-AIMR was established on October 1, 2007, and about half a year passed so quickly. Already, excellent researchers in various disciplines including physics, chemistry, material sciences, and engineering are joining us from all over the world. Thirty PIs (principal investigators) of WPI-AIMR together with those excellent researchers have started their activities toward our goal, that is to say, through in-depth understanding and control at atomic and molecular level to promote the development of new materials and substances, to invent innovative processes and devices, and ultimately to benefit the society and mankind. In order to assist to gain access to the goal, we organize the first international WPI workshop “Challenge of Interdisciplinary Materials Science to Technological Innovation of the 21st Century”. A major purpose of this workshop is to find collaboration partners within the WPI framework or even beyond the WPI framework, because fusion and integration of the above disciplines are needed to make the goal feasible. We have four major research groups, physical metallurgy (bulk metallic glasses), nano-physics, nano-chemistry, and device/system development, and in the workshop PIs of those four thrusts, together with researchers and collaborators of WPI, present the state of the art of their accomplishments. I hope that you will learn in-depth the researches going on now in the disciplines different from your own specialty, and you will be able to find partners and collaborators in order to pursue integration and fusion of your own research.

We plan that this kind of international WPI workshop including all the disciplines of WPI is held around the first week of March, every year. Of course, more specialized symposia of compact size may be organized when they are needed. Finally I believe you will obtain rich fruits by participating in these future workshops.

Research Prospect



Prof. Akihisa INOUE
東北大学総長・主任研究者 井上 明久



Prof. Dmitri V. Louzguine
教授 ルズギン・ドミトリ

SOLIDIFICATION, GLASS-FORMATION, STRUCTURAL FEATURES AND CRYSTALLIZATION BEHAVIOR OF Cu-BASED GLASSY ALLOYS

Dmitri V. Louzguine-Luzgin and Akihisa Inoue

*WPI Advanced Institute for Materials Research, Tohoku University,
Katahira 2-1-1, Aoba-Ku, Sendai 980-8577, Japan*

Cu-based glassy alloys exhibit high strength, good glass-forming ability (GFA) and significantly high stability of the supercooled liquid. In the present work we describe solidification, structural features and crystallization behavior of recently discovered Cu-based bulk glassy alloys. The resistance of the supercooled liquid to crystallization in these alloys has opened opportunities to study the glass transition and crystallization kinetics in the supercooled liquid region. The addition of a certain fraction of Ag to Cu-based alloy causes an increase in the reduced glass-transition temperature and γ parameter values in expense of lowering liquidus and increasing their crystallization temperature. The structure of the Cu-based alloys is studied by real-space distribution functions. It is suggested that the medium-range order maintains up to about 2 nm distance. It is also found that the structure of the Cu-Ag-Zr-Ti glassy alloy depends on cooling rate. It is glassy in the case of ribbon samples while the nanoscale highly ordered clusters are formed in the bulk samples. Nevertheless the studied Cu-based alloys crystallize by nucleation and 3-dimensional crystal growth process. The cooling curve of the ingot cast in Cu-mould can be fit successfully with an exponential decay equation with two exponents. This rather indicates that both processes: the heat transfer through the melt as well as through the melt/mould interface influence the cooling rate observed. For a small ingot of 3 mm in diameter the average cooling rate in the region between the liquidus and glass-transition temperature is about 10^3 K/s. Such a high value demonstrates that equilibrium phase diagrams can be used for predicting the GFA only in a rough approximation.

Introduction

Since the synthesis of a metallic amorphous phase in the Au-Si system by a rapid solidification technique [1], a great number of metallic amorphous and glassy alloys have been produced in different alloy systems. Later the high glass-forming ability achieved at some alloy compositions allowed to produce bulk metallic glasses [2] in the thickness range of 1-100 mm by using various casting processes based on the principles for achieving high glass-forming ability [2]. Bulk glassy alloys exhibit high strength, hardness, wear resistance and large elastic deformation and high corrosion resistance. Glassy alloys being metastable undergo relaxation and devitrification (crystallization) processes on heating. The thermal expansion, glass-transition and volume change on heating were studied in several glassy alloys by synchrotron beam X-ray diffractometry. Recently these features were also studied for Cu-Hf-Ti-Pd glassy alloy using a real-space distribution function [3].

Cu-Zr-Ti bulk glassy alloys were reported to exhibit a high mechanical strength exceeding 2 GPa. A quaternary $\text{Cu}_{55}\text{Zr}_{30}\text{Ti}_{10}\text{Co}_5$ glassy alloy showed the highest among Cu-based glasses ultimate compressive strength value of 2.3 GPa [4]. The formation of the nanoscale icosahedral phase was recently observed in the Cu-Zr-Ti alloys containing Pd [5] and Au while Ag- and Pt-bearing alloys did not form the icosahedral phase.

1. Influence of cooling rate on the structure and properties of a Cu-Zr-Ti-Ag glassy alloy

Solidification behavior of $\text{Cu}_{44}\text{Ag}_{15}\text{Zr}_{36}\text{Ti}_5$ glassy alloy (the composition is given in nominal atomic percentages) was studied using a Cu-mould casting technique [6]. The time-temperature cooling curves upon casting into Cu mould were recorded by using a thin K-type thermocouple (as schematically is shown in Fig. 1.1) which was connected to an analog-to-digital converter.

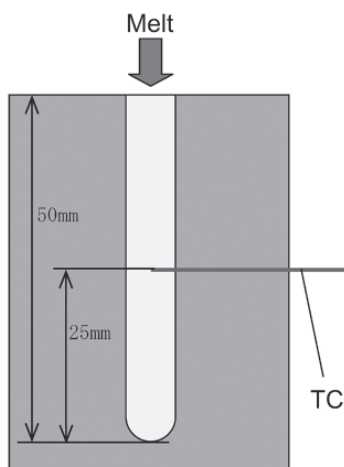


Fig. 1.1. Schematic illustration of Cu mould and location of the thermocouple (TC).

As was shown by XRD experiments the structure of the as-solidified alloy in ribbon and bulk shapes was found to consist of a glassy phase. Fig. 1.2 represents the time-temperature cooling traces for the $\text{Cu}_{44}\text{Ag}_{15}\text{Zr}_{36}\text{Ti}_5$ glassy alloy samples of 3 and 5 mm in diameter and the resulted cooling rate measured at $T_g \sim 700$ K as a tangent to the graph is about 600 K/s and 200 K/s, respectively. Upon casting the melt temperature decreases nonlinearly. The initial cooling rate of the liquid in the center of the 3 mm ingot of the sample during initial 100 ms is about 2000 K/s. The same value for the 5 mm sample is 600 K/s. The cooling rate upon melt spinning was estimated at 10^5 - 10^6 K/s.

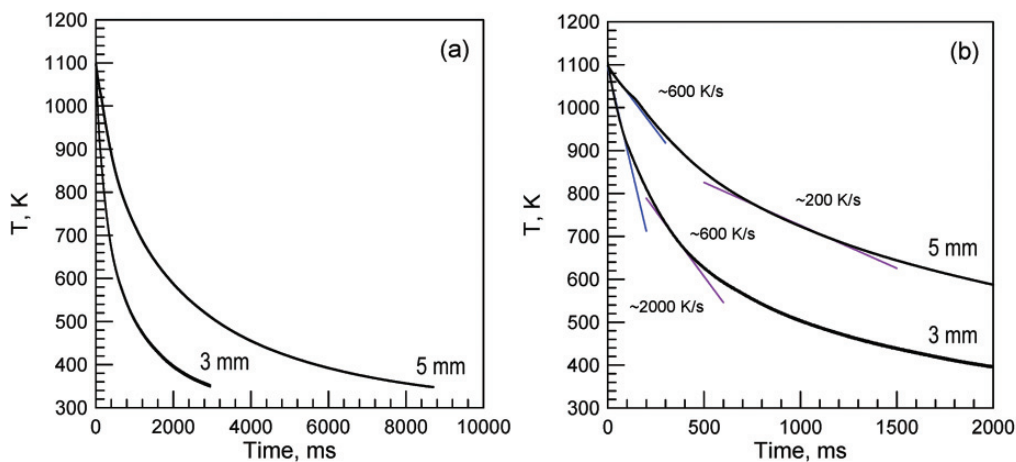


Fig. 1.2. Time-temperature cooling traces for the $\text{Cu}_{44}\text{Ag}_{15}\text{Zr}_{36}\text{Ti}_5$ glassy alloy samples of 3 and 5 mm in diameter. (a and b) represent different time scale for convenience.

The devitrification behavior of the alloy samples on heating was investigated using DSC. The studied alloy undergoes a two-stage crystallization by 3-dimensional diffusion-controlled growth process which is typical for primary crystallization mechanism.

The DSC traces of the as-solidified samples demonstrate an increment of the heat capacity (C_p) at the glass transition temperature (T_g) and subsequent exothermic peak owing to crystallization of the supercooled liquid (see Fig. 1.3). Heat of structure relaxation of the ribbon, 3 mm and 5 mm samples prior to glass-transition is 1.83 (100 %), 0.87 (48 %) and 0.64 (35 %) J/mol, respectively.

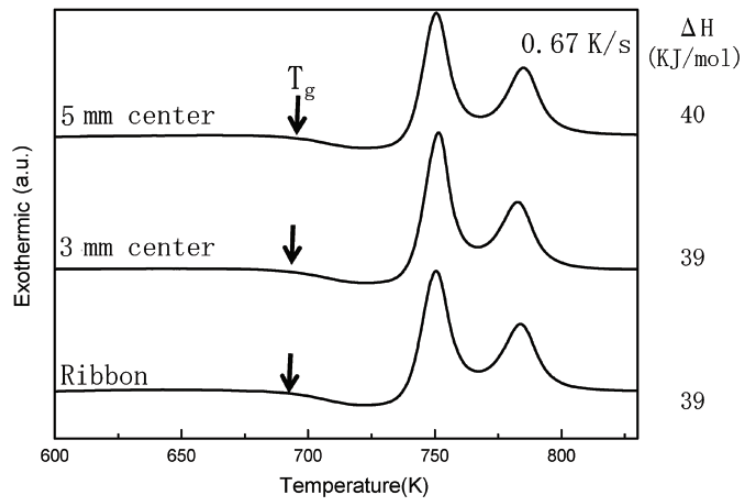


Fig. 1.3. The DSC traces of the as-solidified ribbon and bulk samples as well as the exothermic heat release corresponding to both exothermic events.

The isothermal calorimetry trace allowed to produce the Avrami plot. The Avrami plot created according to the following kinetic law for the volume fraction (x) transformed as a function of time (t): $x(t) = 1 - \exp(-Kt^n)$ was found to be reasonably linear and $n=2.3$ rather indicates 3-dimensional diffusion-controlled growth process.

During the exothermic reactions (see peaks in Fig. 1.3) the supercooled liquid crystallizes forming oC68 $\text{Cu}_{10}\text{Zr}_7$ and tP4 AgZr phases, though some weak peaks remain unidentified which indicates possible existence of a third phase.

Vickers microhardness data indicate that the HV values of the bulk samples are found to be close to each other but significantly different from that of the ribbon sample using a confidence interval with the probability of 95 % (Fig. 1.4).

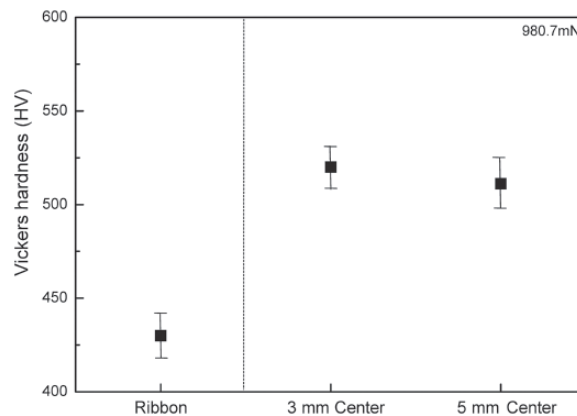


Fig. 1.4. Vickers microhardness as a function of the sample size, and thus, cooling rate.

As the Vickers microhardness of the ribbon and bulk samples is different we performed a deep structural investigation of the as-solidified samples. As shown in Fig. 1.5 (a and c) the ribbon sample has a uniform structure while the bulk sample exhibits some highly ordered regions Fig. 1.5 (b and d) of about 3 nm size within the glassy phase. The nanobeam diffraction (NBD) pattern taken from this region can be indexed according to the AgZr phase.

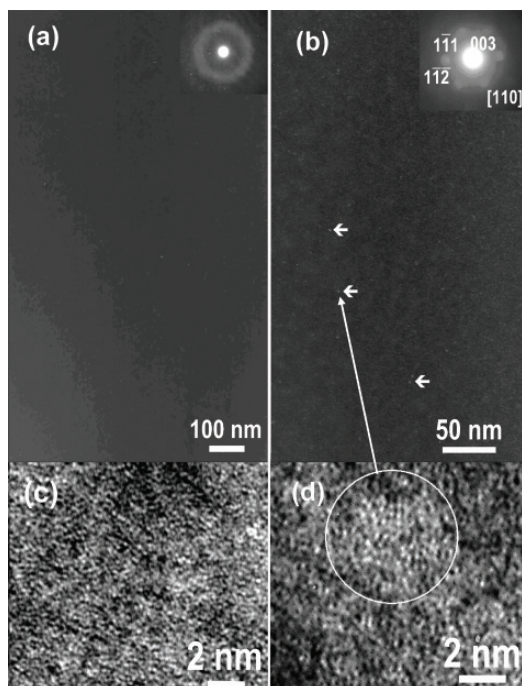


Fig. 1.5. The structure of (a) the ribbon sample and (b) bulk sample of 5 mm in diameter, TEM dark-field. The inserts are typical NBD patterns, respectively. Visible camera length is somewhat different in each case due to subsequent image processing. Some of the NBD patterns taken from these regions can be indexed according to AgZr phase. (c) and (d) are the corresponding high-resolution TEM images. The ribbon sample (c) has a uniform glassy structure while the bulk sample exhibits some highly ordered regions (d) of about 3 nm in size within the glassy phase marked with arrows in (b). The structure of the ion-polished and electrochemically polished samples did not differ by sight.

It is found that the structure of the $\text{Cu}_{44}\text{Ag}_{15}\text{Zr}_{36}\text{Ti}_5$ glassy alloy depends on cooling rate. It is glassy in the case of ribbon samples while the nanoscale clusters of the crystalline phase (highly ordered regions) are formed in the bulk samples. Such a change is reflected in the shift of the X-ray diffraction peak, in the magnitude of the heat of structure relaxation and in the variation of the Vickers microhardness observed in Fig. 1.4. A slight deviation of the cooling curve signal of the 5 mm bulk sample at 1030 K observed in Fig. 1.2 likely corresponds to the formation of the ordered regions.

We also studied the cooling rate as a function of casting temperature. The cooling curves in Fig. 1.6 are plotted from a certain arbitrary temperature above the liquidus temperature for better comparison. Fig. 1.7 shows that the cooling rate at T_g slightly changes with casting temperature.

However, the DSC, HV and XRD data of the samples cast from different temperatures did not show any systematic variation as the cooling rate (Fig. 1.7) varied only by about 20 %.

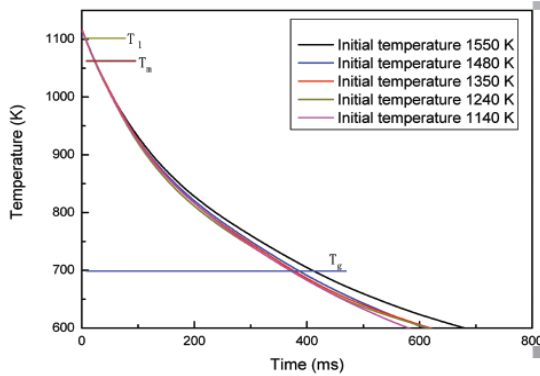


Fig. 1.6. Cooling curves of the bulk sample (3 mm) recorded from different casting temperature.

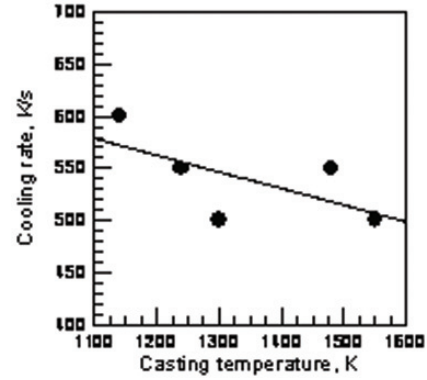


Fig. 1.7. Cooling rate R at T_g as a function of casting temperature.

The cooling rate at T_g depends upon the ingot size. At the same time the cooling rate also slightly depends upon the casting temperature (Fig. 1.6 and 1.7). It takes place likely owing to different amounts of heat which was transferred to the mould (depending upon casting temperature which determines the heat content of the melt) and caused its heating.

Heat transfer through the melt, heat transfer through the melt-mould interface and heat transfer through the mould take place upon cooling of the melt. The interfacial heat transfer coefficient (h) indicates a heat transfer rate through the melt/mould interface. The Biot number (Bi) defined as hL/λ_l , (where L is a characteristic length scale and λ_l is the thermal conductivity of the liquid being cast) indicates which process: heat transfer through the melt or heat transfer through the melt/mould interface dominates upon cooling. The value of the Biot number calculated for Cu-based alloys is about 1 which implies that the temperature gradients inside the melt are non-negligible.

As one can see in Fig. 1.8 the cooling curve of the 3 mm ingot cannot be fit well with Newtonian equation (violet line). However, it can be fit very well (Fig. 1.8) if an exponential decay equation with two exponents is used: $T(t) = T_0 + A_1 e^{-t/\tau_1} + A_2 e^{-t/\tau_2}$ where $T_0 = 314$ K, $A_1 = 347$ K, $\tau_1 = 0.205$ s, $A_2 = 429$ K, $\tau_2 = 1.209$ s. This may indicate that both processes: the heat transfer through the melt as well as through the melt/mould interface influence the cooling rate obtained. The results suggest that upon bulk glass casting the thermal conduction within the melt also plays an important role influencing the cooling rate.

The cooling rate drastically changes with temperature as shown in Fig. 1.8 (b) but the important values belong to the region between T_1 and T_g . The average value in this region is close to 1200 K/s. Such a high average value of 1200 K/s clearly demonstrates that casting conditions of

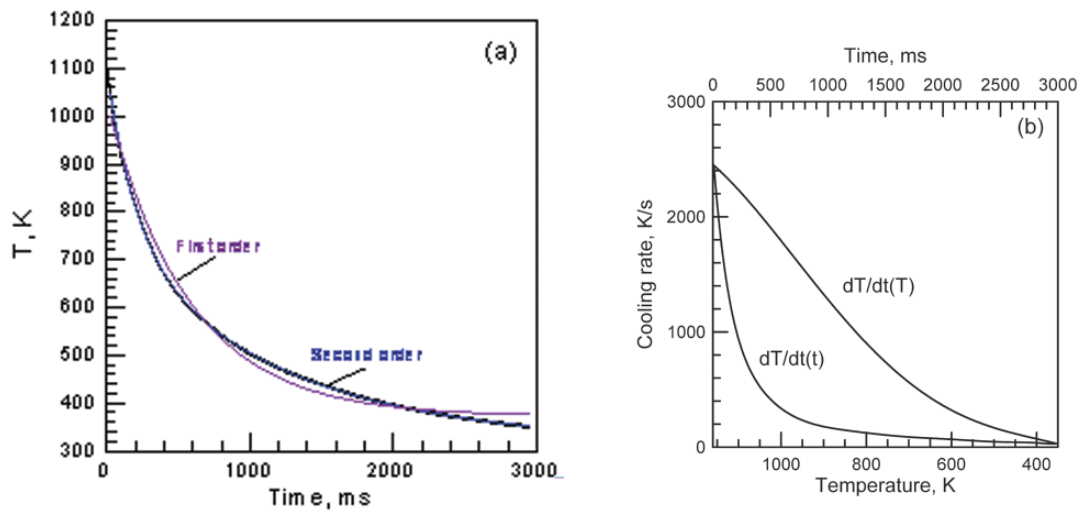


Fig. 1.8. (a) Cooling curve of the studied alloy (black curve behind blue one) taken from the central part of the ingot of 3 mm in diameter. Violet line – the best fit with the Newtonian cooling law. Blue line – fit with second order exponential decay function. (b) The cooling rate as a function of time and temperature.

conventional bulk glassy alloys are far from equilibrium and equilibrium phase diagrams can be used for predicting the GFA only in a rough approximation.

Contrary to ribbon samples cast at about 10^6 K/s bulk glassy samples cast at a cooling rate about three-four orders in magnitude lower contain highly ordered clusters up to 3-5 nm in size. Such a difference in the structure causes the observed variation in microhardness as nanoscale ordered regions were found to cause strengthening of the glassy matrix owing to different atomic structure of these regions or change in the matrix composition.

2. Real-space structural studies of Cu-Zr-Ti glassy alloy

The interference function $Q_i(Q)$ for $\text{Cu}_{60}\text{Zr}_{30}\text{Ti}_{10}$ alloy calculated from the XRD intensity profile after the necessary corrections is shown in Fig. 2.1 while RDF(r) obtained by Fourier Transformation is shown in Fig. 2.

Taking into account large negative mixing enthalpy of the Cu-Zr interatomic pair one can assume that this pair is the most probable interatomic distance corresponding to left shoulder of the PDF function in the present alloy. As the maximum of the left shoulder (0.273 nm) corresponds to lower value than the predicted Cu-Zr interatomic distance (0.289 nm) one can assume that this distance in the studied glassy alloy is lower than that predicted by the Goldschmidt atomic radii due to negative mixing enthalpy (attractive interaction) in this atomic pair.

Such effect is quite common in the intermetallic compounds. For example, oC68 $\text{Cu}_{10}\text{Zr}_7$ phase is a stable phase forming in the $\text{Cu}_{60}\text{Zr}_{30}\text{Ti}_{10}$ alloy after crystallization of the glassy phase. It

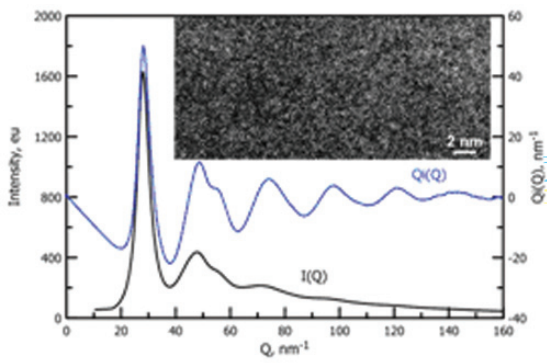


Fig. 2.1. Scattered intensity $i(Q)$ and $Q_i(Q)$ functions of $\text{Cu}_{60}\text{Zr}_{30}\text{Ti}_{10}$ alloy. The insert – high resolution TEM image (HRTEM) of as-solidified sample.

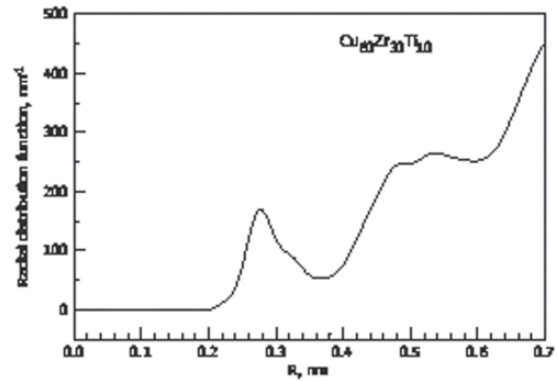


Fig. 2.2. Radial distribution function of $\text{Cu}_{60}\text{Zr}_{30}\text{Ti}_{10}$ alloy.

is isomorphous to oC68 $\text{Ni}_{10}\text{Zr}_7$ one, has close lattice parameters and the Goldschmidt atomic radius of Ni is close to that of Cu. In some clusters this phase shows Ni-Zr distances as small as 0.238 nm and typical Ni-Zr interatomic distances are about 0.26-0.28 nm which is less than 0.289 nm predicted by the Goldschmidt atomic radii but corresponds well to the PDF(r) peak position.

These data are in good correspondence with the results of the PDF(r) function fitting with two Gaussian peaks as shown in Fig. 2.3. The second peak corresponds well to Zr-Zr interatomic distance while first one can be a combination of the peaks produced by other atomic pairs. Different Cu-Cu and Cu-Zr interatomic distances observed in the oC68 $\text{Cu}_{10}\text{Zr}_7$ compound varying in wide ranges from about 0.24 to 0.31 nm for Cu-Zr pair and from about 0.22 to 0.31 for Cu-Cu pair explain the single-peak shape of the main PDF(r) maximum (Fig. 3) responsible for the Cu-Cu, Cu-Ti and Cu-Zr atomic pairs.

According to Fig. 2.4 a detectable medium-range order maintains until about 2 nm (Fig. 2.4 (a)) of the interatomic distance independently on the truncation distance of the Fourier Transformation in the reciprocal space (Fig. 2.4 (b)). Such a high degree of medium range order is well consistent with recent models which predict that metallic glasses are not random packing of

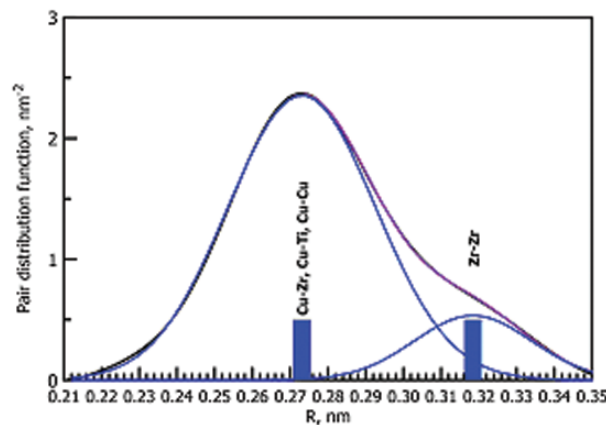


Fig. 2.3. Fitting of the first maximum of PDF(r) (baseline corrected) with 2 Gaussian peaks.

atoms but dense packing of clusters. It is also deduced from the small density difference between glassy and the corresponding crystalline phases.

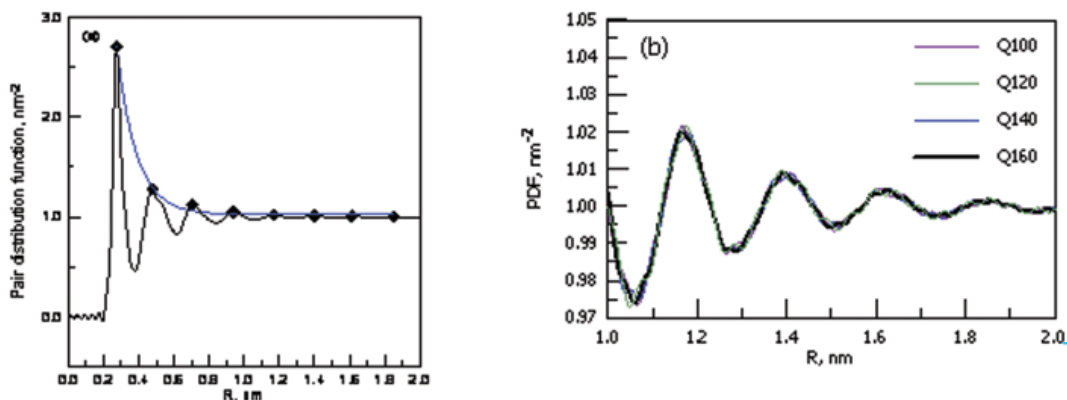


Fig. 2.4. (a) Fitting of the PDF(r) maxima with the exponential decay function. (b) medium-range distance PDF(r) function. Q100-160 PDF(r) traces represent truncation of the Fourier Transformation procedure of $Q_i(Q)$ at different Q values ranged from 100 to 160 nm^{-1} . It is seen that the notwithstanding on some noise (inherited from the XRD patterns) the positions of the PDF(r) maxima change insignificantly.

A question may arise if the medium-range order maintains until about 2 nm why no clearly ordered zones are seen in the HRTEM image in Fig. 1. If one takes a Fast Fourier Transformation (FFT) of two parts of the HRTEM image like shown in Fig. 2.5 one can see that although the FFT image shows a diffuse halo only from the area of about 4 nm^2 it has some features if taken from the area of about 2 nm^2 . At the same time an icosahedral-type medium range order which is expected to be a dominant local configuration in liquids and metallic glasses may be a good explanation why no crystal-like atomic arrays are observed in the HRTEM images (Figs. 1 and 5) of these glasses.

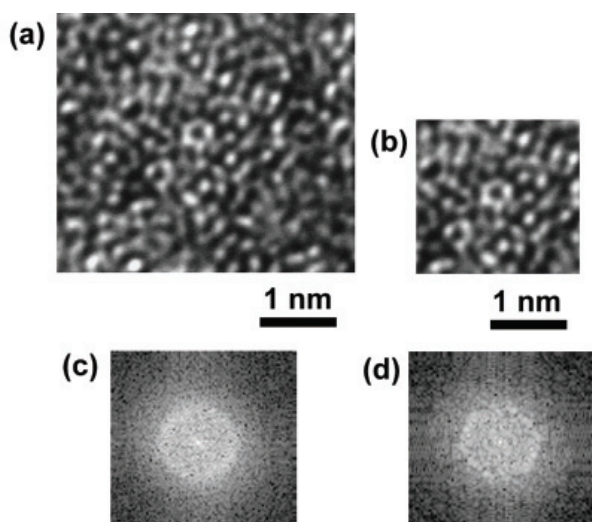


Fig. 2.5. Two parts of the HRTEM image in Fig. 1: (a) about 4 nm^2 and (b) about 2 nm^2 in size. Area (b) is a part of (a). (c) and (d) the corresponding FFT images.

3. Devitrification behavior and glass-forming ability of Cu-Zr-Ag alloys

Bulk glass formation in the Cu-Zr-Ag glassy alloys has been studied recently. $\text{Cu}_{45}\text{Zr}_{45}\text{Ag}_{10}$ alloy exhibited the highest glass-forming ability (GFA) (the critical diameter is 6 mm) among Cu-Zr-Ag glassy alloys and high mechanical strength of 1.8 GPa [7].

The structure of the as-solidified Cu-Zr-Ag alloys was found to consist of a glassy phase. The devitrification behavior on heating was investigated using DSC. The DSC traces of the as-solidified $\text{Cu}_{55-x}\text{Zr}_{45}\text{Ag}_x$ samples shown in Fig. 3.1 demonstrate an increment of heat capacity (C_p) at the glass transition temperature (T_g) (the temperature corresponding to the beginning of glass-transition is shown in the figure) and subsequent exothermic peak due to crystallization of the supercooled liquid starting at the onset temperature (T_x) (see Fig. 3.1). The T_g and T_x temperatures plotted in Fig. 3.2 (a) as a function of Ag content were determined from the intersection of two tangents to the curve below and above the onset temperature. The supercooled liquid region (ΔT_x) also shown in Fig. 3.2 (a) is defined as the difference between T_x and T_g . On heating above T_g a glassy phase becomes a supercooled liquid which is still not crystallized below T_x .

The phase composition of the annealed samples determined using the XRD patterns is

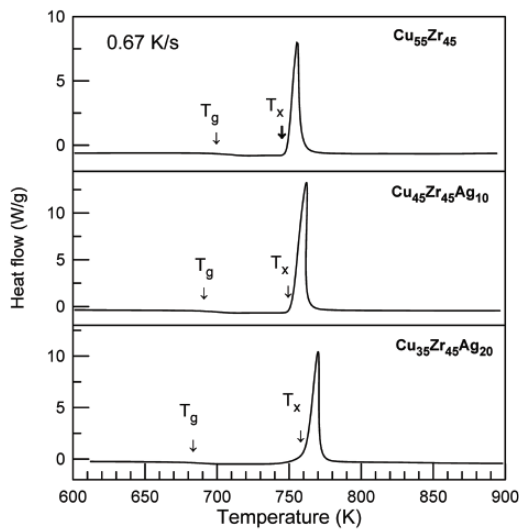


Fig. 3.1. DSC traces of the $\text{Cu}_{55-x}\text{Zr}_{45}\text{Ag}_x$ glassy alloys.

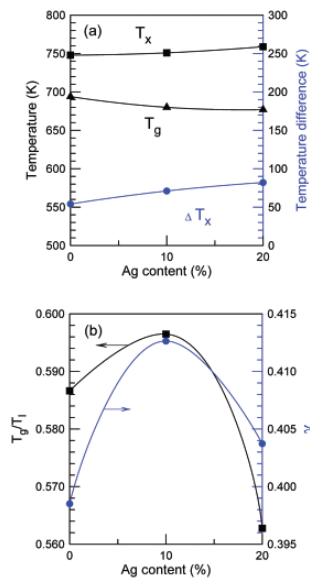


Fig. 3.2. (a) T_g , T_x and ΔT_x as well as (b) T_g/T_i and γ parameter values as a function of Ag content.

shown in Fig. 3.3. During the exothermic reactions (see peaks in Fig. 3.1) the supercooled liquid crystallizes forming oC68 $\text{Cu}_{10}\text{Zr}_7$ phase in $\text{Cu}_{55}\text{Zr}_{45}$ alloy and a mixture of oC68 $(\text{Cu,Ag})_{10}\text{Zr}_7$ and tP4 $(\text{Ag,Cu})\text{Zr}$ solid solution phases in Ag-bearing alloys.

Upon the isothermal calorimetry in both Ag-bearing alloys the crystallization started after a

certain incubation period (about 350 s for $\text{Cu}_{45}\text{Zr}_{45}\text{Ag}_{10}$ and $\text{Cu}_{35}\text{Zr}_{45}\text{Ag}_{20}$ alloys at 717 and 722 K, respectively) which indicates nucleation and growth transformation mechanism.

The linearity of the Avrami plot of $\ln(-\ln(1-x))$ vs. $\ln(t)$ for both Ag-bearing alloys shown

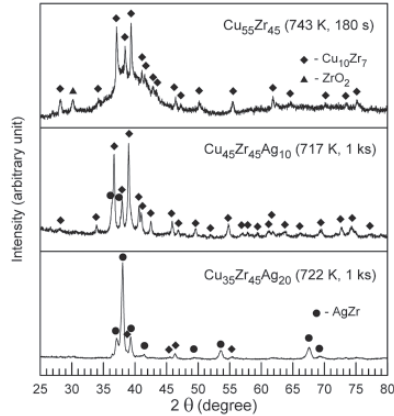


Fig. 3.3. X-ray diffraction patterns of the $\text{Cu}_{55-x}\text{Zr}_{45}\text{Ag}_x$ glassy alloys in a heat treated state.

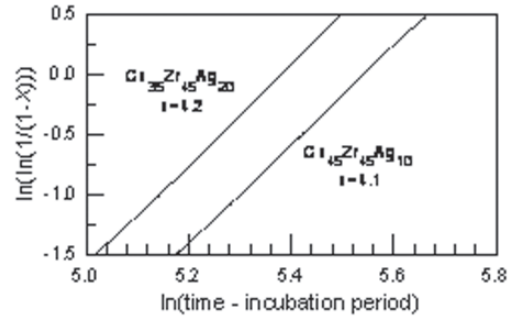


Fig. 3.4. The Avrami plots for $\text{Cu}_{45}\text{Zr}_{45}\text{Ag}_{10}$ and $\text{Cu}_{35}\text{Zr}_{45}\text{Ag}_{20}$ glassy alloys constructed using the isothermal calorimetry data.

in Fig. 3.4 indicates that the crystallization of the alloys obeys the well-known kinetic law for the volume fraction (x) transformed as a function of time (t): $x(t) = 1 - \exp(-Kt^n)$ provided that the nucleation and growth rates are time-independent which causes the linearity of the Avrami plot. The values of the Avrami exponent obtained are close to 4 which indicates a steady-state nucleation and 3-dimensional interface-controlled growth of nuclei.

XRD results (see Fig. 3.3) indicate that $(\text{Cu,Ag})_{10}\text{Zr}_7$ phase is the main structure constituent in the $\text{Cu}_{45}\text{Zr}_{45}\text{Ag}_{10}$ alloy while the $\text{Cu}_{35}\text{Zr}_{45}\text{Ag}_{20}$ alloy contains a large fraction of $(\text{Ag,Cu})\text{Zr}$ phase. The phase composition was confirmed using TEM (Figs. 3.5 and 3.6) including selected-area electron diffraction (SAED) patterns.

A small volume fraction (~ 10 vol.%) of a residual globular glassy phase is observed in the structure of the $\text{Cu}_{35}\text{Zr}_{45}\text{Ag}_{20}$ alloy (Fig. 3.6 (a)) while no phase separation was found in the case of the as-solidified sample and the sample annealed at T_g . According to EDX analysis (Table 3.1) the residual amorphous phase is depleted in Ag compared to the crystalline region. It contains only about 14 at.% Ag.

A limited difference in the crystallization behavior of $\text{Cu}_{55-x}\text{Zr}_{45}\text{Ag}_x$ alloys (at least at $x \leq 10$)

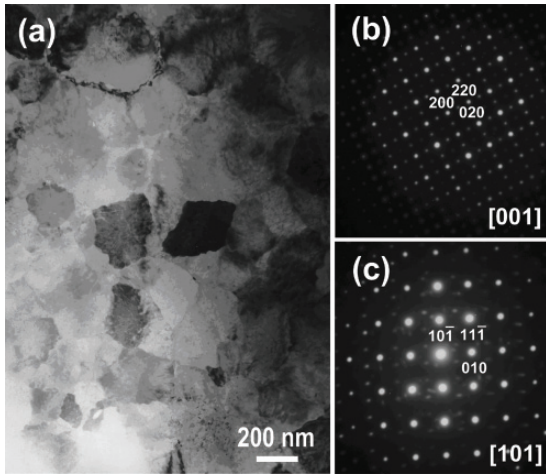


Fig. 3.5. The structure of the $\text{Cu}_{45}\text{Zr}_{45}\text{Ag}_{10}$ alloy annealed at 730 K for 300 s, TEM. (a) – Bright-field image. Grains of both $(\text{Cu,Ag})_{10}\text{Zr}_7$ and $(\text{Ag,Cu})\text{Zr}$ phases are observed. (b) and (c) SAED patterns taken from $(\text{Cu,Ag})_{10}\text{Zr}_7$ and $(\text{Ag,Cu})\text{Zr}$ phases, respectively.

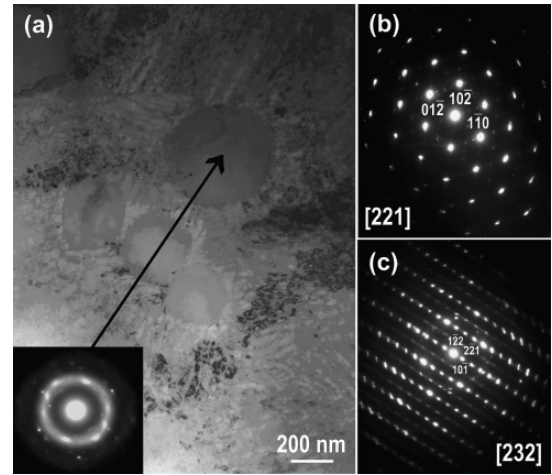


Fig. 3.6. The structure of $\text{Cu}_{35}\text{Zr}_{45}\text{Ag}_{20}$ alloy annealed at 722 K for 1 ks, TEM. (a) – Bright-field image. The insert-SAED pattern from the globular amorphous phase. (b) and (c) SAED patterns taken from $(\text{Ag,Cu})\text{Zr}$ and $(\text{Cu,Ag})_{10}\text{Zr}_7$ phases, respectively.

Table 3.1. Chemical composition of the thermodynamic phases observed in $\text{Cu}_{35}\text{Zr}_{45}\text{Ag}_{20}$ alloy annealed at 722 K for 1 ks.

Phases\Elements	Cu, at. %	Zr, at. %	Ag, at. %
oC68 $(\text{Cu,Ag})_{10}\text{Zr}_7$	34	43	23
tP4 $(\text{Ag,Cu})\text{Zr}$	20	54	26
Residual amorphous	34	52	14

was found. Ag-bearing and Ag-free alloys exhibit devitrification forming of a supercooled liquid region and subsequent crystallization forming equilibrium crystalline phases. The simultaneous formation of oC68 $(\text{Cu,Ag})_{10}\text{Zr}_7$ and tP4 $(\text{Ag,Cu})\text{Zr}$ solid solution phases in the Ag-bearing alloys by nucleation and 3-dimensional interface-controlled growth of nuclei indicates rather eutectic crystallization. These phases exist in both studied Ag-bearing alloys at room temperature in accordance with the equilibrium Ag-Cu-Zr phase diagram.

T_g/T_1 ratio for the $\text{Cu}_{45}\text{Zr}_{45}\text{Ag}_{10}$ alloy of 0.596 (Fig. 3.2 (b)) is larger than that 0.587 calculated for the binary $\text{Cu}_{55}\text{Zr}_{45}$ alloy calculated taking into account its liquidus temperature of about 1183 K and 0.563 obtained for $\text{Cu}_{35}\text{Zr}_{45}\text{Ag}_{20}$ alloy having T_1 of 1203 K. γ parameter ($T_x/(T_g+T_1)$) values are 0.399 for $\text{Cu}_{55}\text{Zr}_{45}$, 0.413 for $\text{Cu}_{45}\text{Zr}_{45}\text{Ag}_{10}$ and 0.404 for $\text{Cu}_{35}\text{Zr}_{45}\text{Ag}_{20}$ alloy (Fig. 3.2 (b)). As one can see the addition of 10 at.% Ag causes a significant increase in T_g/T_1 and γ parameter values in expense of lowering T_1 and increasing T_x . $\text{Cu}_{45}\text{Zr}_{45}\text{Ag}_{10}$ alloy exhibits the highest GFA (critical diameter of about 6 mm) while $\text{Cu}_{35}\text{Zr}_{45}\text{Ag}_{20}$ alloy shows much lower GFA in accordance with lower T_g/T_1 and γ parameter values.

$\text{Cu}_{35}\text{Zr}_{45}\text{Ag}_{20}$ alloy exhibits possible phase separation upon heating within a supercooled liquid region just prior to crystallization of a liquid because no phase separation is observed at T_g and below it. This may be the reason for the existence of the residual globular amorphous phase observed in the sample heat treated at 722 K for 1 ks (Fig. 3.6 (a)). This residual amorphous phase requires higher temperature for crystallization. Such a phase separation in the Cu-Zr-Ag system can be expected according to a simple eutectic-type Cu-Ag phase diagram and a slightly negative mixing enthalpy in Cu-Ag pair.

4. Influence of Al and Ag on the Devitrification Behavior of a Cu-Zr Glassy Alloy

Cu-Zr-Al-Ag alloys also showed high GFA [8]. The DSC traces of the as-solidified $\text{Cu}_{50}\text{Zr}_{50}$, $\text{Cu}_{50}\text{Zr}_{45}\text{Al}_5$ and $\text{Cu}_{45}\text{Zr}_{45}\text{Al}_5\text{Ag}_5$ samples are shown in Fig. 4.1.

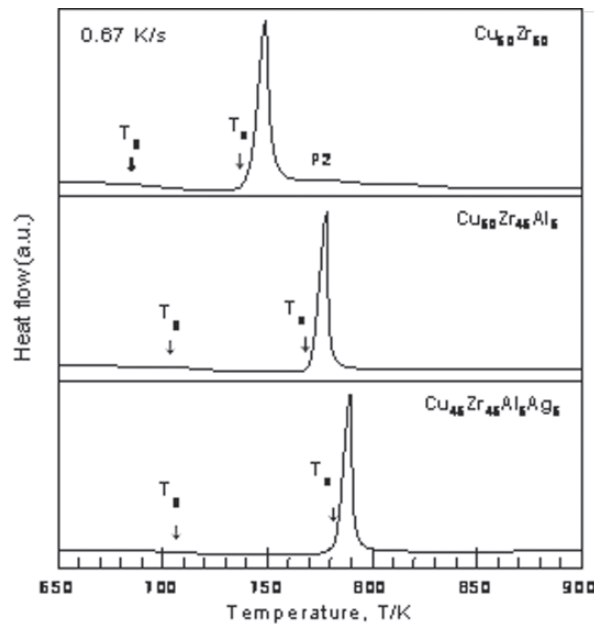


Fig. 4.1. DSC traces of the studied alloys. The DSC trace of the $\text{Cu}_{50}\text{Zr}_{50}$ alloy is also shown for comparison; P2 illustrates the position of the broad second peak.

The phase composition of the annealed samples is determined using the XRD patterns shown in Fig. 4.2. During the exothermic reactions (see peaks in Fig. 4.2) the supercooled liquid crystallizes forming oC68 $\text{Cu}_{10}\text{Zr}_7$ phase and an unidentified phase in $\text{Cu}_{50}\text{Zr}_{45}\text{Al}_5$ alloy while $\text{Cu}_{45}\text{Zr}_{45}\text{Al}_5\text{Ag}_5$ alloy forms a mixture of oC68 $\text{Cu}_{10}\text{Zr}_7$, cF16 Cu_2AlZr and tP4 AgZr phases. XRD results (see Fig. 4.2) indicate that although the $\text{Cu}_{10}\text{Zr}_7$ phase is the main structure constituent in the studied alloys other crystalline phases also precipitate simultaneously indicating rather eutectic crystallization.

The isothermal calorimetry data showed that in both alloys the crystallization started after a

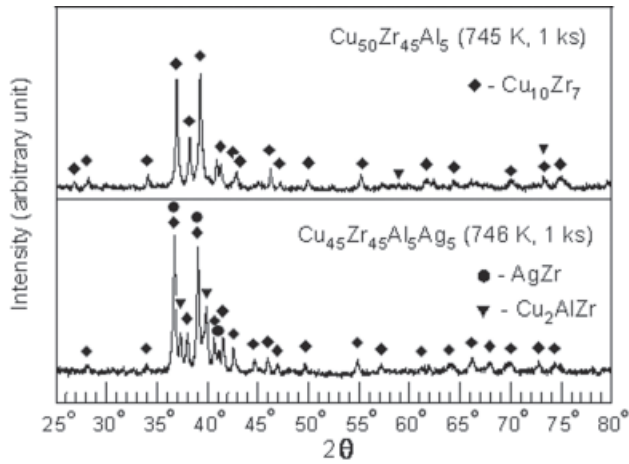


Fig. 4.2. XRD patterns of the studied alloys in a heat-treated state.

certain incubation period (about 180 and 230 s for $\text{Cu}_{50}\text{Zr}_{45}\text{Al}_5$ and $\text{Cu}_{45}\text{Zr}_{45}\text{Al}_5\text{Ag}_5$ alloys at 745 and 746 K, respectively) which indicates nucleation and growth transformation mechanism.

All of the Avrami plots of $\ln(-\ln(1-x))$ vs. $\ln(t)$ demonstrated a non-linear character which indicates that the nucleation and growth rates are rather time-dependent. Nevertheless, an average Avrami exponent for $\text{Cu}_{45}\text{Zr}_{45}\text{Al}_5\text{Ag}_5$ alloy is close to 4 which may indicate the nucleation and 3-dimensional interface-controlled growth process.

The binary $\text{Cu}_{50}\text{Zr}_{50}$ alloy exhibits inharmonic shape of the DIC traces, and thus, the shape of the Avrami plot is not linear indicating deceleration of the phase transformation with time (4.3). The XRD analysis indicates that the crystallizing phase is rather a metastable monoclinic CuZr phase. This is in consistent with the Cu-Zr phase diagram which indicatives that cubic cP2 CuZr phase is unstable below 988 K. The mP CuZr phase decomposes at higher temperature while $\text{Cu}_{10}\text{Zr}_7$ and CuZr_2 phases are formed.

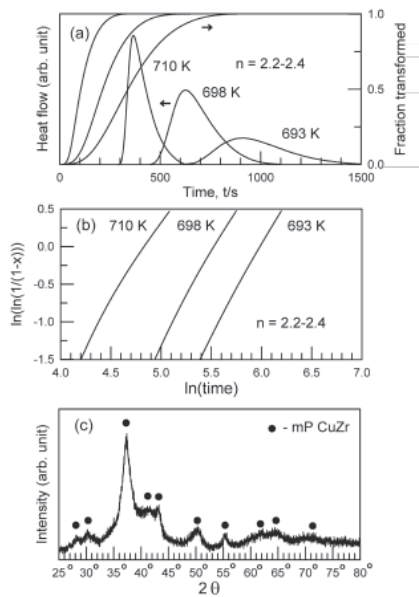


Fig. 4.3. (a) Isothermal calorimetry traces and fraction transformed as a function of time (without incubation period) of the $\text{Cu}_{50}\text{Zr}_{50}$ glassy alloy and (b) the resulted Avrami plot. (c) XRD trace of the sample annealed for 1.2 ks at 698 K.

The crystallization behavior of the studied alloys nearly follows the equilibrium phase diagrams, that is, $\text{Cu}_{50}\text{Zr}_{45}\text{Al}_5$ and $\text{Cu}_{45}\text{Zr}_{45}\text{Al}_5\text{Ag}_5$ glassy alloys exhibit rather eutectic crystallization while the $\text{Cu}_{50}\text{Zr}_{50}$ forms a nanoscale primary metastable CuZr phase with a monoclinic structure. The formation of such a phase may be initiated by the relatively low crystallization temperature compared to the temperature of eutectoid transformation in CuZr alloy of 988 K.

The eutectic compositions are suitable for BMG alloys as these alloys exhibit low liquidus temperature, and thus, high stability of a liquid versus crystallization compared to $\text{Cu}_{50}\text{Zr}_{50}$ alloy. For example, $\text{Cu}_{50}\text{Zr}_{50}$ glassy alloy has a T_g/T_l ratio and γ parameter of 0.555 and 0.387, respectively while $\text{Cu}_{45}\text{Zr}_{45}\text{Al}_5\text{Ag}_5$ glassy alloy 0.617 and 0.429, respectively. $\text{Cu}_{45}\text{Zr}_{45}\text{Al}_5\text{Ag}_5$ alloy also shows a large supercooled liquid region of 86 K which suggests that it can be deformed by viscous flow in this region.

Another important reason is effective filling of space by atoms of different sizes. Such a feature may also be favored at eutectic compositions at which liquid shows high stability. Nevertheless, as cooling conditions upon bulk glass casting are far from equilibrium one must consider the effect of the metastable phase diagram and the shift of eutectic point. The fact that the crystalline $\text{Cu}_{45}\text{Zr}_{45}\text{Al}_5\text{Ag}_5$ alloy does not show a single stage eutectic reaction on melting agrees well with the proposition that the best glass-formers belong to slightly off- equilibrium eutectic compositions and correspond to non-equilibrium eutectics. Solute partitioning upon eutectic crystallization may also be the reason restricting the crystallization rate of Al- and Ag- bearing alloys compared with Cu-Zr one.

EXPERIMENTAL DETAILS

The ingots were prepared by arc-melting mixtures of pure metals in an argon atmosphere. From these ingots, ribbon samples of about 20 μm as well as bulk glassy samples having a diameter of 3 or 5 mm were prepared by rapid solidification of the melt on a single copper roller at a roller tangential velocity of about 40 m/s and a Cu-mould casting technique, respectively. The structure of the samples was examined by X-ray diffractometry (XRD) with monochromatic CuK_α radiation. Phase transformations were studied by differential scanning calorimetry (DSC) at a heating rate of 0.67 K/s and differential isothermal calorimetry. Transmission electron microscopy (TEM) investigation was carried out using a JEM 2010 (JEOL) microscope operating at 200 kV equipped with an energy dispersive X-ray spectrometer (EDX) of 0.1 keV resolution.

Synchrotron radiation X-ray diffraction in transmission was carried out using a high energy monochromatic beam of the European Synchrotron Radiation Facility (ESRF) equipped with a nitrogen-cooled double-silicon monochromator. After correction the measured intensity was converted to electron units per atom. The total structure factor $S(Q)$ and the interference function $Q_i(Q)$ have been obtained from the coherent scattering intensity. The radial distribution $\text{RDF}(r)$ and pair distribution $\text{PDF}(r)$ functions have been obtained by the Fourier transformation of $Q_i(Q)$.

References

- [1] W. Klement, R. H. Willens, and P. Duwez, *Nature* 187 (1960) 869.
- [2] A. Inoue, *Acta Mater.* 48 (2000) 279.
- [3] D. V. Louzguine-Luzgin, A. Inoue, A. R. Yavari, and G. Vaughan, *Appl. Phys. Lett.* 88 (2006) 121926.
- [4] D. V. Louzguine and A. Inoue, *Phil. Mag. Lett.* 83 (2003) 191.
- [5] D. V. Louzguine, A. R. Yavari and A. Inoue, *Philosophical Magazine* 83 (2003) 2989.
- [6] D. V. Louzguine-Luzgin, T. Saito, J. Saida, A. Inoue, *Journal Materials Research* 23 (2008) 515.
- [7] W. Zhang and A. Inoue, *J. Mater. Res.* 21 (2006) 234.
- [8] Q. Zhang, W. Zhang and A. Inoue, *Mater. Trans.* 48 (2007) 629.



Prof. Max LAGALLY
主任研究者 ラガリー・マックス

Silicon Nanomembranes

Max G. Lagally, University of Wisconsin-Madison
Madison, WI 53706 USA
lagally@engr.wisc.edu

Introduction

Silicon-on-insulator (SOI) is the source for a new class of nanostructures, Si nanomembranes (SiNMs). In SOI, a SiO₂ layer is interspersed between a thin crystalline top Si layer and the bottom Si wafer: the ability to etch this buried oxide selectively creates the membranes. When released from the oxide, this layered structure can form extremely flexible thin nanomembranes, with thicknesses from several 100 nm to less than 10 nm, which can be strain engineered and patterned to create various shapes (including sheets, tubes, spirals, and ribbons), depending on how one defines a pattern before release. [1-2] The opportunity to create nanomembranes exists for many other materials beyond Si and Ge: all that is required is a release layer, a layer that can be preferentially removed without damaging the material of the membrane. The strain is introduced into membranes by careful heteroepitaxial growth techniques.

Table 1 shows a summary of the novel features of Si nanomembranes and the properties that are or can be modified from those of bulk Si when Si is in the form of a thin membrane. The very high interface-to-volume ratio makes surfaces or interfaces potentially very important contributors to unique membrane properties. [3] The consequence is a wide variety of potential applications in sensors, photonics and optoelectronics, flexible electronics, and thermoelectrics. Even biological applications are likely. Furthermore, nano membranes are possible in other materials systems and may provide an entirely

Features	Modified properties
• Thin	• Surface
• Flexible, conformable	• Band structure, quantum properties
• Can be strain engineered	• Electronic transport
• Transparent	• Mechanical properties
• Transferable	• Dielectric properties
• Bondable, stackable	• Phononic properties
• Patternable (sheets, ribbons, tubes)	• Integration of modified properties

Figure 1. Key features of Si nanomembranes and a list of properties modified from those of the bulk when a thin crystalline sheet is considered.

new platform for nanomaterials applications. In the form of nanowires or nanoribbons (easily made by selective patterning before etching to release them) SiNMs may have a modified band structure and density of states if sufficiently small. Combined with the strong dependence of the conductivity on the surface, SiNMs in the form of ribbons may have significant potential as nanowire sensors or devices, in the same manner as proposed for carbon nanotubes and for nanowires produced by vapor-liquid-solid (VLS) growth, but in a much more controlled fashion.

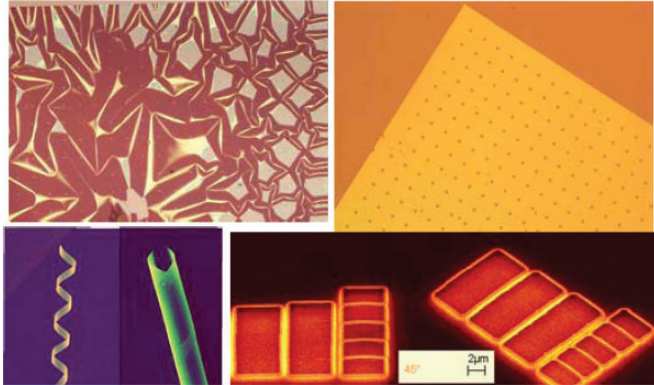


Figure 2. Si nanomembranes in various shapes, clockwise from top left: as released, crumpled but single-crystal; transferred to a new host substrate; patterned and etched into arrays of nanoribbons; and strain engineered and cut to make corkscrews or tubes.

Figure 2 shows optical images of SiNMs made from SOI(001) in various shapes – flatsheets, tubes, wires, and sheets that are warped, crumpled, or rippled; or smoothly curved.

All of them are single-crystal, with one, two, or three epitaxial layers. Membranes with more layers have also been made, and single- or multilayer membranes have been stacked on top of each other. The stacked membranes do not have an epitaxial relationship to each other, of course, but each membrane is a single crystal, with all layers in that membrane having an epitaxial relationship to each other.

Fabrication of Si nanomembranes

To fabricate elastically strained Si membranes from SOI(001) [4] a heteroepitaxial, strained SiGe layer is grown on the Si template layer of SOI. Because Ge has a 4% larger lattice constant than Si, a SiGe alloy layer grown epitaxially on unstrained Si will be compressed. The higher the Ge alloy concentration, the higher the compressive strain becomes in this layer, but to avoid dislocation formation, the layer must be thin. To create flat released membranes, an additional layer of Si is grown to balance the effect of the template Si layer when the structure is released. When this three-layer sandwich is still attached to the oxide, only the middle (SiGe) layer is strained. It cannot relax elastically until the structure is released from the oxide – at that stage the strain in the SiGe layer is shared elastically with the two Si layers on either side. They become tensilely strained while the SiGe becomes less compressively strained.

To release the membrane, the oxide layer is selectively removed by HF. HF attacks SiO₂ but not Si or Ge or their alloys. To increase the etch rate, access holes can be patterned in the layer sandwich before release. These etch holes are visible in the top two images in Fig. 2. The strain gets divided among the layers, with the strain in the Si layers of opposite sign as that in the SiGe layer; i.e., they are under tension. The SiGe cannot relax completely. The degree of strain in the Si is related to its thickness – the thinner, relative to the SiGe layer, the more strain.

While the use of SiGe as the straining layer always produces tensile strain in the Si layers and compressive strain in the SiGe layer, other materials combinations (e.g., a C-containing Si layer) could produce compressively strained Si. In non-group-IV materials, e.g., III-V materials, both outcomes (compressive or tensile top layer) are also possible.

Characterization and applications

Thinness and strain show dramatic effects in Si nanomembranes. Thinness causes changes in conductivity that are surprising and dramatic under the proper circumstances.[3] Strain in nanomembranes affects the electronic band structure. [5,6] Examples of these two phenomena are briefly described here.

When a doped semiconductor is made very thin, the total number of dopants per unit area becomes small. The sheet resistance thus naturally increases as the membrane gets thinner. If, in addition, there exist surface or interface states, the nature of the conductivity can change. For example, the number of dopants in one cm² of a 100nm thick Si membrane doped at 10¹⁵ cm⁻³ is 10¹⁰. There are ~10¹¹ cm⁻² states at an oxide/Si interface that can trap charge, depleting this Si membrane of mobile charge carriers. The membrane (and all thinner ones), behaves as if it were intrinsic. Such behavior can be observed [3]. Thus for thin enough oxide-covered Si membranes, the Fermi level will be determined by a competition between interface trap density and membrane “bulk” dopant concentration. This statement will be true for any materials system that has, relative to the dopant concentration, a sufficient density of interface states that can trap charge in the appropriate manner.

SiNMs with a surface oxide are therefore very good insulators at room temperature. They would be very good insulators even if the top oxide were replaced with another material that does not provide traps, because the bottom interface provides more than enough trap states. But if the top oxide layer is replaced with a layer that provides surface bands in appropriate positions in energy, conductivity can not only be restored to

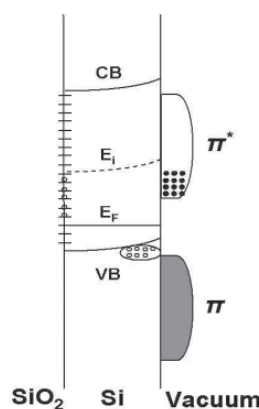


Figure 3. Schematic diagram of surface transfer doping in a semiconductor nanomembrane with interface trap states at one interface and an appropriate surface band at the opposite face.

what the value would have been for a bulk wafer doped at the same level, but it can be significantly enhanced. In Si(001) membranes, the simplest example is a clean surface. Si(001) surfaces form a 2x1 reconstruction to minimize the dangling bonds on the surface, consisting of π^* and π bands, each with the density of states of about $10^{15} \text{ cm}^{-2} \text{ eV}^{-1}$. These bands are positioned [7] approximately such that it is easy to excite electrons thermally across the gap (variously determined to be 0.35 to 0.6 eV) from the bulk valence band edge to the surface LUMO band than across the 1.1 eV bulk gap. Two parallel conducting paths, electrons on the surface and holes in the “bulk” of the Si membrane, can now contribute to the conductivity of the membrane system. This so-called surface transfer doping restores conductivity via “bulk valence band” holes even if the surface conduction is negligible (e.g., the surface electron mobility is small). Figure 3 shows a schematic diagram of the band structure that is associated with surface transfer doping. The number of states on the surface is approximately the number of atoms on the surface, hence 10^{14} to $10^{15}/\text{cm}^2$. That is a high doping level for a thin membrane and stays this large no matter how thin the membrane is made. In general, then, HOMO (highest occupied molecular orbital) or LUMO (lowest unoccupied molecular orbital) states localized in energy and appropriately positioned in energy with respect to the valence or conduction bands of the membrane provide for the thermal creation of high-mobility free carriers in the membrane. The deposition or adsorption of appropriate molecular or atomic layers on the surface could allow the same behavior outside a vacuum and create the potential for a new class of chemical and biological sensors. A schematic example of a possible sensor is shown in Fig. 4. It has not yet been possible to achieve the appropriate surface functionalization to provide the surface bands, but all elements of the idea are present in Fig. 4. If a surface band is created and charge can be either injected or removed from the band by specific adsorption of a biomolecule or toxin, the conductivity along the ribbon would change by many orders of magnitude.

As a second example we show characterization of the band structure changes that occur when Si is strained. In particular, we show the situation corresponding to our current SiNMs, i.e., tensile biaxial strain in the plane. The relevant parts of the Si band structure are shown in Fig. 5. In particular the conduction band minimum is affected by strain. Strain splits the 6-fold degeneracy of the

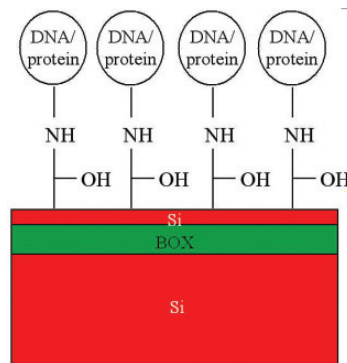


Figure 4. Schematic diagram of a membrane-based molecular sensor using change in the electrical conductivity in the thin Si sheet or ribbon as a molecule is specifically adsorbed.

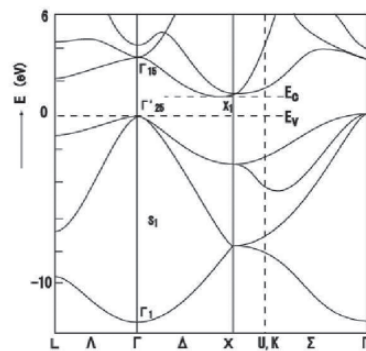


Figure 5. Band structure of Si, E vs. k.

minimum, reducing the intervalley scattering and thus raising the electron mobility by more than a factor of 2 if the strain is high enough.

A theoretical determination of the change in band gap with tensile or compressive strain is shown in Fig. 6 [8]. The Δ_4 and Δ_2 valleys at the X point split with strain. Both move to lower energies with tensile strain, but by different amounts. For compressive strain, they move to higher energies. The valence band also shifts, so that the band gap becomes smaller for both compressive and tensile strains. The availability of uniformly strained, defect-free Si membranes makes it possible to measure the strain dependence of features of the band structure. The required resolution demands a tunable source of x-rays with ~ 10 meV line width. Such x-ray sources require a synchrotron. We perform x-ray absorption spectroscopy using the University of Wisconsin Synchrotron to measure the shift in conduction band features with strain. Figure 7

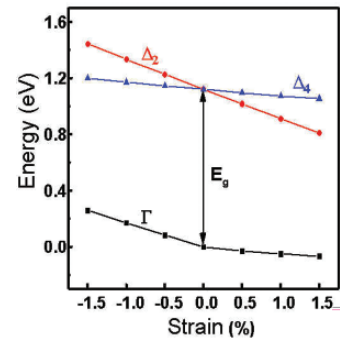


Figure 6. Calculated strain dependence of the band gap and the levels defining the band gap of Si [Feng Liu, to be published].

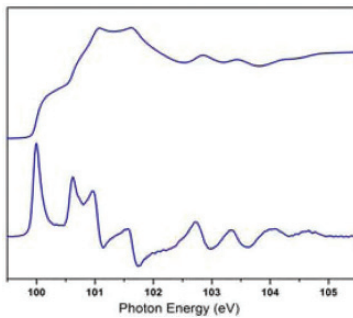


Figure 7. Absorption edge of SiNM. Lower curve is the derivative, showing the various levels of the conduction band that are accessible.

shows an absorption edge and the near-edge structure that is observable. Making these measurements as a function of the strain in a membrane and using the derivative spectra to identify the precise positions of peaks allows us to obtain band shifts with strain. We can therefore predict the band gap with strain.

Many other structural, chemical, mechanical, and electronic properties of membranes can be expected. Our research efforts are currently focused on exploring such properties in detail.

These unique properties allow many potential applications. We have already shown that we can make extremely fast flexible electronics, [9,10] stacked membranes for Bragg mirrors, [11] simple 2D photonic crystals, first-generation fast photodetectors, thermoelectric nanowires, and membrane materials for hybrid orientation and hybrid composition electronics. The opportunities are far-reaching both for fundamental science and for useful technology.

Summary

Single-crystal semiconductor membranes, at the dimensions discussed here, represent a new class of nanosystems with exceedingly large potential. In particular, the ability to introduce strain without defects, the ability to make thousands of identical structures using top-down approaches,

and the ability to integrate structures with different dimensionalities, different shapes, and different compositions make these systems very versatile. Nanomembranes can be made from other semiconductors and even non-semiconductors. The focus here has been on flat SiNMs, because their properties are both easier to understand and more near-term in their potential applicability than those of curled SiNMs.

Acknowledgements

I have greatly benefited from collaborations with and the efforts of G.K. Celler, M. M. Roberts, D. E. Savage, F. Liu, P.P. Zhang, H.C. Yuan, I. Knezevic, Z.Q. Ma, P.G. Evans, M.A. Eriksson, R. Blick, L. Klein, C. Ritz, F. Flack, S. A. Scott, and M.H. Huang. Aspects of the work to which this group of researchers contributed were variously supported by the USDOE, USAFOSR, USNSF, and Soitec, Inc.

References

- [1] M. H. Huang, C. Boone, M. M. Roberts, D. E. Savage, M. G. Lagally, N. Shaji, H. Qin, R. Blick, J. A. Nairn and F. Liu, *Adv. Mater.* **17** 2860 (2005)
- [2] For a review of early work, see S A. Scott and M.G. Lagally, *J. Phys. D.* **40** R1 (2007)
- [3] P. P. Zhang, E. Tevaarwerk, B. N. Park, D. E. Savage, G. K. Celler, I. Knezevic, P. G. Evans, M. A. Eriksson, and M. G. Lagally, *Nature* **439** 703 (2006)
- [4] M.M. Roberts, L.J. Klein, D.E. Savage, M. Friesen, K.A. Slinker, G. K. Celler, M.A. Eriksson, and M.G. Lagally, *Nature Materials* **5**, 388 (2006)
- [5] C. G. Van de Walle and R. M. Martin, *Phys. Rev. B* **34**, 5621 (1986)
- [6] C. Euaruksakul, Z. W. Li, F. Zheng, F. J. Himpsel, C. S. Ritz, B. Tanto, D. E. Savage, X. S. Liu, and M. G. Lagally, *Phys. Rev. Lett.*, in press.
- [7] J. E. Northrup, *Phys. Rev. B.* **47** 10032 (1993)
- [8] F. Liu, in preparation
- [9] E. Menard, K. J. Lee, D.-Y. Khang, R. G. Nuzzo, and J. A. Rogers, *Appl. Phys. Lett.* **84** 5398 (2004)
- [10] H.C. Yuan, Z.Q. Ma, M. M. Roberts, D. E. Savage, and M. G. Lagally, *J. Appl. Phys.* **100** 013708 (2006)
- [11] Weina Peng, M. M. Roberts, E. P. Nordberg, F. S. Flack, P. E. Colavita, R. J. Hamers, D. E. Savage, M.G. Lagally, and M. A. Eriksson, *Appl. Phys. Lett.* **90** 183107 (2007)



Assoc. Prof. Ken NAKAJIMA
准教授 中嶋 健

“Nanofishing of a Single Polymer Chain”

(Presentation at the 1st WPI & IFCAM Joint Workshop, Tohoku University)

Ken NAKAJIMA

Associate Professor, WPI - Advanced Institute for Materials Research

1. Introduction

Let's open the first page of the books for polymer physics or rubber physics.¹⁻³⁾ These books usually begin with the explanation of the origin of polymer chains' elasticity. It is not originated from energetic elasticity mainly possessed by solid-state materials such as a metallic spring but from so-called entropic elasticity. The entropic elasticity is the consequence of an essential property of polymer chains, *i.e.*, a single polymer chain being composed of a large number of unit constituents. Thus, even a single polymer chain can be treated by statistical mechanics. The calculation with a boundary condition that these constituents are bonded to each other to form a chain structure gives the final formula of entropic elasticity. This is the story developed during the era when a great advocate of polymer science, Prof. H. Staudinger, proposed that a single polymer takes the form of a linear string or chain molecule.

The entropic elasticity of a single polymer chain is treated similarly with the statistical mechanical property of gas molecules. Now, let's compare gas molecules to children moving around freely (with random speed and direction) in a schoolyard even though this situation is two-dimensional. Then, in the case of a single polymer chain, the children must move hand in hand as in a schematic illustration in a famous textbook of polymer physics (Figure 1).¹⁾ This is the only

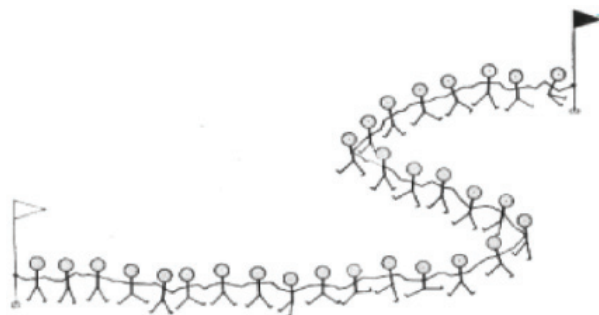


Figure 1 Drawing to help explain entropic elasticity.¹⁾

restraint condition for the children who become constituents of a polymer chain. If two adult men take the hands of the children at each end of the chain and they stand at fixed point, they must feel a very strong force. This is analogous to the restoring force of rubber, entropic elasticity. Higher temperature is equivalent to the children's cheerfulness. In fact, the entropic elasticity for a single polymer chain is calculated to be proportional to absolute temperature using a statistical mechanical treatment, ²⁾

$$F = \frac{3k_B T}{na^2} x, \quad (1)$$

where k_B is the Boltzmann constant and n and a are the number and size of the constituents (monomers, children), respectively. The front factor of x can be treated as the spring constant of rubbery elasticity, which obeys Hooke's law.

Some readers might be suspicious of the above description. Polymers are very small chain molecules and are under intense thermal motion. By using statistical mechanics, the spring constant of a single polymer chain can be calculated. Furthermore, this spring is not like a metallic spring but is entropic. However, who has observed it directly? Has anyone experienced pulling a single polymer chain as in the case of macroscopic rubber? The actual situation is that nobody has seen this theoretically equipped situation of the microscopic world. In any case, molecular-level rubber elasticity has been "a house of cards" based on the single polymer chain entropic elasticity without any experimental evidence.

The fact that rubber shows rubber elasticity was discovered more than hundred years earlier than Prof. H. Staudinger's proposal. The memory effect acquired by vulcanization, so-called Gough-Joule effect and its thermodynamic explanation were the great achievements in the nineteenth century. As seen in many textbooks, ¹⁻³⁾ this thermodynamic approach was the easiest one to gain consistency between ever-performed experiments and theory. In fact, thermodynamics of rubbery material can be treated in parallel with thermodynamics of gas. One could show experimentally that rubber elasticity was mainly dominated by entropic elasticity, which at present all of rubber researcher should know. However, the situation is almost the same with the case of a single polymer chain; nobody has seen the movement of chain molecules in rubbery materials as in the case of gas molecules.

In this report, I describe the experimental methods that can be used to answer this serious question; whether a single polymer chain really has entropic elasticity. For the purpose, I introduce the technique named as "single molecule force spectroscopy" or "nanofishing," where a single polystyrene chain as an example is stretched at its both ends in a solvent. The experiment was realized by atomic force microscope (AFM) ⁴⁾ that was invented in the late twentieth century. It has been possible to perform a real experiment for the conceptual experiment that appeared in the famous textbook written by Prof. P. G. de Gennes. ⁵⁾

2. Entropic Elasticity of Single Polymer Chain

2.1 Brief Introduction

The use of AFM has enabled us to visualize a small world consisting of atoms and molecules. Similar to reading Braille by tracing with a finger or tracking grooves with a needle in a phonograph record, AFM uses a very sharp probe tip (ultimately consisting of a single atom) to trace the surface of an object. For the reader's imagination, think of a scale with a length of 10 cm. A sharp spike of 5 mm long is attached at the end of the scale. Take another end and push the spike onto a desk. The stronger the force becomes, the larger the deflection of the scale. Then, move the assembly of the scale and the spike on the desk. The deflection changes in accordance with the surface topography. Raster scans over the two-dimensional surface thus reproduce a surface topographic image, which is the principle of AFM. By scaling down by a thousand times, the scale and the spike correspond to a cantilever and probe of AFM. The tip radius of the spike (10 μm) then corresponds to that of the probe (10 nm). If the AFM system detects a deflection of 10 nm (10 μm on the macroscopic scale), it becomes possible to detect a weak force. Since typical values of the spring constants of cantilevers become about 1 N/m or even less, the resolution of force detection reaches 1 nN.

By using AFM, we are able to visualize a single polymer chain, as many researchers have already reported. In practice, a single polymer chain looked like a piece of string.⁶⁾ It does not resemble a metallic spring at all. The recent study has revealed the dynamic movements of such strings.⁷⁾ Furthermore, dozens of researchers have placed their attention on the expanded capability of AFM as single molecule force spectroscopy. With this technology, the relationship between force and deformation of a single molecule sandwiched between a substrate and an AFM probe has been measured. A technique "nanofishing" introduced in this section comes under this category. Now, in the twenty-first century, we have obtained a novel method for experimentally verifying the statistical mechanics of a single polymer chain, which is indeed the basis of polymer physics. As in the case of stress-strain (S-S) curves of rubber, we can now investigate such curves for single polymer chains.

2.2 Static Nanofishing

According to the literature, trials on stretching single polymer chains by means of AFM have been extensively performed by many researchers as schematically shown in Figure 2. However, these trials have been especially dedicated to studies of "single protein unfolding" events,⁸⁻¹¹⁾ physisorbed macromolecules.¹²⁻¹⁵⁾ In the former case, proteins with modified ends were sandwiched via specific chemical bonds between a substrate and a cantilever and could be successfully stretched in the course of force-distance curve measurement by AFM. Those successes were attributed to two principal factors, the unique three-dimensional structures of proteins and the genetic engineering techniques for modifying the ends of proteins. Thus, picking points were controllably fixed.

From a comparison of such cases, synthesized polymers have many disadvantages. For instance, it is difficult to attach any reactive groups at their ends in general. Thus, the force-distance curve data obtained in uncontrolled experiments contain many complicated factors such as that the adsorptions occur not only at the tails but also at the loops. It is very difficult to judge whether the stretching event is really for a single polymer chain. The polydispersity also makes the situation very complicated. As described, however, successful nanofishing results on polystyrene (PS) chains with chemically active termini have been reported and thus several statistical analyses could be conducted to investigate the physical e polymer chain.^{16,17)}

A thiol-terminated PS was used as a sample in the experiment. It was based on a living polymerized carboxyl-terminated PS with $M_n = 93,800$ and $M_w = 100,400$. The polydispersity was $M_w / M_n = 1.07$. The degree of polymerization was about 900 and, thus, its contour length was about 220 nm. The thiol groups were substituted for the carboxylic ends using 1,10-decanedithiol by means of thiolester bonding, anticipating the preferential interaction between thiol and gold. No dimer formation was indicated from the result of gel permeation chromatography (GPC). The polymer was dissolved in a Θ solvent, cyclohexane, at $20 \mu\text{M}/\text{ml}$, and $10 \mu\text{l}$ of the solution was cast on a Au(111) substrate. After 5 min of incubation, the surface was rinsed with a pure solvent to remove weakly physisorbed molecules. These sample preparation procedures brought about well-dispersed (checked by AFM imaging, data not shown) chemisorption of polymer chains that possibly took on a random-coil form just like advertising balloons, which assured that the subsequent nanofishing measurements were on a single-molecule basis. The apparent size of the random-coil obtained by AFM imaging (data not shown), W , was about 40 nm. Then, by considering probe-shape convolution effect,¹⁸⁾ the deconvoluted size R_s could be calculated, with the formula of $W \approx 4\sqrt{R_s R_p}$, to be about 5 nm assuming that a probe radius, R_p , of 20 nm. The value was almost comparable with the radius of a single polymer chain. Indeed, the radius of a polymer random coil with $n = 900$ and $a = 0.25$ becomes $\sqrt{na} = 7.5$ nm. It was very rare to fish “two fish” at the same time. At this stage, it was speculated that, except for their modified termini, the interaction between a gold substrate and polymer chains would be weak enough for them to not strongly adsorb with collapsed or extended forms. Thus, this was the case of the adsorption of polymer chains to a

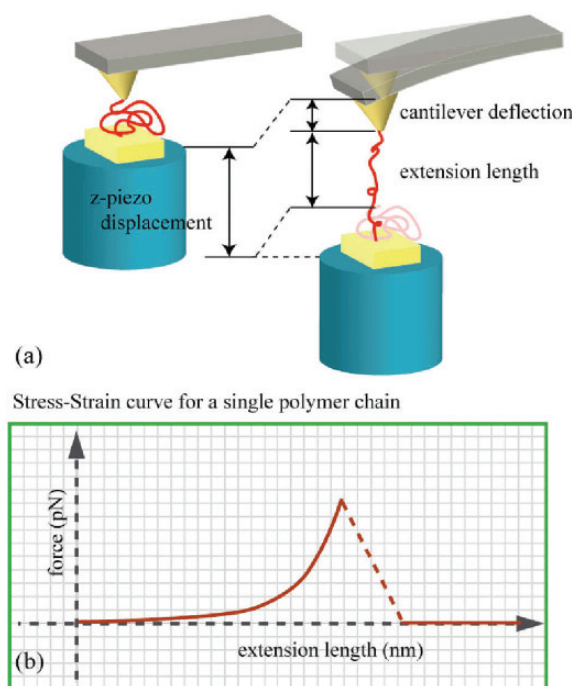


Figure 2 Concept of nanofishing, (a) schematic drawing and (b) force-extension (stress-strain) curve.

repulsive wall.⁵⁾

In addition to the use of cyclohexane, dimethylformamide (DMF) was used as a good solvent. So as to pick up the thiol- modified terminal, gold-coated cantilevers were used. The nominal values of their spring constant k_1 were 30 or 110 pN/nm. A typical force-extension curve measured in cyclohexane is shown in Figure 3.¹⁶⁾ The solvent temperature was kept at about 35°C, which corresponded to its Θ temperature for PS chains. Thus, a chain should behave as an ideal chain. The slope at the lowest extension limit (dashed line in Figure 3) was 1.20×10^{-4} N/m. The value should be that of single polymer chain elasticity caused by entropic contribution. At first glance, the force data fluctuated a great deal. However, this fluctuation was due to the thermal noise imposed on the cantilever. A simple estimation told us that the root-mean-square (rms) noise in the force signal ($\Delta F \sim 15.6$ pN) for an extension length from 300 to 350 nm was comparable with the thermal noise, $\Delta F = (k_1 k_B T)^{1/2} \sim 21.6$ pN.

As for further analysis, curve fitting against the worm-like chain (WLC) model was conducted and indicated as a solid line in Figure 3. The model describes single polymer chain mechanics ranging from random-coil to fully extended forms, as follows:

$$F(x) = \frac{k_B T}{l_p} \left[\frac{1}{4(1-x/L)^2} + \frac{x}{L} - \frac{1}{4} \right], \quad (2)$$

where x is the extension length at an external load of F . l_p and L are persistence and contour lengths, respectively. The fitting results were $l_p = 0.31 \pm 0.01$ nm and $L = 284.5 \pm 0.8$ nm. The persistence length almost corresponded to the length of a single monomer. The degree of polymerization was then calculated from these two intrinsic values to be about 918, which was in good agreement with the expected value from the synthesis information. Actually, a histogram of contour length made by dozens of successful fishing results showed a single peak with good coincidence with the GPC result. Another estimation was made with the following equation derived from Eq. (2) for condition $x \ll L$:

$$\left. \frac{dF}{dx} \right|_{x \rightarrow 0} = \frac{3k_B T}{2l_p L}. \quad (3)$$

The substitution of l_p and L resulted in a spring constant of 0.71×10^{-4} N/m for single

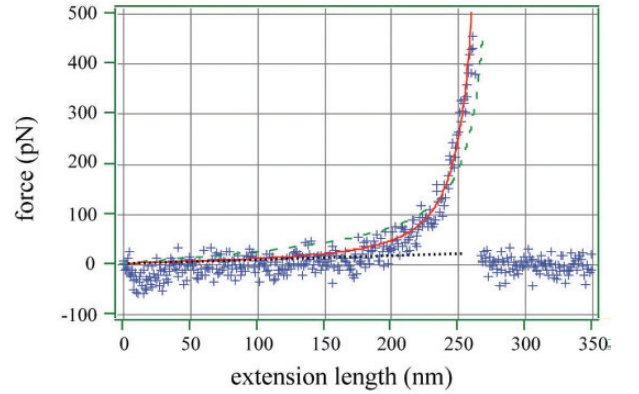


Figure 3 Nanofishing of a single PS chain in cyclohexane. The solvent temperature was about 35°C (Θ temperature). A cantilever with a 110 pN/nm spring constant was used. The WLC (Worm-Like Chain, solid line) and the FJC (Freely Jointed Chain, dashed line) models were used to obtain fitting curves.¹⁶⁾

polymer chain elasticity, which was almost equivalent to the experimentally obtained slope value, 1.20×10^{-4} N/m, and the value obtained by the simplest form, 1.45×10^{-4} N/m ($n = 918$ and $a = 0.31$ nm for Eq. (1)). These comparisons implied that the measurements were consistent with the theoretical predictions. The deviation between the rupture length of 260.9 nm and the fitted contour length indicated that the polymer chain was not fully stretched at the rupture event. The reason for this was that the rupture event was a stochastic process and was dependent on many factors such as pulling speed, bond strength, and temperature. The validity of the freely jointed (FJC) model (dashed green line) was also checked:

$$\frac{F(x)l_K}{k_B T} = \mathcal{L}^{-1}\left(\frac{x}{L}\right), \quad \mathcal{L}(y) = \coth y - \frac{1}{y}, \quad (4)$$

where l_K is the Kuhn length and $\mathcal{L}(y)$ is the Langevin function. It was obvious that the FJC model did not represent the experimental result well. Thus, nanofishing could be used to judge the ever-present basic theories of polymer physics.

Further examinations by changing solvent temperature and solvent type proved to be useful in order to reveal statistical mechanical properties such as the second virial coefficient on a single polymer chain basis.^{16,17)} Such properties have normally been investigated by light scattering or osmotic pressure as averaged information from an ensemble of many polymer chains. Detailed discussions are given in the literature and readers are strongly recommended to refer them, while differences in solvent qualities cause differences in the conformations of single polymer chains, resulting in observable changes in force-extension curves. The results seemed to be explained well by Flory's lattice model, at least as the first approximation.¹⁹⁾

In a poor solvent (cyclohexane at 5°C), a polymer chain takes on a condensed globular state because constituent molecules are repulsed by the solvent molecules. Nanofishing of this chain revealed a perfectly different force-extension curve, as shown in Figure 4. It was observed that constant force continued from about 30 to 130 nm after non-specific adsorption between a substrate and a probe. This phenomenon could be related to the extraction of monomers one by one from a collapsed globule into a stretched strand, which was numerically predicted by M. Wittkop and coworkers.²⁰⁾ Using Monte Carlo simulation, they examined the deformation behavior of a single polymer chain below the Θ temperature, thus the poor region. This type of measurement is not

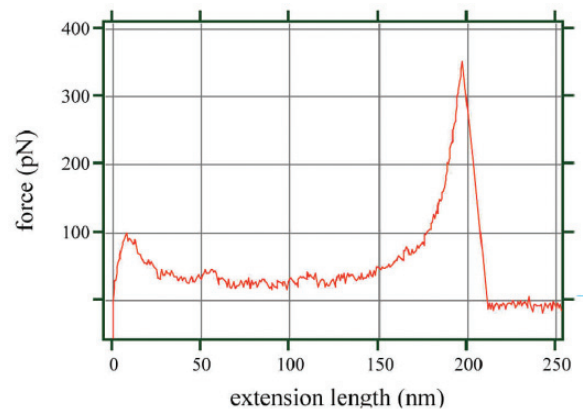


Figure 4 Nanofishing of a single PS chain in cyclohexane at 5 °C (poor region). A cantilever with a 30 pN/nm spring constant was used. The coil-strand coexistence was revealed in the extension range of 30 to 130 nm.

possible by ensemble-averaged measurements, and nanofishing is the only tool that can be used. As seen, nanofishing seems to have a very promising future. However, there are several drawbacks to be solved. For example, it is difficult to define the transverse section perpendicular to the extension direction and therefore stress that is defined as force divided by section area. It is also difficult to discuss Poisson's ratio, though these definition themselves may be unnecessary. If an ultimate goal is the measurement of single polymer chain elasticity inside a practical rubbery material, the current status that the measurement must be performed in liquid condition would be severe problem together with the above-mentioned difficulty for uncontrolled physisorption-based experiments.

Before closing this section, we would like to introduce an experiment that checks the validity of the hypothesis of whether nanofishing is performed in a quasistatic condition. The force-extension curve in Figure 3 was taken at a pulling speed of $2 \mu\text{m/s}$. Under this condition, no change in force was observed if extension was stopped at a certain point before rupture. Thus, it could be tentatively regarded that the condition was near equilibrium. In contrast, the curve in Figure 5 gave an apparent deviation from the former result.²¹⁾ In this experiment, a single polymer chain was exposed to a sudden, stepwise stress-increase of maximum 1500 pN with the speed of 500 pN/ms

for four times before rupture as in the case of the macroscopic creep measurement. In this case, the pulling speed corresponded to about $17 \mu\text{m/s}$, 8.5 times faster than the former measurement. A sudden increase in force with almost "no" deformation of the polymer chain was observed for each part. It was speculated that this phenomenon was due to topological constraint, *i.e.*, internal entanglement of a polymer chain. The relaxation of this constraint was also found in each successive response. Further studies are necessary to explain the observed result. Nevertheless, we could conclude from this experiment that the result obtained in Figure 3 was for a quasi-static condition because the curve merely shows mild, gradual changes in contrast to that in Figure 5. In addition, we should note that the curve in Figure 5 might have a certain relationship with the hysteresis observed in the S-S curve for macroscopic rubbery materials since we never observe any hysteresis for quasi-static nanofishing.

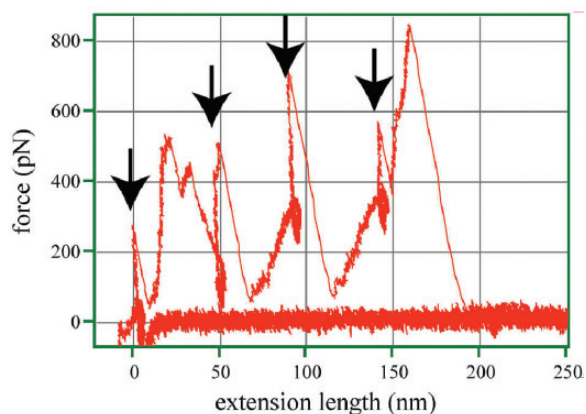


Figure 5 Nanofishing with a very fast pulling speed (about $17 \mu\text{m/s}$) for a single polystyrene chain in DMF.

A cantilever with a 30 pN/nm spring constant was used.

2.3 Dynamic Nanofishing

In the previous section, we showed that static nanofishing merely gave static information about polymer chains. Therefore, viscoelasticity, which is a quite important property of polymers, seldom appears. Why do polymer solutions have viscosity? How does an elastomeric isolator

absorb the energy created by earthquakes? It is possible to ascribe these qualities to the viscosity of polymers. Incidentally, there is a model to describe polymeric viscoelasticity, which is composed of a single spring and a single dashpot (device composed of piston, cylinder, and viscous fluid, which gives resistance proportional to velocity). Let's say that the model is an extremely simplified one that can reproduce only a single relaxation event. Where are the spring and dashpot? What does a dashpot look like? These are frequently asked questions by many students. The students do not understand that the model is just a phenomenological one. As explained, a single polymer chain does not necessarily take the form of spring. In the same way, we do not find dashpot structures on a microscopic scale. The phenomena modeled by dashpots are several frictional contributions such as internal friction between neighboring segments (monomers) during rotational movement with respect to bonding axis, the friction between segments and solvent molecules, and the friction between segments during cooperative movement in polymer "spaghetti." These origins have their own time constants. Thus, the use of the phenomenological model requires thinking about the kinds of interaction that take place. In any case, the frictional or energy-dissipative processes are of great importance in applying polymers to realistic industrial applications. Thus, the origins must be explained experimentally. Here, we introduce a potential technique of revealing monomer-solvent friction for a single polymer chain.²²⁾

The experimental setup was almost same as that for the static measurement, while the cantilever was now vibrated at its resonant frequency in liquid ($f_1 = \omega_1/2\pi = 9.03$ kHz). A gold-coated cantilever was again used and its spring constant was experimentally determined by the thermal noise method ($k_1 = 29.6$ pN/nm).²³⁾ The RMS oscillation amplitude was $A = 6.0$

nm when free oscillation (no interaction with a polymer or a substrate) was reached. In the case of successful nanofishing, the RMS amplitude decreased as in the case of the tapping-mode operation. The phase shift between input and output signals also deviated from 90° , which was the value for free resonance. The change in boundary condition by polymer chain attachment caused a change in the free oscillation of the cantilever.

To obtain information about the mechanical properties of a single polymer chain, the separation-dependent RMS amplitude and phase shift changes (data not shown) were analyzed based on the phenomenological model depicted in Figure 6. Assuming sinusoidal drive of the cantilever base $z_d(t) = A_d e^{i\omega t}$ with drive amplitude A_d and drive frequency ω , the deflection of the cantilever as a sinusoidal response can be written as $z(t) = A e^{i(\omega t + \theta)}$ with amplitude A and phase shift θ . The cantilever is represented by an effective tip mass together with a spring and dashpot

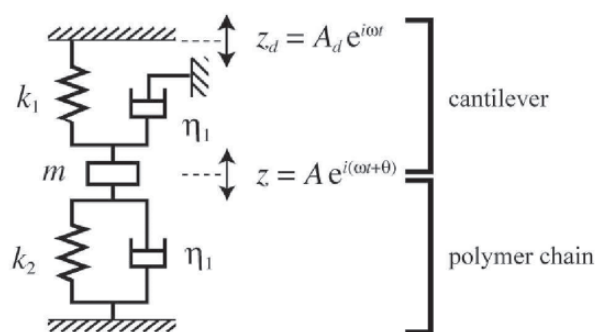


Figure 6 A double-Voigt model depicting measurement of dynamic nanofishing.

connected in parallel (Voigt element), which are characterized by mass m , spring constant k_1 , and damping coefficient η_1 . Here, the damping is due to the viscous drag by the surrounding medium and the intrinsic damping caused by the deflection of the cantilever beam. A polymer chain is also described as a Voigt element, which has a spring k_2 and dashpot η_2 connected in parallel; the mass of a molecule is so small compared to the tip mass that it is ignored. The two parameters, k_2 and η_2 , are what we are interested in.

Analysis started from the following equation of motion:²⁴⁾

$$m\ddot{z}(t) + (\eta_1 + \eta_2)\dot{z}(t) + (k_1 + k_2)z(t) = k_1 z_d(t). \quad (5)$$

Parameters η_1 and m were obtained from the spring constant of the cantilever k_1 ($= 29.6$ pN/nm), resonant frequency ω_1 ($= 2\pi f_1 = 21.2$ kHz), and quality factor Q ($= 25$), as follows:

$$m = \frac{k_1 \sqrt{Q^2 - 1}}{Q\omega_1^2}, \quad \eta_1 = \frac{k_1}{Q\omega_1}. \quad (6)$$

Note that these values were determined during the cantilever tuning process and were therefore independent of the stretching event. Although detailed calculation is omitted, k_2 and η_2 could be calculated from the solution of Eq. (5):

$$k_2 = \frac{A_1}{A} \{ (-m\omega_1^2 + k_1) \cos\Delta + \eta_1 \omega_1 \sin\Delta \} - (-m\omega_1^2 + k_1), \quad (7)$$

$$\eta_2 = \frac{A_1}{A\omega_1} \{ \eta_1 \omega_1 \cos\Delta - (-m\omega_1^2 + k_1) \sin\Delta \} - \eta_1, \quad (8)$$

where A_i is the oscillation amplitude without the polymer chain and Δ is the difference in phase shift with (θ) and without (θ_i) the polymer chain ($\Delta = \theta_i - \theta$). Amplitude and phase shift in the approaching process are regarded as A_i and θ_i .

Figure 7 shows the obtained result. The stiffness of a single chain k_2 (Figure 7a) increased abruptly with stretching. This is commonly observed in conventional simple stretching experiments on polymers, as in Figure 3, *i.e.*, an almost constant value for spring constant at low extension and an apparent increase due to the fully stretched effect caused not only by entropic contribution but also by enthalpic contribution such as bond angle constraint. The average value of k_2 in the low extension region was 2.86×10^{-5} N/m. A new result, only available by dynamic nanofishing for the frictional coefficient, which might be related to viscosity, was obtained as shown in Figure 7b. At

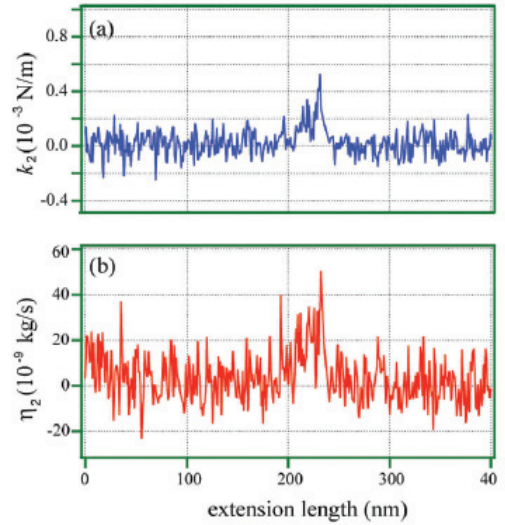


Figure 7 The behavior of (a) chain stiffness, k_2 and (b) viscosity of the chain, η_2 against the extension. The values of k_2 and η_2 were calculated by a double-Voigt model.

first glance, almost zero viscosity was observed in the low extension region. However, viscosity had a certain value in this region. From Figure 7b, viscosity η_2 in the region (30-150 nm) averaged 2.62×10^{-9} kg/s. Note that this value is the first estimation of viscosity on a single polymer chain basis in a low extension region.

It was also found that the viscosity also increased in the same manner as in k_2 . There have been many theoretical descriptions for polymer-solvent friction.^{1, 5, 19)} As an extreme case, a single polymer chain is treated as a rigid sphere with a certain hydrodynamic radius. The radius must be correlated to Flory's radius, R_F .²⁵⁾

$$f_{\text{Kirkwood}} = 6\pi\eta_s R_F \frac{d\mathbf{r}}{dt}, \quad (9)$$

where η_s is solvent viscosity. In contrast, there is a theory called the free-draining model where all constituents of a single polymer chain are exposed in a solvent flow.²⁶⁾

$$f_{\text{Rouse}} = \zeta_s n \frac{d\mathbf{r}}{dt}, \quad (10)$$

where ζ_s and n are the frictional coefficient between a constituent monomer and a solvent molecule and the number of monomers, respectively. It seemed that the experimental result contradicted the assumption of the free-draining molecule, which ought to be treated as the first approximation of polymer chains interacting with solvent molecules because the increase in viscosity in the higher extension region was never explained by this simple additivity. The increase might be related to an increase in the number of constituent molecules exposed to solvent friction. Further studies with improved signal-to-noise ratios are necessary to explain this point including comparison with more sophisticated theories that can treat solvent flow inside a random coil and an extended chain form.⁵⁾

Up to here, the discussion has seemed to assume that viscosity η_2 determined by dynamic nanofishing is due to solvent friction, an idea that is not groundless. To verify this assumption, the dependence of η_2 on solvent temperature and quality was investigated. There is a well-accepted concept to describe polymer solution viscosity, intrinsic viscosity $[\eta]$. Values have been accumulated for different polymer species, solvent qualities, and temperatures by conventional techniques such as light scattering and osmotic pressure.

$$[\eta] = \lim_{c \rightarrow 0} \frac{\eta_{sp}}{c} = KM^\alpha \quad (11)$$

As is seen, $[\eta]$ is the value of specific viscosity, $\eta_{sp} = (\eta - \eta_s) / \eta_s$, is extrapolated to an infinitely dilute condition, where η , c , and M are solution viscosity, concentration, and molecular weight, respectively. K and α are constants depending on polymer species, solvent quality, or temperature.²⁷⁾ Although the units of $[\eta]$ and of η_2 were different, it was considered that the origin of both parameters was the same to each other. This was because both parameters represented viscosity in an infinite dilute polymer solution. Thus, the coefficient of the viscosity-molecular weight relationship was chosen as the property for comparison. Assumed that there exist a constant

K' satisfying the following relationship:

$$\eta_2 = K'M^\alpha. \quad (12)$$

To compute constant K' from the experimental data, molecular weight M was calculated from the contour length obtained by WLC fitting against the force-extension curve (data not shown, however, obtained together with the curves in Figure 7), and a constant α was determined by reference data.²⁷⁾ The temperature dependence of the viscosity constant K' and corresponding reference data K are shown in Figure 8. Viscosity constants K' and K were divided by those in Θ solvent K'_Θ and K_Θ for scaling, respectively. Experimental and reference data showed good agreement with each other. This agreement supports the idea that the viscosity measured here clearly depends on solvent conditions as well as intrinsic viscosity. Taking the increase in viscosity in the high extension region into account, it would be concluded that viscosity under 10 kHz perturbation was attributed to monomer-solvent friction. The investigation of molecular weight dependence will also help in checking the validity of the analysis. The realization of such an experiment is expected.

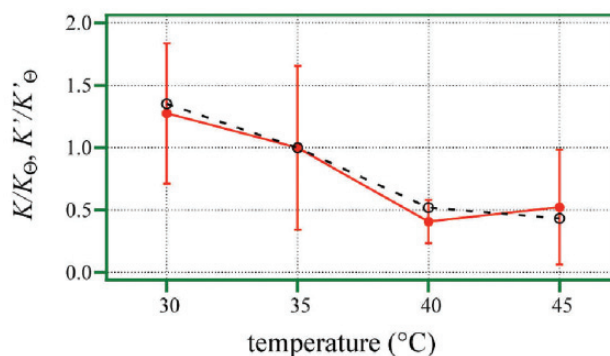


Figure 8 Temperature dependence of the viscosity constant K' (solid) and K (dashed). Both constants are divided by those in Θ solvent for scaling.

3. Summary

To close the section, it is worth mentioning the possible future direction of anofishing experiments. The leading person in this field, Prof. H. E. Gaub and coworkers realized a kind of heat engine using a photosensitive single polymer chain.¹⁵⁾ They used the cis-trans isomerization of an azobenzene polymer to convert photochemical energy into mechanical energy. Of course, industrial application of this technique is not simple, while the research gives us a kind of dream that nanofishing will open a promising future. In the past, studies on a single polymer chain had been preceded by theoretical work. However, we believe that in the twenty-first century, experimental studies will take the initiative in this field.

References

- 1) Saito, N: “*Polymer Physics (in Japanese)*”, Syokabo, Tokyo, Japan (1967)
- 2) Kubo, R.: “*Rubber Elasticity /the reprint of the first edition (in Japanese)*”, Syokabo, Tokyo, Japan (1996)
- 3) Treloar, L.R.G.: “*The Physics of Rubber Elasticity*”, Oxford University Press, Oxford, UK

(1975)

- 4) Binnig, G., Quate, C. F., Gerber, Ch., Weibel, E.: *Phys. Rev. Lett.*, **56**, 930 (1986)
- 5) de Gennes, P. G.: “*Scaling Concepts in Polymer Physics*”, Cornell University Press, New York, USA (1979)
- 6) Kumaki, J., Nishikawa, Y., Hashimoto, T.: *J. Am. Chem. Soc.*, **118**, 3321 (1996)
- 7) Ando, T., Kodera, N., Naito, Y., Kinoshita, T., Furuta, K., Toyoshima, Y.: *Chemphyschem.*, **4**, 1196 (2003)
- 8) Mitsui, K., Hara, M., Ikai, A.: *FEBS Lett.*, **385**, 29 (1996)
- 9) Rief, M., Oesterhelt, F., Fernandez, J. M., Gaub, H. E.: *Science*, **276**, 1109 (1997)
- 10) Dietz, H., Rief, M.: *PNAS*, **101**, 16192 (2004)
- 11) Wang, T., Sakai, Y., Nakajima, K., Miyawaki, A., Ito, K., Hara, M.: *Colloid Surf.*, **B40**, 183 (2005)
- 12) Cortiz C., Hadziioannou, G.: *Macromolecules*, **32**, 780 (1999)
- 13) Li, H., Zhang, W., Xu, W., Zhang, X.: *Macromolecules*, **33**, 465 (2000)
- 14) Haupt, B. J., Senden, T. J., Sevick, E. M.: *Langmuir*, **18**, 2174 (2002)
- 15) Holland, N. B., Hugel, T., Neuert, G., Scholz, A. C., Renner, C., Oesterhelt, D., Moroder, L., Seitz, M., Gaub, H. E.: *Macromolecules*, **36**, 2015 (2003)
- 16) Nakajima, K., Watabe, H., Nishi, T.: *Polymer*, **47**, 2505 (2006)
- 17) Nakajima, K., Watabe, H., Nishi, T.: *Kautsch. Gummi Kunstst.*, **5**, 256 (2006)
- 18) Vesenka, J., Guthold, M., Tang, C. L., Keller, D., Delaine, E., Bustamante, C.: *Ultramicroscopy*, **42-44**, 1243 (1992)
- 19) Flory, P. J.: “*Principles of Polymer Chemistry*”, Cornell University Press, New York USA (1953)
- 20) Wittkop, M., Kreitmeier, S., Goeritz, D.: *Phys. Rev. E*, **53**, 838 (1996)
- 21) Nakajima, K., Watabe, H., Ohno, N., Nagayama, S., Watanabe, K., Nishi, T.: *J. Soc. Rubber Ind., Jpn.* (in Japanese), **79**, 466 (2006)
- 22) Watabe, H., Nakajima, K., Sakai, Y., Nishi, T.: *Macromolecules*, **39**, 5921 (2006)
- 23) Hutter, J. L., Bechhoefer, J.: *Rev. Sci. Instrum.*, **64**, 1868 (1993)
- 24) Anczykowski, B., Gotsmann, B., Fuchs, H., Cleveland, J. P., Elings, V. B.: *Appl. Surf. Sci.*, **140**, 376 (1999)
- 25) Kirkwood, J. G., Riseman, J.: *J. Chem. Phys.*, **16**, 565 (1948)
- 26) Kramers, H. A.: *J. Chem. Phys.*, **14**, 415 (1946)
- 27) Brandrup, J., Immergut, E. H.: “*Polymer Handbook: 3rd ed.*”, Wiley Interscience, New York, USA (1989)



Assoc. Prof. Taro HITOSUGI
准教授 一杉 太朗

Development of TiO₂-based transparent conductor

Taro Hitosugi
WPI-AIMR, Tohoku University

ABSTRACT

We, here, report on the development of TiO₂-based transparent conducting oxide (TCO) which is a promising candidate for next-generation transparent electrode. Anatase Nb-doped TiO₂ (Ti_{1-x}Nb_xO₂) epitaxial thin films with $0.03 \leq x \leq 0.06$ shows resistivity ρ of $2-3 \times 10^{-4} \Omega\text{cm}$ and internal transmittance of $\sim 95\%$ in the visible light region. Further, we demonstrate polycrystalline films deposited on glass with $\rho = 4.6 \times 10^{-4} \Omega\text{cm}$ at room temperature. These values are comparable to those of typical TCOs, In_{2-x}Sn_xO₃ (ITO). We also present the recent progress on sputter-deposited TiO₂-based TCO on glass substrate and discuss unique characteristics of this material, such as high refractive index, high transmittance in infrared, and high stability in reduced atmosphere.

Introduction

Transparent conducting oxide (TCO) exhibits two properties at once, namely, high optical transmittance and high electrical conductivity. It has been an essential part of devices that require

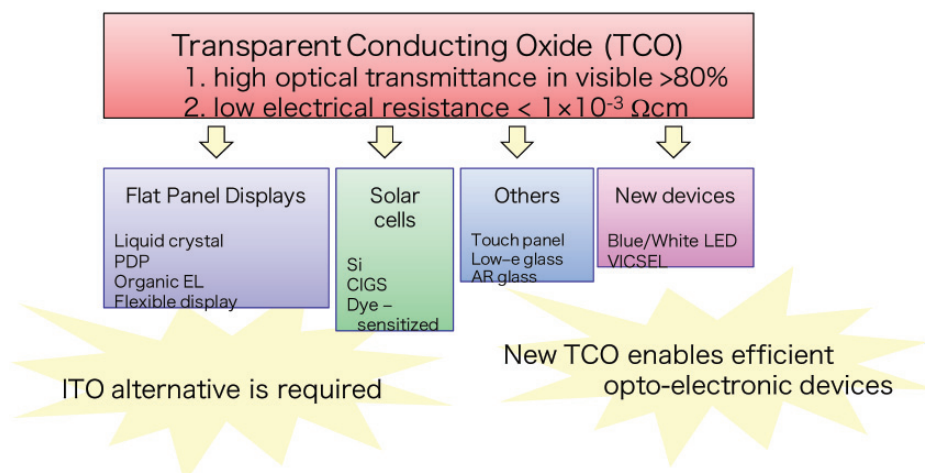


Fig. 1 Wide spread usage of transparent conducting oxides (TCO).

electrical contact and optical access, such as flat panel displays (FPDs), light emitting diodes (LEDs), and solar cells (Fig. 1).^{1,2} Currently, Sn-doped indium oxide (ITO) is the most widely used TCO, because of its high transparent conducting properties^{3,4} and its easiness for preparation. There is, however, a strong demand to search for a new TCO from two backgrounds. One is that since TCO is a key component in opto-electronic devices, various characteristics are required in emerging devices. For example, if there is a TCO with high refractive index, brighter GaN-based LED would be available. Solar cells and organic LED has similar problem, and if suitable TCO is developed, more efficient devices would be possible. The other background is the unstable supply of indium, since its demand is continuously expanding. These backgrounds motivate us to develop a new transparent conducting oxide. Although ZnO, SnO₂ and many kinds of multicomponent materials have been investigated as ITO alternatives,⁵ exploring new materials should be more encouraged in view of the increasing request for novel applications of TCOs.

In this article, we report on the development of a new TCO, anatase Ti_{1-x}Nb_xO₂ (TNO),^{6,7} which possess electrical and optical properties comparable to those of ITO. Anatase TiO₂ is suitable as a mother compound of next-generation TCO, because it is characterized by a wide band gap (3.2 eV)⁸ and relatively low effective mass $\sim m_0$ (m_0 : free electron mass).⁹ This TNO has properties that ITO does not have, such as, high refractive index, high transmittance in infrared, and high stability in reduced atmosphere. These properties would provide new optoelectrical devices, as witnessed in the role of ITO in FPDs. Moreover, titanium, being the major constituent of TNO is much more abundant in the earth's crust, approximately a factor of 10⁵, than indium.¹⁰

Titanium dioxide (TiO₂)

Titanium dioxide (TiO₂) has been intensively studied over the last decades because of its interesting technological applications, such as for catalysis¹, pigment², and sensors³. More recently, TiO₂ has been attracted researchers from the interest in the applications for high-k materials,¹¹ resistive random access memory (RRAM),¹² and spintronics.¹³ Among many polytypes of TiO₂, technologically important crystal structures are rutile and less dense structure, anatase (Figs. 2(a) and (b)). Of these phases, rutile phase has been extensively studied. The reason is that most crystal growth techniques yield TiO₂, basically in the rutile phase. Crystal growth of anatase is difficult because it is not the most stable structure in

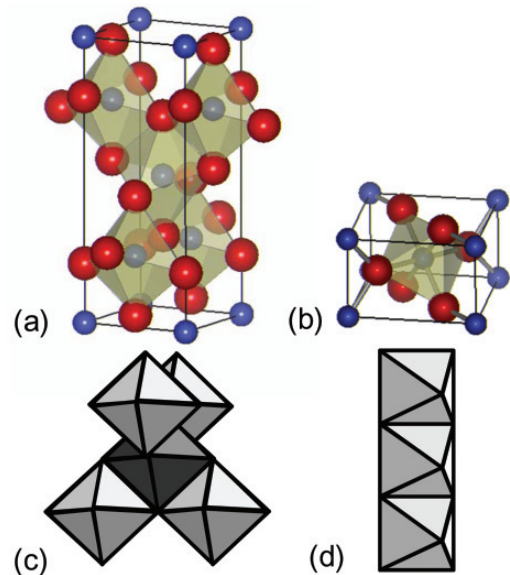


Fig. 2 Crystal structures of (a) anatase and (b) rutile, and schematic view of the network of TiO₆ octahedra for (c) anatase and (b) rutile. Red and blue balls denote Ti and O, respectively.

bulk form, and the first report on the growth of single crystals were from Lévy *et al.*¹⁴ Both rutile and anatase crystallizes in a tetragonal phase, and the structure of rutile and anatase crystals can be described in terms of chains of TiO_6 octahedra. The two structures differ by the distortion inside each octahedron and by their network of octahedra. Each Ti^{4+} ion is surrounded by an octahedron of six O^{2-} ions. In an anatase structure, each octahedron is in contact with eight neighbors (four sharing an edge and four sharing a corner) (Fig. 2(c)), while in a rutile structure, the coordination number is 10 (two sharing an edge and eight sharing a corner) (Fig. 2(d)).

A conventional method for controlling resistivity (ρ) of TiO_2 is to introduce oxygen deficiency δ , as expressed as $\text{TiO}_{2-\delta}$, by growing or annealing films under reducing atmosphere. In this way, the n-type carrier density, n_e , of TiO_2 is controllable by amount of δ . Empirically, however, the obtained oxygen-deficient films tend to lose transparency, so that they are not applicable to TCOs. Recently, we demonstrated a different and more effective way of carrier doping into anatase TiO_2 , substitution of Nb for Ti.^{6,7} Nb is soluble to anatase TiO_2 up to 20%, and Nb ions, existing as Nb^{5+} , release conduction electrons with an efficiency of >90%. By using this Nb-doping technique, therefore, it is possible obtain highly conducting transition metal doped TiO_2 . Further, the Nb-doping technique combined with the annealing procedure enables us to achieve high electrical conductivity and high transparency at the same time even in polycrystalline films on glass substrate.

Nonmetal – metal transition & Transparent conducting properties

Figure 3(a) shows the ρ of $\text{Ti}_{1-x}\text{Nb}_x\text{O}_2$ epitaxial thin films as a function of x . Undoped anatase TiO_2 shows ρ in the order of $10^{-1} \Omega\text{cm}$, and doping Nb result in the drastic drop of ρ , showing minimum at $x = 0.06$. These anatase epitaxial thin films were grown by pulsed laser deposition (PLD) technique on $\text{SrTiO}_3(100)$ or $\text{LaAlO}_3(100)$ substrates,^{6,7} and X-ray diffraction (XRD) confirmed the

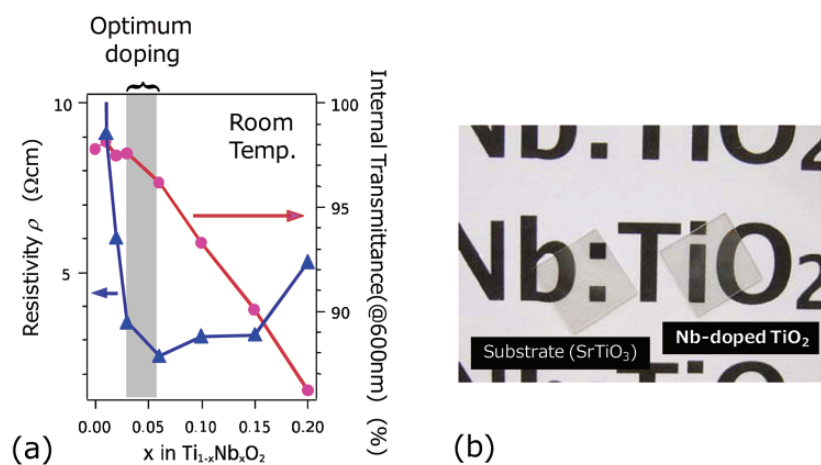


Fig. 3 (a) Resistivity and internal transmittance (@ 600 nm) of $\text{Ti}_{1-x}\text{Nb}_x\text{O}_2$. (b) Appearance of $\text{Ti}_{0.94}\text{Nb}_{0.04}\text{O}_2$ epitaxial thin film on $\text{SrTiO}_3(100)$ substrate.

single phase growth of anatase. Fig. 3(a) also shows the internal optical transmittance at 600 nm obtained from measuring extinction coefficient. The transmittance gradually decreases on doping Nb. What we found is that there is an optimum doping x that can achieve both high electrical conductivity and high optical transmittance. It should be emphasized here that the ρ values of optimally doped films, $0.03 \leq x \leq 0.06$, are as low as $2 - 3 \times 10^{-4} \Omega\text{cm}$, which are comparable to those of conventional ITO films.^{3,15} Fig. 3(b) shows the appearance of SrTiO₃ substrate with and without films.

These highly conductive films are characterized by degenerate semiconductor with metallic temperature dependence of ρ . Figure 4(a) plots carrier density, n_e , against x . As can be seen, there is good linear relation between n_e and x up to $x \sim 0.06$, which can be formulated as $n_e \sim 0.9n_{\text{cation}}$, where n_{cation} is the density of Nb. This provides the evidence that Nb ions release conduction electrons with an efficiency of $\sim 90\%$. At higher doping level, $x > 0.06$, the ionization efficiency is slightly suppressed. The Hall mobility, μ_H , increases as temperature is lowered, and indicates the importance of phonon scattering (Fig. 4(b)). The $0.03 \leq x \leq 0.06$ films with optimal electric and optical properties possess μ_H (300 K) $\sim 20 \text{ cm}^2\text{V}^{-1}\text{s}^{-1}$, which is approximately half of that of ITO with the same dopant concentration.

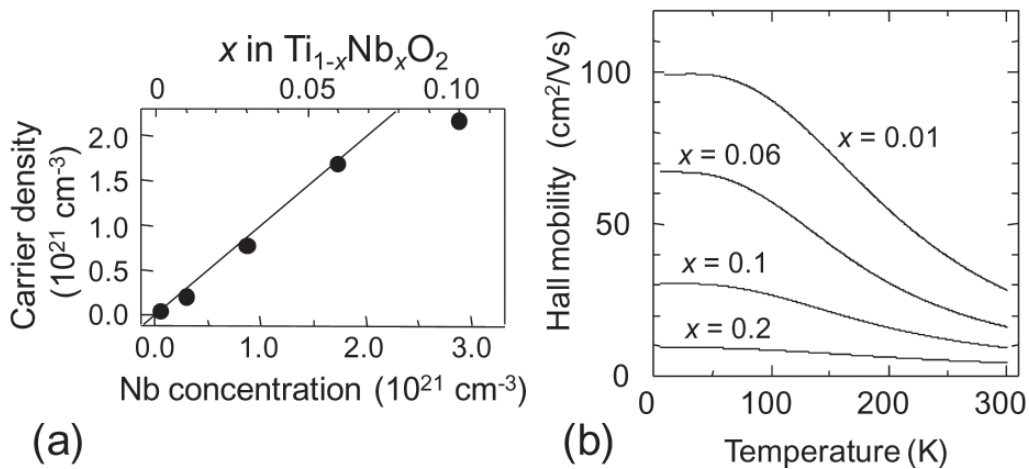


Fig. 4 (a) Carrier density at 300 K as a function of Nb concentration and x . (b) Hall mobility as a function of temperature.

The above experimental results demonstrates that Nb-doped anatase TiO₂ ($\text{Ti}_{0.94}\text{Nb}_{0.06}\text{O}_2$: TCO) in epitaxial thin film form, is an excellent TCO with high conductivity, $\rho \sim 2 \times 10^{-4} \Omega\text{cm}$ and internal transmittance $>95\%$ in visible. These values are comparable to those of typical TCOs such as indium tin oxide (ITO) and ZnO, indicating that TNO could be a good candidate for next-generation TCO.

Polycrystalline films on glass substrate

From a practical viewpoint, TCO films need to be coated on glass and plastics. In particular, considerable efforts have been devoted to the deposition of TCO films on glass because of increasing technological demands for flat panel displays and solar cells. Very recently, we have attempted to grow TNO films on glass by using PLD, and obtained $\rho = 4.6 \times 10^{-3} \Omega\text{cm}$ (Fig. 5(a), (b)),¹⁶ which satisfies the practical requirement for TCOs of $\rho \sim 10^{-4} \Omega\text{cm}$. These films were prepared on glass via crystallizing from amorphous phase, and the crystallization process was found to cause a substantial ρ drop by a factor of 10^6 . Further, we applied this technique to sputtering and prepared highly conducting TNO films on glass. Our best film shows $8 \times 10^{-4} \Omega\text{cm}$ at room temperature with absorption less than 10 % in visible.

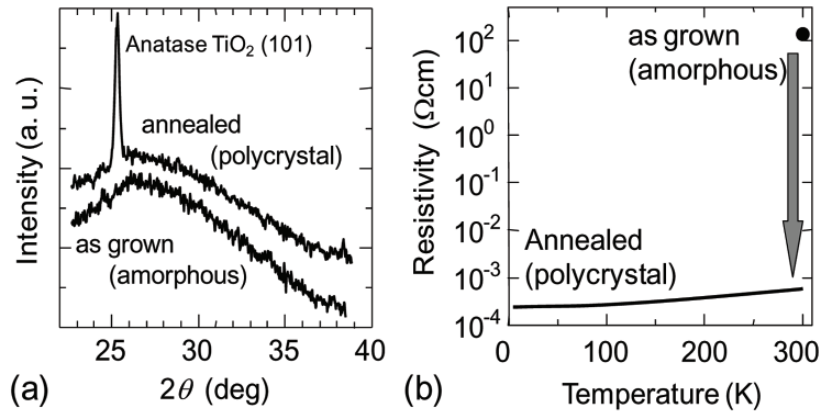


Figure 5 (a) X-ray diffraction patterns of the $\text{Ti}_{0.94}\text{Nb}_{0.06}\text{O}_2$ film before (as-grown, amorphous) and after H_2 annealing at 500°C . Amorphous film crystallizes on annealing. (b) Resistivity of as-grown amorphous film and annealed film. The annealed film shows positive temperature coefficient indicative of metallic behavior.

Preparation method is as follows. Amorphous $\text{Ti}_{0.94}\text{Nb}_{0.06}\text{O}_2$ films were deposited using a commercial sputtering apparatus on unheated non-alkali glass (Corning 1737) substrates (Fig. 6(a)). A sintered pellet with a nominal composition of $\text{Ti}_{0.94}\text{Nb}_{0.06}\text{O}_2$ or Ti metal was used as a sputtering target, and deposition time was adjusted so as to obtain films with thicknesses of ~ 200 nm. The as-grown films were further annealed in vacuum using a rapid thermal annealing furnace, wherein the annealing temperature was raised to 500°C within 5 minutes (Fig. 6(b)). The annealing furnace was evacuated to 10^{-4} Torr, in order to eliminate residual oxygen in the furnace.

Appearance of the films is shown in Figs 6(c) and (d).

The minimum ρ achieved in from this process using sputtering is $8 \times 10^{-4} \Omega\text{cm}$, which is very low ρ as transition metal oxide in polycrystalline form.¹⁷ Notably, annealing treatment in air provides insulating films with $\rho > 10^6 \Omega\text{cm}$, suggesting that oxygen vacancies play an important role for lowering ρ of the polycrystalline TNO films.

A typical film shows a metallic temperature dependence of ρ . Further, n_e is almost

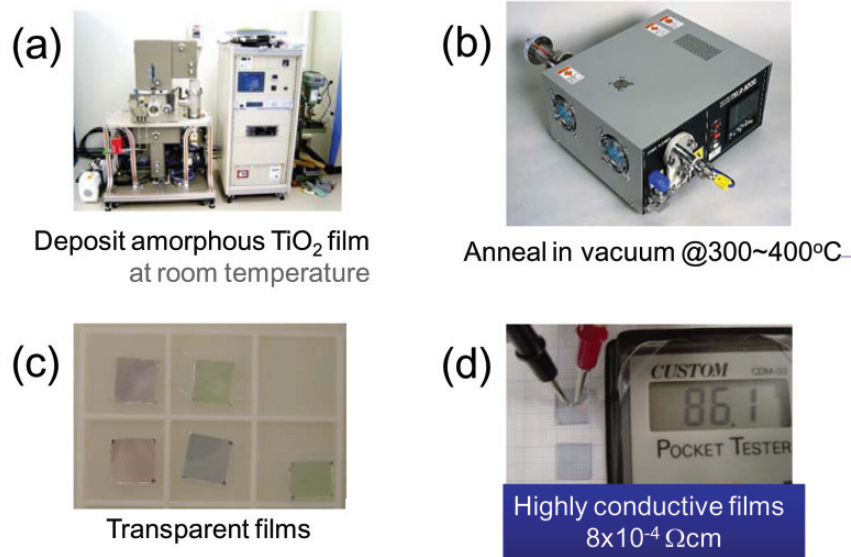


Fig. 6 Preparation process of TiO_2 -based TCO on glass substrate. (a) At first, deposit amorphous TiO_2 film at room temperature by sputtering technique. (b) Then, anneal the film in vacuum at 300 – 600°C. (c) Photograph of films on glass. Films are colored due to interference effect. (d) Demonstration of measurement of TiO_2 -based TCO film.

independent of temperature, so that the present polycrystalline film can be regarded as a degenerate semiconductor. From the n_e value of $\sim 1.6 \times 10^{21} \text{ cm}^{-3}$, it is estimated that doped Nb atoms are activated with an efficiency of $\sim 90\%$. This strongly suggests that the Nb dopants are substituted for the Ti sites in anatase TiO_2 without segregation. High activation efficiency is a unique characteristic of TNO in both epitaxial and polycrystalline films, compared with other conventional TCOs, typically $< 50\%$.^{18,19,20}

Transmittance (T_r) and reflectance (R) spectra of a TNO film after annealing (thickness $\sim 200 \text{ nm}$) are shown in Fig. 7(a). The T_r value throughout the wavelength region of 400-1500 nm is 60-80%, which is lower than those of typical ITO films. This is due to the relatively high refractive index of anatase TNO, approximately 2.4 at 500 nm, which tends to enhance R and, thus to suppress T_r . The absorbance (A) in the visible region, evaluated from the formula $A = 1 - (T_r + R)$, is below 10% (Fig. 7(b)).

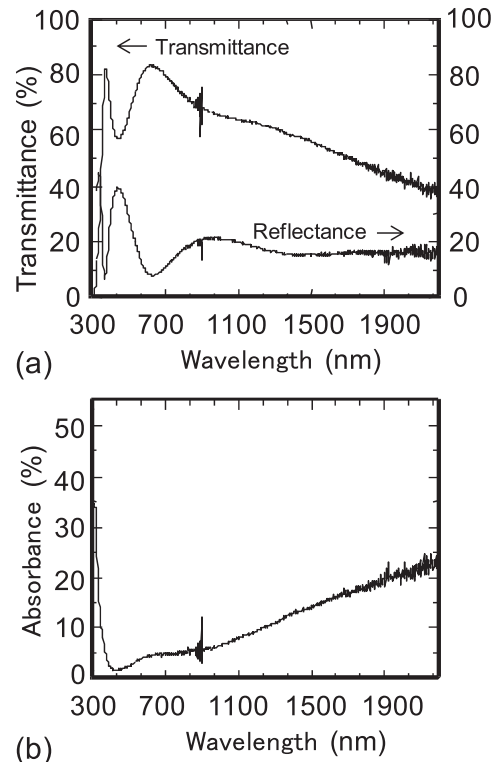


Fig. 7 (a) Transmittance, reflectance, and (b) absorbance, of a typical anatase $\text{Ti}_{1-x}\text{Nb}_x\text{O}_2$ on glass substrate.

H																	He	
Li	Be											B	C	N	O	F	Ne	
Na	Mg											Al	Si	P	S	Cl	Ar	
K	Ca	Sc	Ti	V	Cr	Mn	Fe	Cd	Ni	Cu	Zn	Ga	Ge	As	Se	Br	Kr	
Rb	Sr	Y	Zr	Nb	Mo	Tc	Ru	Rh	Pd	Ag	Cd	In	Sn	Sb	Te	I	Xe	
Cs	Ba	La	Hf	Ta	W	Re	Os	Ir	Pt	Au	Hg	Tl	Pb	Bi	Po	At	Rn	
Fr	Ra	Ac																

d-electron system
s-electron system

Fig. 8 Anatase $Ti_{1-x}Nb_xO_2$ is a *d*-electron-based new TCO.

Prospects toward application

It is very important to find applications that utilize the unique characteristics of TiO_2 -based TCO. As mentioned earlier, this TNO has several properties that ITO does not have, such as, high refractive index, high transmittance in infrared, and high stability in reduced atmosphere. These properties would provide new opto-electrical devices that would not compete with ITO. We are now seeking applications for light emitting diodes and solar cells to increase their efficiency. Further, since this TNO system is based on *d*-electron system (Fig. 8), combining TCO properties with *d*-electrons may open up new spinelectronic devices or new perspectives utilizing *d*-electrons.

Lower ρ and higher transmittance is still required, and experiments are underway. By introducing seed layer, we have obtained $6.5 \times 10^{-4} \Omega\text{cm}$ on glass substrate by using sputtering method. Exploration of other dopant and to establish guiding principles to obtain a new TCO should be very important research topics.

CONCLUSIONS

We reported on the development of anatase TiO_2 -based transparent conducting oxide. The epitaxial film exhibits low $\rho \sim 2 \times 10^{-4} \Omega\text{cm}$ and high optical transmittance in visible. We have also succeeded in preparation of highly conducting anatase $Ti_{0.94}Nb_{0.06}O_2$ polycrystalline films on glass substrates by sputtering technique. The polycrystalline films was revealed to show excellent transparency with absorption $<10\%$ in visible region. These results are encouraging for the fabrication of wide-area polycrystalline TNO on glass with practical electrical and optical properties as a TCO. We conclude that anatase Nb-doped TiO_2 is a promising candidate for ITO alternatives. This material is the first transparent conducting oxide based on *d*-electrons, and the present results would stimulate material explorations to search for new TCOs based on *d*-electrons.

Acknowledgments

I would like to express my sincere thanks to my collaborators, Prof. Tetsuya Hasegawa (Univ. of Tokyo), Prof. Yutaka Furubayashi (Kanazawa Inst. of Tech.), and Dr. Naoomi Yamada (Kanagawa Academy of Science and Technology). This work was supported by MEXT Elements Science and Technology Project, the Global COE Program for Chemistry Innovation, and NEDO.

- 1) D. S. Ginley and C. Bright, *Mater. Res. Bull.* **25**, 15 (2000).
- 2) H. L. Hartnagel, A. L. Dawar, A. K. Jain, and C. Jagadish: *Semiconducting Transparent Thin Films*; Institute of Physics: Bristol, UK, 1995.
- 3) C. A. Pan and T. P. Ma, *Appl. Phys. Lett.* **37**, 163 (1980).
- 4) I. Hamberg and C. G. Granqvist, *J. Appl. Phys.* **60**, R123 (1986).
- 5) T. Minami, *Mater. Res. Bull.* **25**, 38 (2000).
- 6) Y. Furubayashi, T. Hitosugi, Y. Yamamoto, K. Inaba, G. Kinoda, Y. Hirose, T. Shimada, and T. Hasegawa, *Appl. Phys. Lett.* **86**, 252101 (2005).
- 7) T. Hitosugi, Y. Furubayashi, A. Ueda, K. Itabashi, K. Inaba, Y. Hirose, G. Kinoda, Y. Yamamoto, T. Shimada, and T. Hasegawa, *Jpn. J. Appl. Phys.* **44**, L1063 (2005).
- 8) H. Tang, H. Berger, P. E. Schmid, F. Levy, and G. Burri, *Solid State Commun.* **23**, 161 (1977).
- 9) H. Tang, K. Prasad, R. Sanjines, P. E. Schmid, and F. Lévy, *J. Appl. Phys.* **75**, 2042 (1994).
- 10) S. R. Taylor, and S. H. McLennan, *The Continental Crust: Its Composition and Evolution*, Blackwell, Oxford, p.312 (1985).
- 11) A. I. Kingon, J.-P. Maria, S. K. Streiffer, *Nature* **406**, 1032 (2000).
- 12) M. Fujimoto, H. Koyama, M. Konagai, Y. Hosoi, K. Ishihara, S. Ohnishi, and N. Awaya, *Appl. Phys. Lett.* **89**, 223509 (2006).
- 13) Y. Matsumoto, M. Murakami, T. Shono, T. Hasegawa, T. Fukumura, M. Kawasaki, P. Ahmet, T. Chikyow, S. Koshihara, and H. Koinuma, *Science* **291**, 534 (2001).
- 14) H. Berger, H. Tang, and F. Lévy, *J. Cryst. Growth* **130**, 108 (1993).
- 15) Y. Shigesato, D. C. Paine, and T. E. Haynes, *J. Appl. Phys.* **73**, 3805 (1993).
- 16) T. Hitosugi, A. Ueda, S. Nakao, Y. Furubayashi, N. Yamada, Y. Hirose, T. Shimada, and T. Hasegawa, *Appl. Phys. Lett.* **90**, 212106 (2007).
- 17) N. Tsuda, K. Nasu, A. Fujimori, K. Shiratori, *Electronic Conduction in Oxides*, Springer, Berlin, 2000.
- 18) N. Yamada, I. Yasui, Y. Shigesato, H. Li, Y. Ujihira, and K. Nomura, *Jpn. J. Appl. Phys.* **39**, 4158 (2000).
- 19) H. Kostlin, R. Jost, and W. Lems, *Phys. Stat. Sol(a)* **29**, 87 (1975).
- 20) J. -C. Manificier, L. Szepessy, J. F. Bresse, M. Perotin, R. Stuck, *Mat. Res. Bull.* **14**, 163 (1079).



Dr. Rudolf M. TROMP

主任研究者 トロンプ・ルドルフ

LOW ENERGY ELECTRON MICROSCOPY: A 10 YEAR OUTLOOK

Rudolf M. Tromp

IBM T.J. Watson Research Center
1101 Kitchawan Road
P.O. Box 218
Yorktown Heights, NY 10598
USA

SUMMARY

Low Energy Electron Microscopy (LEEM), and its close cousin Photo Electron Emission Microscopy (PEEM) have evolved from curiosities in the hands of physicists, to powerful tools for dynamic materials analysis. Invented in 1962, and first successfully realized in 1985, there are about 30 combined LEEM/PEEM instruments in the world today, in addition to about an equal number of PEEM-only instruments. Most of these instruments follow a design that is now almost 20 years old. The most advanced instruments are located at synchrotron radiation facilities, but they are relatively few in number, and not readily available to the general user. In the meantime, the field of electron microscopy is undergoing revolutionary advances fueled by dual breakthroughs in electron energy filtering and aberration correction. Similarly, the field of quantum optics is developing ever more powerful light sources in the Vacuum Ultra Violet (VUV) and soft X-ray ranges that do not depend on massive investments in national infrastructure (i.e. synchrotrons), but deliver their photons in a standard laboratory. These advances from two very different fields will combine to set the stage for the development of LEEM and PEEM over the next decade. Aberration correction will improve LEEM resolution from 5-10 nm today, to 1.5-2 nm in the near future, enough to resolve individual unit cells in the famous Si(111)-(7x7) surface, or –probably more important- sufficient to resolve the structure of nanoscale features such as magnetic domain walls. In PEEM the spatial resolution will improve from ~ 20 nm today to 4-5 nm, while at the same time improving transmission by a factor ~10. Energy filtering, today mostly used by synchrotron-based instruments, will be ubiquitous, powerful, simple, and relatively inexpensive. For PEEM there will be a broad choice of light

sources, not just the ever-present Hg discharge lamp of today. We will obtain not just the atomic structure of surfaces using LEED-IV information with nm spatial resolution, nor just the spatial arrangement of structural domains, quantum well structures, or other multi-phase arrangements, as well as their evolution in time; but we will also learn the spatially resolved electronic structure from nano-ARUPS, Angle Resolved Ultraviolet Photoelectron Spectroscopy at the nanoscale, as well as the chemical makeup of the surface with nano-XPS, X-ray Photoelectron Spectroscopy at the nanoscale, all in one compact instrument, in a standard laboratory environment. Some of the ingredients of this new paradigm are in place today, others need more work. This paper will give an overview of where we are, and where we need more work and more investment.

A LITTLE BIT OF HISTORY

LEEM and PEEM, while having reached adolescence only recently (not always well-behaved, and with pimples here and there), are not exactly new kids on the block. Ernst Bauer¹ invented LEEM in 1962 . But cathode-lens microscopy goes back to the early days of electron microscopy, to Bruche² , and other pioneers of the field. For many decades electron microscopy was thrust forward by a single-minded imperative: resolution. As Oliver Wells often reminds me, the Scanning Electron Microscope could have been built much earlier. But who was interested in a microscope that promised only 20 nm spatial resolution? In the 80's and 90's we witnessed the emergence of MeV electron microscopes that required the construction of multistory buildings to house them, trying to beat chromatic and geometric lens aberrations by sheer force. But faster, more powerful computers caught up with them. First, computer-based reconstructions of aberration-corrected images³ pushed resolution down below 0.1 nm. This was followed by computer-designed and -controlled electron-optical multipole aberration correctors that deliver 70 pm spatial resolution in a microscope that fits inside a regular lab again⁴ . In transmission electron microscopy, aberration correction is a commercial reality. The race for resolution will now be replaced by a race for usability and function. In LEEM and PEEM the driving force has never been resolution. The best non-corrected resolution measured with LEEM is 4.1 nm, at 3.5 eV electron energy⁵ , not even close to 70 pm. But LEEM naturally has an exquisite surface sensitivity that TEM does not offer. It can follow the evolution of surface structure in real time with an ease and grace that neither TEM, nor SEM, nor STM can match. LEEM cannot see atoms, but it can see what atoms do, how they make atomic steps fluctuate at high temperature, how and where nucleation occurs during growth, how critical fluctuations mark two-dimensional phase transitions. With PEEM we can look at core levels for chemical information, use magnetic dichroism to study magnetic structure and dynamics with sub-nanosecond time resolution, probe valence band information for electronic structure. So, while function has been the first and foremost driving force in LEEM and PEEM, resolution has taken a backseat. Even so, a few experiments have shown that aberration correction, based not on

multipoles but on electron reflection mirrors, can work in LEEM/PEEM, and developments of commercial versions are well under way.

On the photon end of the spectrum, many of us will recall the Teller X-ray laser. While potentially powerful, it never had much appeal for scientists who aspired to having a reliable laser source in their own lab. How often do you get a chance to trigger the explosion of an atomic bomb? Fortunately, we have also witnessed the renaissance of atomic physics. Thirty years ago, this field seemed of interest only to scientists with an innate fondness of bookkeeping. Long, inscrutable tables of spectral lines, labeled with orbital transition indices failed to inspire most of us. Now, atomic fountains, laser cooling, Bose-Einstein condensation, atoms in strong fields, and Nobel Prizes too, sing a siren song that casts a powerful spell. Soft X-ray lasers now exist⁶ and you don't have to work for the government to own one. VUV lasers are rapidly improving^{7, 8}. In the next ten years these light sources will become more mature, and will become a formidable competition for synchrotron radiation light sources. High brightness, easily controlled polarization, tunability, low cost, year-round availability to the individual researcher, photons@home. These are some of the attributes that will drive the development of these sources, as well as compelling commercial applications such as the several kW average power 13.5 nm laser-based light sources needed for VUV lithography⁹, supported by powerful international semiconductor consortia.

Thus, out of these two seemingly unconnected research strands, low-resolution electron microscopy with cathode lenses, and atomic physics, have emerged two exciting opportunities that will merge over the next 5-10 years, and create a new form of microscopy that will probe atomic, geometric, electronic, chemical, and magnetic structure, on one sample, in one instrument, in real time, with nanometer spatial resolution, and with (sub)nanosecond time resolution. Aberration corrected, energy filtered LEEM/PEEM plus photons@home will bring these powerful capabilities to small scale research labs, at a cost that will be affordable to numerous institutions.

WHAT IS LEEM?

As the name suggests, LEEM uses low energy electrons to form an image of a sample. Compared to any other form of electron microscopy, really low energy electrons, in the range of 0-100 eV, but most often below 10 eV. At these very low electron energies, the elastic reflectivity of the incident electron beam is very high, guaranteeing bright images that can be obtained at video-rate (or faster) acquisition times. So LEEM can make real-time movies of surface processes such as growth, phase transitions, step motion, etching, etc. Since the electrons are slow and reflect from the surface, LEEM is also very surface sensitive, with probe depths ranging from sub-nm to several 10s of nm. The electron energy can be kept almost arbitrarily low, even down to zero eV if we make the electron turn around just a few nanometers in front of the sample in so-called mirror microscopy.

This makes LEEM extremely suitable for the study of highly radiation sensitive materials such as thin film organics and self-assembled monolayers, which can be observed without degradation under the electron beam¹⁰.

To get the electrons onto the sample, we start with an gun that generates electrons with 15 keV kinetic energy (figure 1)¹¹. A rather standard condenser lens system transports the beam down the optical column towards the objective lens. However, before reaching the objective lens, the electrons pass through a double-focusing magnetic 90° deflection system whose purpose will soon become clear. The electrons are then refocused by a transfer lens into the backfocal plane of the objective lens, so that a collimated beam is directed at the sample. While the objective lens is grounded, the sample is held at a potential close to the electron gun potential. Thus the electrons are decelerated between the objective lens and the sample to an adjustable energy in the range of 0-100 eV, and they interact with the sample at this low electron energy. At such low energies, the electron wavelength is on the same order of magnitude as the atomic spacing in the surface. If the sample is crystalline, the reflected electrons will undergo Low Energy Electron Diffraction (LEED), and after reflection from the sample, and after re-acceleration to 15 keV, a LEED pattern will be observed in the backfocal plane of the objective lens. The objective lens also forms a real-space image of the sample at a greater distance. The transfer lens then focuses the image onto the diagonal plane of the magnetic 90° deflection system, which directs the beam down into the projector column. As we see, the incident and reflected paths of the electron beam between the 90° deflection system and the objective lens coincide. The purpose of the 90° deflection system is to spatially separate the illumination and projection systems of the electron microscopes so that we have independent control over these essential functions. We will see later that the 90° deflection system can also serve as a high quality, and very convenient energy filter that allows us to record energy filtered images and angular intensity distributions, as well spatially resolved energy spectra. But for now we will ignore this feature.

The LEED pattern is again in focus in the center of the first lens below the 90° deflection system, where we can insert a contrast aperture to select the LEED beam that we want to use for image formation, enabling bright field and dark field imaging conditions, as in a TEM. The remaining lenses then project either the real space image, or the diffraction pattern onto the channelplate intensified phosphor screen.

This arrangement allows us a variety of imaging modes. In bright field imaging the (0,0) specular LEED beam is selected (figure 2a). In this case all areas on the surface will diffract into the aperture (assuming that all areas of the surface are crystalline), and contrast can arise in a variety of ways. First, areas with different structures will have different structure factors, and thereby different (0,0) beam intensities, at least at some electron energies. Second, contrast can arise at

atomic steps when the path length difference between electrons reflected from the top and bottom of an atomic step is a non-integer fraction of the electron wavelength. By slight defocusing of the objective lens Fresnel fringes will mark the locations of the atomic steps on the surface. Third, thin films present on the surface may have a thickness that locally matches the wavelength of the incident electron beam, giving rise to so-called quantum well contrast. Dark field imaging uses a LEED beam other than (0,0) (figure 2b). For instance, on the dimmer-reconstructed Si(001)(2x1) we may select a (1/2,0) diffracted beam. As the dimmer reconstruction rotates by 90 degrees at each atomic step, every other atomic terrace will diffract into this (1/2,0) beam, while intervening terraces diffract into the (0,1/2) beam. Therefore, alternating terraces will have bright and dark contrast. Finally, in mirror imaging the sample bias is more negative than the gun potential, so that the electrons never touch the sample but turn around just in front of it (figure 2c). The mirror image is very sensitive to geometric features on the sample, as well as spatial variations in electrostatic potential (such as workfunction variations), and even to magnetic fringe field emerging from a magnetic sample which easily deflect the electrons at the turning point where their kinetic energy is momentarily reduced to zero. Finally, figure 2d shows a representative LEED pattern obtained on the Si(111)(7x7) surface, obtained with the contrast aperture removed from the beam path.

As mentioned before, the electron reflectivity of the electrons at these low energies can be very high (in mirror mode the reflectivity equals unity), and bright, high contrast images are easily obtained at video acquisition rates, enabling dynamic imaging of surface process such as epitaxial growth, interface formation, phase transitions, etcetera. Several reviews are available in the literature that provide a broad background on the types of experiments that are possible¹²⁻¹⁵.

One feature we would like to highlight here, is that the bright-field image intensity depends strongly on the electron energy. Of course, the analysis of the LEED spot intensity as a function of electron energy (known as LEED-IV intensity analysis) is the oldest structural technique in surface science^{16,17}. Calculations of the intensity of the diffracted LEED beams with energy are not trivial. Of course, the intensities depend on the structure of the surface. However, unlike electron scattering at much higher energies, and unlike X-ray diffraction, multiple scattering events are extremely important and must be taken into account in detail. Over the last 30 years such calculations have been used to determine hundreds if not thousands of surface structures¹⁷. The bright field LEEM image shows us the spatial distribution of the intensity of the (0,0) LEED beam. If we now vary the sample potential, and thereby the electron energy, we can measure the spatially resolved LEED-IV information for each pixel in the image, with a spatial resolution that is limited by the resolution of the microscope, between 5 and 10 nm. In a recent paper J. Hannon and coworkers¹⁸ have shown how this information can be used to determine the atomic structure and composition of the Cu(001)-Pd system with high accuracy, distinguishing and measuring the amount of Pd in the outer three atomic layers of the crystal with 10 nm lateral resolution (figure 3). This highlights an important

strength of LEEM: while the spatial resolution is not sufficient to see individual atoms, we can still obtain atomic resolution structure data by making use of the quantitative information contained in the diffraction pattern. As the images in figure 2 and 3 show, we also obtain structural information on larger scales, such as the locations and shapes of atomic steps, spatial distributions of phase domains, etcetera.

AND WHAT IS PEEM?

In PEEM we illuminate the sample not with an electron beam, but with photons which –by the photoelectric effect- emit electrons from the sample. The most universally used light source is a Hg discharge lamp which emits photons with an upper energy of about 4.8 eV. If the workfunction of the sample (energy separation between the Fermi level of the solid and the vacuum level) is smaller than the photon energy, then photoexcited electrons can leave the sample into the vacuum. They are then accelerated into the objective lens, and used to form an image of the sample. This image is very sensitive to local variations in the workfunction. If the sample is not perfectly flat, the equipotential planes in front of the sample are distorted by the geometric features of the sample, giving rise to localized focusing or defocusing effects. Thus, the image is also very sensitive to sample geometry, which is sometimes a blessing, sometimes a detriment.

Things get more interesting when the photon energy becomes higher. In the early days of Angle-Resolved Ultraviolet Photoelectron Spectroscopy (ARUPS), the He discharge lamp was the light source of choice. It delivers an intense beam of UV light at a photon energy of 21.2 eV (HeI line), or a weaker beam at 40.8 eV (HeII line). This light source is compact, simple to operate, highly monochromatic, and relatively inexpensive. Other photon energies are available by switching to different gases such as Ne or H. At these higher photon energies, electrons are excited from a larger range of binding energies inside the valence band. For instance, on semiconductor surfaces we can see the bulk valence bands, as well as electron states localized at the outermost atomic layer – surface states. By measuring the electron energy distributions as a function of emission angle, the energy versus momentum distributions of the electrons can be measured, and the bandstructure of the sample reconstructed and compared with theory. There is no doubt that ARUPS has contributed more to our understanding of the electronic structure of materials than any other method¹⁹. Presently, high resolution ARUPS plays a key role in building an understanding of the fundamental science behind such materials as high temperature superconductors, and graphene.

At higher photon energies yet, electron emission from the deeper core levels becomes possible. These core levels are to first order a marker of the chemical identity of the atom which emits the electron. But the detailed finestructure of the core level spectrum contains information not only on the chemical identity of the atom, but also on its chemical environment, as the exact

binding energy depends sensitively on that environment. The angular emission pattern is affected by the location of the atom's neighbors, and this atomic geometry can be reconstructed from the photoelectron diffraction pattern. Magnetic information is available by means of circular and linear magnetic dichroism effects, enabling dynamic imaging of magnetic domain structure with time resolutions below 1 nanosecond²⁰. Thus, the use of corelevel information in PEEM adds a powerful set of analytical tools to the experiment.

Unfortunately, this expansive power of PEEM imaging methods is today available only at the few instruments coupled to synchrotron radiation sources. Of course, synchrotrons are in many ways the ideal photon sources for such experiments, with high brightness, adjustable polarization, and broad energy tunability. Synchrotrons are also expensive, and not easily accessible to the general user, with only small chunks of beamtime in any given year, and little opportunity to systematically explore a given materials system over longer time. Also, it is hard to get access for routine (but tremendously important) routine sample analysis for things such as metrology inspection, quality control, contamination analysis, etcetera. The promise of PEEM is therefore only a distant vision for many potential applications, difficult if not impossible to turn into reality.

ENERGY FILTERING

There are yet other technical hurdles. To take advantage of the full power of PEEM it is desirable to analyze the photoelectrons in both energy and emission angle. This is absolutely necessary if we want to obtain information on the electronic bandstructure of our sample. Even many PEEM experiments performed at synchrotron rings don't use an energy filter^{21,22}. The elemental sensitivity is obtained by scanning the photon energy across a corelevel excitation threshold, and the contrast aperture serves to crudely select electrons over a bandwidth of several eVs in the secondary electron band near zero kinetic energy. There is an important reason for doing this: it simplifies the setup (no energy filter), the transmission is high, and it is easier to scan the photon energy than to analyze the electron energy. Many elegant experiments have been performed in this manner, but it also leaves many possibilities on the table. An energy filter is a rather tricky piece of electron optics, and energy filtering in transmission electron microscopes has only come to maturity over the last 10-15 years, with significant advances still being made^{23,24}. In PEEM, the main approach explored so far is to install a hemispherical electrostatic analyzer, well known from lab-based XPS experiments, in the projector column of the PEEM instrument²⁵. The electrons are deflected by a 180° spherical capacitor which exhibits a chromatic dispersion (displacement per unit of energy) given by $D=2R/E$, where R is the mean radius of the spherical capacitor, and E the energy with which the electrons pass through the analyzer. To increase the energy dispersion (and thereby the energy resolution for a given slit size), one can make R larger, i.e. increase the physical

size of the analyzer. This is expensive, and heavy, because the volume and mass of the analyzer increase with R^3 , while the dispersion increases only with R . Alternatively, one can decrease the pass energy E by decelerating the electrons before they enter the analyzer to energies of a few 100 eV or less, far lower than the transport energy of the electron beam in the rest of the microscope. In practice, both strategies are followed, often at the same time, so that the highest resolution electron spectrometers combine large size with low pass energy. In an electron microscope, one must also carefully control the optical properties of the analyzer, in reference to both the diffraction and the image planes, which are widely separated in space. That is, the energy filter must produce stigmatic images of both the image and the diffraction planes, preferably at unit magnification, without compromising image quality. This requirement necessitates the addition of coupling lenses, as well as retardation/acceleration lenses, resulting in a complex and expensive setup. Furthermore, once the energy filter is in place, its use can no longer be avoided. The electron beam must always pass through the analyzer and all its associated optics, further complicating alignment and use of the microscope, even when the energy filtering function is not required for a certain experiment.

This is where we take advantage of a hitherto overseen or even avoided fundamental property of the magnetic 90° deflection system, namely its chromatic dispersion. On their path through the 90° deflection system, electrons with higher energy will be deflected over a smaller angle than electrons with a lower energy, unless specific optical design measures are taken to avoid such dispersion²⁹. In the simple 90° deflection system described here dispersion is present, and the following discussion will apply to this specific design. If the mean radius of the deflector is given by R , and the distance from the diffraction planes (situated symmetrically about the deflection field) to the edge of the deflection field by L , then the dispersion is given²⁶ by $D=(R+L)/2E$. In the case that R and L are of similar magnitude, we see that this dispersion is about half as large as that of a hemispherical capacitor. Since the deflection angle is also half as large (90° instead of 180°), this makes sense. Of course, dispersion occurs only in the plane of deflection, and not orthogonal to it. So, a diffraction plane located in the diffraction entrance plane of the 90° deflection system on the objective lens side is both imaged (1:1), and dispersed in the diffraction exit plane of the 90° deflection system. Importantly, the image plane located on the diagonal of the 90° deflection system is achromatic, not affected by dispersion. This is a consequence of the symmetric location of this specific plane. If we now place a slit in the diffraction entrance plane, oriented normal to the deflection plane, we will see a dispersed image of this slit in the diffraction exit plane: energy versus momentum along one of the two primary momentum directions, $E-k_y$, as schematically shown in figure 4.

The vertical position of the slit in the diffraction entrance plane determines the value of k_x . This image can be projected directly on the channelplate intensified phosphor screen and recorded with a suitable camera. By placing a contrast/energy selection aperture in this $E-k_y$ plane, we

can select an energy window of interest and record an energy-filtered real space image for that choice of $E(k_x, k_y)$. By scanning the sample voltage, the energy window is conveniently scanned across the energy spectrum, and we can record real space images for different energies across the energy spectrum. Sometimes one is interested not only in energy filtered images, but also in energy filtered angular distributions, i.e. not just $E-k_y$, but $E-\mathbf{k}$, the full 3-dimensional binding energy vs wavevector distribution. This can be conveniently obtained by scanning the entrance slit across the diffraction plane, in the k_x direction. By recording an $E-k_y$ distribution for each k_x , the full $E-\mathbf{k}$ distribution is easily reconstructed²⁷.

A few questions still need to be addressed. First, the magnetic deflection field is rather small in size, with $R=68$ mm and $L=116$ mm for our microscope, and the electrons are not decelerated on their path through the 90° deflection system. Can we still get sufficient energy resolution? At 15 keV these numbers translate in a dispersion of about 6 m/eV. Using an energy filter slit with a width of 1 μm , fabricated by a Focused Ion Beam milling system, we measure an energy resolution of 0.15 – 0.2 eV, in good agreement with this prediction. Thus, even without slowing the electrons down we obtain an energy resolution $E/\Delta E$ of 100,000, similar to spherical capacitor analyzers at a pass energy of a few 100 eV. For energy-filtered imaging we use a larger slit with a width of 10 μm , giving a passband of 1.5 eV, well matched to the natural line width of typical spectroscopic features and thus optimizing instrument transmission in imaging applications.

Second, how hard is it to operate this energy filter? This is one of the really nice features. The 90° deflection system is an essential and integral part of the LEEM instrument, with or without additional energy filter. Thus, utilizing it as an energy filter only requires the installation of a scanning slit in the entrance side diffraction plane, but *no additional optics*. The electrons are not decelerated, but pass through the 90° deflection system at full 15 keV energy, eliminating the need for retardation and acceleration optics. Already in unfiltered LEEM/PEEM operation the electrons pass through the 90° deflection system, and aligning it is a routine and simple part of microscope setup. In order to make use of the energy filtering function, all that is required is to insert the energy filter slit in the entrance side diffraction plane. No other alignment or changes to the instrument operational parameters are needed to use the energy filtering function.

Finally, is it possible to reconstruct the full $E-\mathbf{k}$ distribution simply by scanning the entrance slit? Indeed it is²⁷. Figure 5 shows illustrative results obtained on a composite Ag(111)/Ag(001) island grown inside the LEEM on a Si(111) substrate. The sample was illuminated with a focused HeI light source, running at a power of about 270 W. Imaging the sample with secondary electrons, the Ag(111) area shows up in bright contrast, while the (001) area is dark (figure 5a). The crystal orientations of each area were determined by selected-area LEED in the LEEM instrument. Using a selected-area aperture in the image plane on the diagonal of the 90° deflection system, we can obtain $E-k_y$ spectra from either the (111) or (001) areas of the Ag crystallite. Placing the energy slit

across the center of the Ewald sphere, the Ag d-bands are clearly observed on both areas, but their dispersions are quite different. By scanning the slit along the k_x direction, the full E- \mathbf{k} distribution can be obtained. Energy spectra at selected k_x, k_y points are shown in figures 5c and 5d for both (111) and (001) areas. We can then extract the full k_x, k_y intensity distribution at a fixed binding energy. Such distributions are shown at a binding energy of 6.1 eV, for both (111) and (001) areas in figures 5e and 5f, reflecting the 3-fold and 4-fold symmetries of both areas. Both surfaces shows a strong photoemission resonance at the boundary of the surface Brillouin zone, corresponding to the bulk L-point where resonant photoemission can occur from an occupied d-band to a high-lying unoccupied band with an interband separation of 21.2 eV, just equal to the incident photon energy. This is the first time that this photoemission resonance has been observed on Ag in an off-normal direction. Acquisition time of the data sets shown in figure 5 was about 1 hour. Finally, figure 5b shows an energy filtered image with the filter aperture selecting the Ag d-band. The contrast difference between (111) and (001) has now disappeared, as both (111) and (001) areas feature prominent d-band intensity. It turns out that the contrast seen in figure 5a is not related to a difference in workfunction between (111) and (001) areas (as usually assumed in such PEEM images), but to a final state effect on the (001) surface where no final state bands are available just above the vacuum level, and photoemission at those energies is therefore strongly reduced relative to (111).

ABERRATION CORRECTION

To further improve the performance of the LEEM/PEEM instrument it is highly desirable to reduce or eliminate the chromatic and spherical aberrations of the objective lens. While aberration coefficients of TEM instruments are measured in millimeters, the corresponding numbers for a cathode lens are measured in meters. In other words, these are really rather poor lenses. This is not the result of inadequate design. The first image forming element in the microscope is the strong accelerating field between the sample and objective lens, which forms a virtual image at magnification $2/3$ behind the sample. It is this unavoidable image forming electrostatic field that dominates the microscope aberrations. To first order, the image resolution scales with $1/E_g$, where E_g is the strength of the electrostatic field in the gap between sample and objective lens. Thus, to optimize resolution it is advantageous to work at the largest field strength practical, in the range of 100 keV/cm, close to the electrostatic discharge limit. It was first shown by Rempfer and coworkers²⁸, and further demonstrated in the SMART project by Rose and coworkers²⁹, that the chromatic and spherical aberrations of the cathode objective lens can be corrected with a 4-element electrostatic electron mirror. This mirror, containing 1 grounded lens element, and 3 negatively biased lens elements has three degrees of freedom, i.e. the three bias voltages. There are also three parameters that need to be controlled: the mirror focal length f_m , the chromatic aberration

coefficient C_c , and the spherical aberration coefficient C_s . It is a generous gift of nature that the three independently controllable voltages are sufficient to adjust all three parameters, f_m , C_c and C_s , so that the mirror creates a properly focused image of the sample, while at the same time canceling the chromatic and spherical aberrations of the objective lens. It even turns out that the mirror reduces the leading 5th order geometric aberration term by a factor 5-10, and the final resolution is limited by a combination of diffraction, 2nd order chromatic, and 5th order geometric aberrations. The effects of aberration correction are demonstrated in figure 6 which shows how improvement in LEEM resolution by a factor 3 is accompanied by an increase in transmission by a factor 9. Similar numbers hold for PEEM experiments with energy pass bands of 1.5 – 3 eV. We predict that LEEM resolution will be better than 1.5 nm, while PEEM resolution will be about 4 nm.

At present, the best resolution recorded with a non-corrected LEEM is 4.1 nm, while the aberration-corrected SMART machine has obtained a resolution of ~3 nm. There is still room for improving resolution by another factor 2. We have completed the design of a new, compact aberration-corrected and energy-filtered LEEM/PEEM instrument, and this new instrument is under construction at the time of writing of this manuscript. It is projected to be operational by the end of 2008.

LIGHT SOURCES

The results in the previous chapter were obtained with a conventional HeI discharge lamp, equipped with a focusing capillary to improve brightness. What other lab-based light sources are presently available? First, in addition to the HeI line, we have also used the HeII line at 40.8 eV with good results, for instance to map the bandstructure of 1.5 monolayers of graphene grown on SiC(0001). In addition, we have a very bright pulsed laser (80 MHz, 12 ps pulse width) in which 355 nm laser light (SpectraPhysics Vanguard laser system) is doubled by a non-linear KBBF crystal (grown at the Institute for Crystal Growth and Development of the Chinese Academy of Sciences in Beijing⁷) to 177 nm. This light is fully coherent, polarized, and focused onto the sample to a spot size of ~35x100 μm^2 . With a photon energy of 6.994 eV, this laser light accesses the top 2-3 eV of the valence band of most materials, providing a very useful spectral range for a wide variety of materials problems. We also have a compact 266 nm laser source. In the longer term we plan to add light sources at significantly shorter wavelengths, in the energy range of 100-250 eV where many corelevels become accessible. Much higher photon energies are not necessarily advantageous, as the electron kinetic energy for a given corelevel increases linearly with photon energy. As kinetic energy increases, the diameter of the Ewald sphere also increases, while only a small diameter area near the optical axis can be accepted for image formation. The transmission therefore drops off with 1/E where E is the kinetic energy of the core electron after excitation into the vacuum. The standard light source used in XPS experiments, using Al or Mg $K\alpha$ radiation will therefore not

be very useful for energy filtered PEEM imaging and spectroscopy experiments, as the reduced transmission at high electron energies will result in weak signal strengths.. Much more promising are the efforts expended in developing 13.5 nm light sources for EUV lithography⁹. With a photon energy of ~92 eV, a 13.5 nm source would give access to both valence bands and core levels for a fairly broad range of materials. At 200 eV photon energy much of the periodic table would be accessible. Development of such light sources will require effort and investment, but will be well worth the trouble. Already, high harmonic generation in gas-filled capillaries can generate photons up to 250 eV⁶, although the short pulse lengths and low duty cycles are not yet attractive for PEEM applications.

Of course, synchrotron sources will continue to provide excellent tunability and brightness, and a small number of experiments will be able to take advantage of such facilities. But we foresee that the center of gravity for spectroscopic LEEM/PEEM will shift from synchrotron to academic and industrial laboratories, taking advantage of both improved electron optics and improved lab-based VUV, EUV, and soft X-ray light sources. The latter may not provide the same level of flexibility as synchrotron light, but they will be available full time to the individual researcher, in an environment which is

completely under his or her control. When new light sources become available, they can be added to the instrument without major revision of the instrument layout. Figure 7 shows the present configuration of the spectroscopic LEEM/PEEM system at IBM, with HeI/HeII light sources, as well as 262 nm and 177 nm laser sources installed on the system.

CONCLUSIONS

LEEM and PEEM have become powerful tools in the study of surfaces and interfaces. While LEEM primarily gives structural information, PEEM can complement LEEM by providing insight into the electronic, chemical, and magnetic properties of the sample. Powerful energy filtering methods have already enabled the acquisition of energy filtered valence band images, as well as full E-**k** ARUPS data on selected sample areas with a diameter of a few μm , in a standard lab environment using HeI and HeII gas discharge sources²⁷. Combination of energy filtering with electron mirror-based aberration correction will improve resolution in LEEM to below 1.5 nm, and in PEEM to 4-5 nm, while increasing transmission by an order of magnitude. New laser-based VUV, EUV, and soft X-ray light sources are starting to become available, and will become ever more useful over the next 5-10 years. Twenty years ago Scanning Tunneling Microscopy was a physicist's dream toy, with limited practical utility. Today it is hard to imagine nanoscale science without STM and AFM. Similarly, LEEM/PEEM instruments are not widely available today, and

mostly in the hands of physicists pursuing questions in basic science. Over the next decade we will witness a broadening of the LEEM/PEEM user community into materials science, chemistry, micro- and nano-electronics, MEMS and NEMS, spintronics, and even life sciences, driven by the convergence of developments in electron optics and atomic physics/quantum optics briefly reviewed in this paper. We hope that WPI-AIMR will play a central role in, and take extensive advantage of these developments.

Acknowledgements:

I like to thank Dr. Jim Hannon for his many essential and deep contributions to the work presented here, Dr. Y. Fujikawa (IMR, Tohoku University) for his critical role in the experiments here reported, Prof. C-T.Chen and Dr. Guiling Wang (CAS, Beijing) for their generous and essential support in developing the 177 nm laser facility at IBM, Arthur Ellis and Joe Santilli for their expert technical support, and Dr. Thomas Theis and Prof. T. Sakurai for their unfailing support and encouragement.

REFERENCES

- 1) E. Bauer, Surf. Sci. **299/300** (1994) 102-115; W. Telieps and E. Bauer, Surf. Sci. **162** (1985) 163-168
- 2) E. Brueche, Z. Phys. (1933) 448
- 3) M.A. O'Keefe et al. Ultramicroscopy **89** (2001) 215-241
- 4) M. Haider, H. Rose, S. Uhlemann, E. Scwan, B. Kabius, K. Urban, Ultramicroscopy **75** (1998) 52; P.E. Batson, N. Delby, O. Krivanek, Nature **418** (2002) 617-620
- 5) http://www.specs.de/cms/front_content.php?idcat=93&idart=401
- 6) S. Mathias, L. Miaja-Avila, M.M. Murnane, H. Kapteyn, M. Aeschlimann, M. Bauer, Rev. Sci. Instr. **78** (2007) 083105 and references therein
- 7) C.T. Chen, T. Kanai, X.Y. Wang, Y. Zhu, S. Watanabe, Optics Letter **33** (2008) 282 and references therein
- 8) www.toptica.de
- 9) M.C. Richardson, C.-S. Koay, K. Takenoshita, C. Keyser, Journal of Vacuum Science and Technology **B 22** (2004) 785-790
- 10) F.J. Meyer zu Heringdorf, M.C. Reuter, R.M. Tromp; Nature **412** (2001) 517
- 11) R.M. Tromp, M. Mankos, M.C. Reuter, A.W. Ellis, M. Copel Surface Review and Letters **5** (1998) 1189
- 12) E. Bauer, Microscopy and Microanalysis, **12** (2006) 347-351
- 13) R.J. Phaneuf, A.K. Schmid, Physics Today **56**, no.3, March 2003

- 14) J.B. Hannon and R.M. Tromp; Annual Review of Materials Research, **33** (2003) 263
- 15) R.M. Tromp and J.B. Hannon, Surf. Rev. Lett. **9**, (2002) 1565-1593
- 16) S.Y. Tong, Surf. Sci. **299/300** (1994) 358
- 17) J.M. MacLaren, J.B. Pendry, P.J. Rous, D.K. Saldin, G.A. Somorjai, M.A. van Hove, D.D. Vvedensky, 'Surface Crystallographic Information Service; A Handbook of Surface Structures', D. Reidel Publishing Company (1987)
- 18) J. B. Hannon, J. Sun, K. Pohl, and G. L. Kellogg; Phys. Rev. Lett. **96** (2006) 246103
- 19) F.J. Himpsel, Adv. Phys. **32**, 1 (1983)
- 20) K. Kuepper, M. Buess, J. Raabe, C. Quitmann, and J. Fassbender; Phys. Rev. Lett. **99** (2007) 167202 and references therein
- 21) S. Anders et al., Rev. Sci. Instrum. **70** (1999) 3973
- 22) W. Wan, J. Feng, H. A. Padmore and D. S. Robin; Nucl. Instr, Meth. **A519** (2003) 222-229
- 23) H. Rose and D. Krahl, in Energy Filtering Transmission Electron Microscopy, Chapter 2 (L. Reimer, Editor; Springer Series in Optical Sciences Volume 71, 1995)
- 24) S. Uhlemann & H. Rose; Optik **96** (1994) 163
- 25) L. H. Veneklasen, Ultramicroscopy **36** (1991) 76
- 26) R.M. Tromp, J.B. Hannon, Y. Fujikawa, to be published
- 27) Y. Fujikawa, T. Sakurai, R.M. Tromp, Phys. Rev. Lett. submitted
- 28) G.F. Rempfer and M.S. Mauck, Optik **92** (1992) 3-8
- 29) R. Fink, M. R. Weiß, E. Umbach, D. Preikszas, H. Rose, R. Spehr, P. Hartel, W. Engel, R. Degenhardt, H. Kuhlenbeck, R. Wichtendahl, W. Erlebach, K. Ihmann, R. Schlögl, H.-J. Freund, A.M. Bradshaw, G. Lilienkamp, Th. Schmidt, E. Bauer, G. Benner, J. Electr. Spectrosc. Rel. Phen. **84** (1997) 231-250

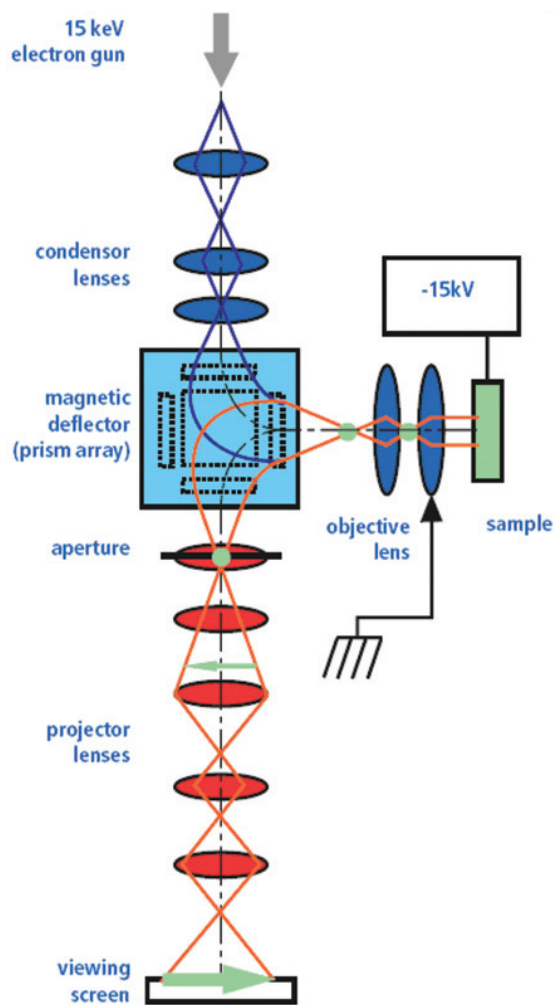


Figure 1. LEEM Optical System.

15 keV electrons originating from the gun are deflected to the sample by the 90° magnetic deflector. The electrons are decelerated between objective lens to an energy between 0 and 100 eV. After reflection from the sample the same magnetic deflector steers the electrons into the projector column. Either a real space image, a diffraction pattern, or an energy spectrum can be displayed on the viewing screen. The sample can also be illuminated by a UV light source from the side.

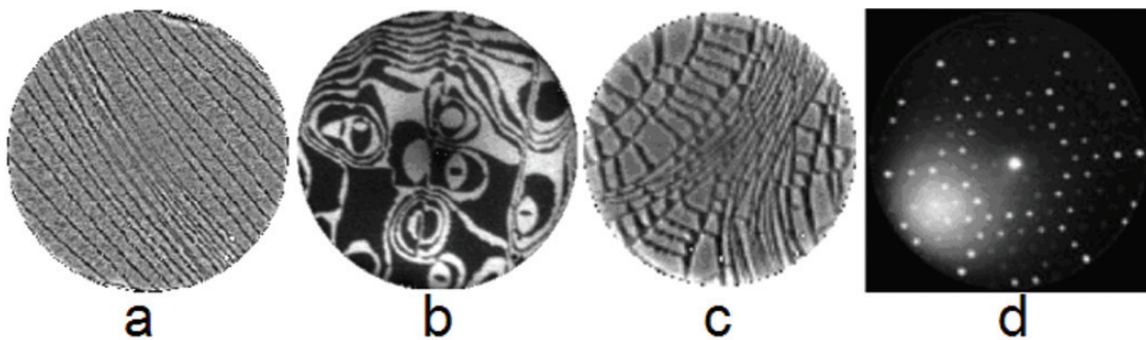


Figure 2. Basic LEEM Imaging Modes

- a-Bright field Si(111) image using the specular LEED diffracted beam. Atomic steps are visible.
- b-Dark field Si(001) image using a $(\frac{1}{2}, 0)$ LEED diffracted beam. Alternating atomic terraces light up as the reconstruction rotates by 90° from terrace to terrace
- c-Mirror mode Si(111) image at ~860 °C . The electrons turn around just before hitting the sample. Contrast is visible between Si(111) (7x7) and (1x1) areas.
- d-LEED pattern of the Si(111) (7x7) surface

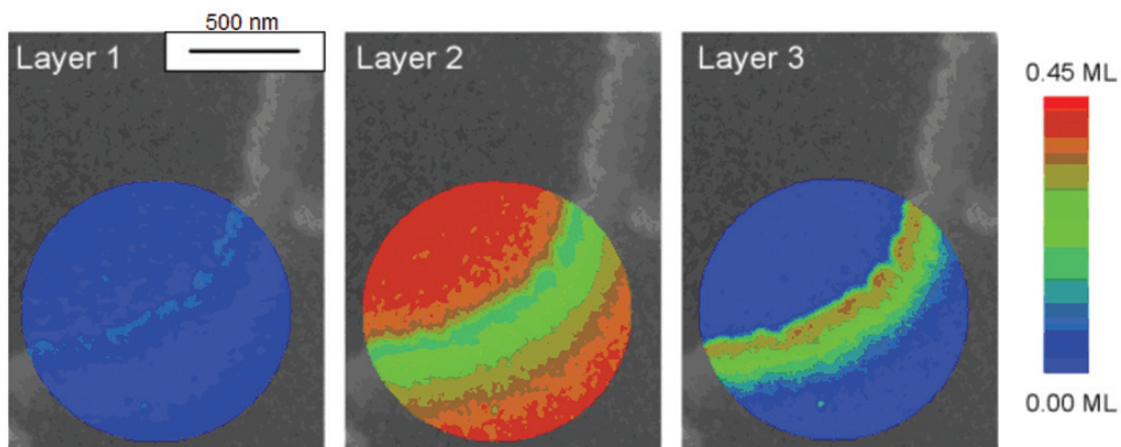


Figure 3. Concentration of Pd in the first three atomic layers of a Cu(001) crystal, shown in the colored circles superimposed on a LEEM image obtained at 13.1 eV, after evaporation of 0.45 monolayer Pd at 200°C . An atomic step runs from the lower left to the upper right. The lower atomic terrace is on the upper left.

The outermost atomic layer contains almost no Pd, as the Cu atoms have a lower surface energy. Pd atoms are buried by the advancing atomic step, but Pd atoms in the second and third layer repel each other, explaining why a higher concentration in the third layer corresponds with the reduced concentration in the second layer. These data were obtained by quantitative analysis of the LEED spot intensities as a function of electron energy for each pixel of the real space image.

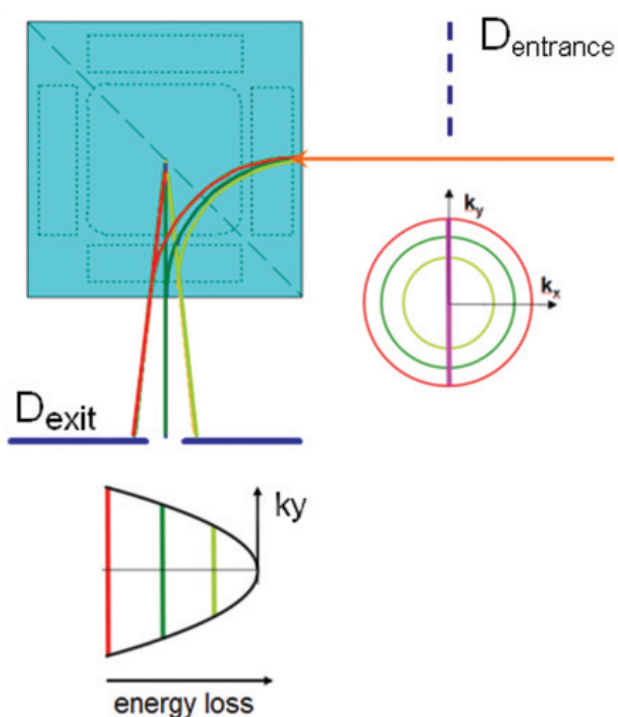


Figure 4. Basic Operation of the Prism Array as an Energy Filter

In the diffraction entrance plane (D_{entrance}) the angular distributions of electrons with increasing energy form concentric discs with increasing diameter (light green, dark green, red). A (pink) slit is placed across these discs to select a slice for a given value of k_x , here shown across the center of the discs. The length of the slit is orthogonal to the plane of the drawing.

On their path through the prism array electrons with different energies are dispersed in angle. In the diffraction exit plane (D_{exit}) we then observe the dispersed E- k_y distribution, which can be projected directly onto the viewing screen, in the same way that a diffraction pattern can be projected onto the viewing screen.

Alternatively, an energy selection aperture can be used to select an energy of interest in the spectrum, and a real space, energy filtered image can be projected onto the viewing screen. The dispersed rays, traced backward, converge in the diagonal plane of the prism array, which is therefore achromatic. The objective lens system places an image in this diagonal plane, so that dispersion does not negatively affect image quality.

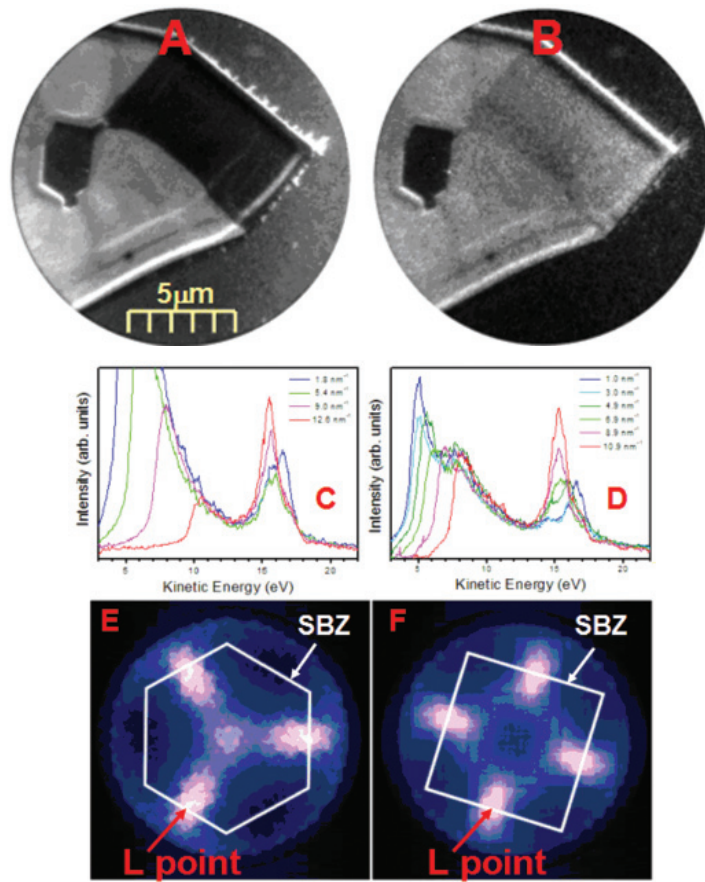


Figure 5. Energy filtered imaging and angle resolved photoemission from a compound Ag island grown on Si(111)

a-Energy filtered secondary electron image. The lighter island area is Ag(111), while the darker area is Ag(001), as determined by selected area Low Energy Electron Diffraction. The contrast difference is due to a difference in final states.

b-Energy filtered d-electron image. Ag(111) and Ag(001) areas have similar intensities, while the Si substrate is dark

c-Electron energy spectra obtained on a 3 μm diameter area on Ag(111)

d-Electron energy spectra obtained on a 3 μm diameter area on Ag(001)

e-Angular distribution of the electron intensity on Ag(111) at a binding energy of 5.7 eV. The surface Brillouin zone (SBZ) is shown in white outline. Strong resonances at the boundary of the surface Brillouin zone, corresponding to the bulk L point, are seen with 3-fold symmetry.

f-Same as (e) for Ag(001), at a binding energy of 5.9 eV. Now the symmetry of the resonance is 4-fold.

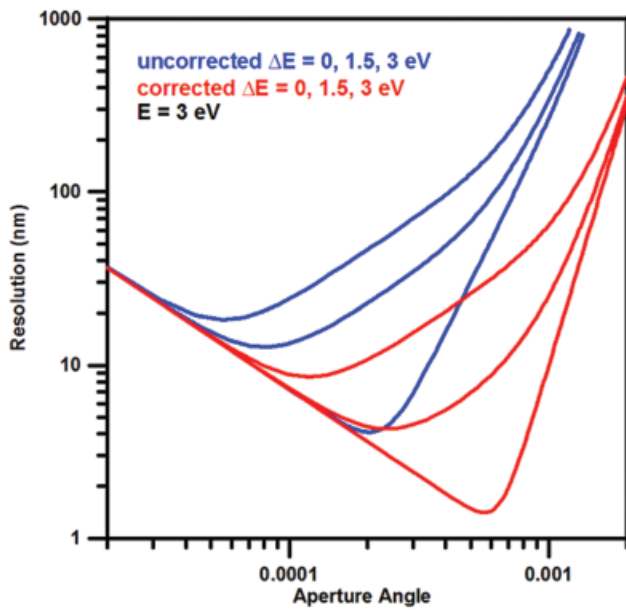


Figure 6. Effect of aberration correction on resolution and transmission.

The figure shows resolution as a function of aperture angle. Blue lines are for an uncorrected microscope, with an electron energy of 3 eV at the sample, and with energy spreads of 0, 1.5, and 3 eV. The best resolution, for $\Delta E=0$ is about 4 nm, at an aperture angle of ~ 0.0002 radians. Red curves are obtained after correction of both chromatic and spherical aberration. For $\Delta E=0$ the resolution improves by a factor 3, while the optimum aperture angle increases by a factor 3, corresponding to an increase in transmission of a factor 9. Similar improvements in resolution and transmission are seen for $\Delta E=1.5$ eV and $\Delta E=3$ eV.

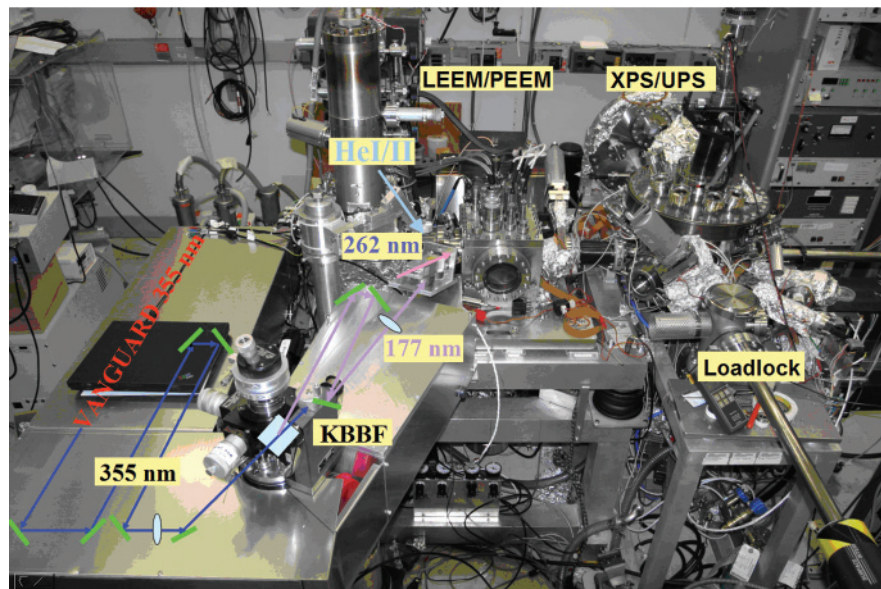


Figure 7. Configuration of the spectroscopic LEEM/PEEM system at the IBM T.J. Watson Research Center. The LEEM/PEEM system is on the left, coupled to a dedicated XPS/UPS system on the right. The LEEM/PEEM is equipped with the in-line energy filter described in this paper, a HeI/HeII discharge light source, as well as 262 nm and 177 nm pulsed laser systems, and a Hg discharge lamp.

The Salient Point of Research

List of the salient of presentation at “Challenge of Interdisciplinary Materials Science to Technological Innovation of the 21st Century”

1. C. T. Liu (Univ. of Tennessee)
“Shear-band dynamics and fracture strength of bulk metallic glasses (BMGs)”
2. A. R. Yavari (WPI-AIMR and Grenoble Institute of Technology)
“Giga-strength micro- and nano-structures “chill-zone” alloys from glass-forming alloys outside the glass-forming composition range”
3. T. Yamasaki (Univ. of Hyogo)
“Viscous flow behaviours of $Zr_{55}Cu_{30}Al_{10}Ni_5$ bulk metallic glasses over the entire temperature range”
4. W. H. Wang (Chinese Academy of Sciences)
“Unique properties of new rare-earth-based bulk metallic glasses”
5. J. H. Perepezko (Univ. of Wisconsin-Madison)
“Bulk Liquid Undercooling and Nucleation Kinetics Analysis”
6. Y. Shibutani (Osaka Univ.)
“Deformation-Induced Free Volume Evolution of Computational Binary Amorphous Alloys”
7. M. Tsukada (WPI-AIMR and Waseda Univ.)
“Theory of Scanning Probe Microscopy and Transport for Nano- Structures”
8. X. F. Jin (Fudan Univ.)
“Interfacial Spin Frustration at Mn/Ni/Cu(001)”
9. V. Crespi (Penn State Univ.)
“Islands and roads at the nanoscale: Universal trends in the theory of two-dimensional growth (of SAMS) and one-dimensional bisection (of nanotubes) on substrates”
10. A. Al-Mahboob (WPI-AIMR)
“LEEM study of organic molecular film growth”
11. W. Song (Chinese Academy of Sciences)
“Nanostructured Metal Oxides: Facile Synthesis methods and Promising Applications”
12. P. Harrowell (Univ. of Sydney)
“Characterizing the Geometry and Composition of Long-Lived Structural Fluctuations in Supercooled Alloys”
13. H. Teichler (Univ. of Goettingen)
“Dynamical heterogeneity in glass forming NiZr bulk melts and nanosized two-dimensional films.-Molecular dynamics results”
14. Y. Hirotsu (Osaka Univ.)
“Medium Range Order Structures and their Changes in the Course of Primary Crystallization in some Metallic Glasses”

15. D. V. Louzguine-Luzgin (WPI-AIMR)
“Nanocrystallisation of high-strength Al-based metallic glasses”
16. K. Fujita (Ube National College of Technology)
“Fracture Toughness and Fatigue Strength in Bulk Metallic Glasses”
17. P. V. Sushko (WPI-AIMR)
“Electronic excitations, charge trapping and defect formation in oxides and oxide nanostructures”
18. T. Gessner (WPI-AIMR, Fraunhofer Institute for Reliability & Microintegration and Chemnitz Univ. of Technology)
“NEMS, MEMS - issues of smart systems integration”
19. J. Zi (Fudan Univ.)
“Propagation of liquid surface waves in periodic structures”
20. T. Hashizume (WPI-AIMR, Hitachi, Ltd. and Tokyo Institute of Technology)
“Interface of organic devices by Scanning probe microscopy”
21. K. Uosaki (Hokkaido Univ.)
“Formation of Two-dimensionally Ordered Atomic/molecular Layers at Solid/liquid Interfaces as New Functionality Materials”
22. T. Adschiri (WPI-AIMR)
“Supercritical hydrothermal synthesis of organic inorganic hybrid nanocolloids”
23. Y. Fujikawa (Tohoku Univ.)
“Five-Dimensional Spectromicroscopy Probing Slow Electrons”
24. K. Nakajima (WPI-AIMR)
“Nanofishing of a Single Polymer Chain”

Shear-banding dynamics detected in bulk metallic glasses (BMGs)

Cang Fan, B. Yang, **C. T. Liu***, P. K. Liaw, and T. G. Nieh

Department of Materials Science and Engineering

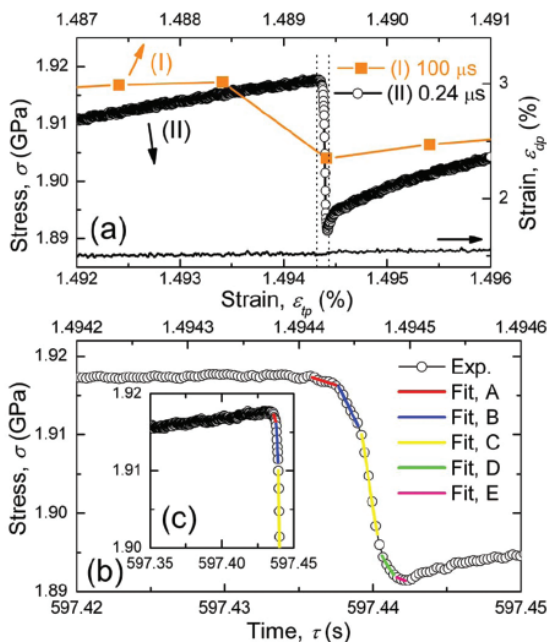
The University of Tennessee, Knoxville TN 37996 USA

*Phone: 865-574-4459; Fax: 865-576-6298

E-mail: liuct@ornl.gov

Contrary to abrupt linear unloading spikes seen in conventional investigations of shear-band deformation of BMGs, we surprisingly observed these stress relief spikes to be nonlinear in nature over fine time scales, recorded by a fast data collection (FDC) system. The dynamic behavior of shear-band glide in BMGs involves five steps: initiation, acceleration, viscous glide, deceleration, and arrest. The shear-band sliding velocity is estimated to be very low, around 0.5 mm per sec, consistent with viscous gliding.

Shear load drop is nonlinear in nature as recorded by FDC



- The shear load drop at 1.5% strain

Curve (I) by CDC

Curve (II) by FDC

- 100% increase in load drop by FDC

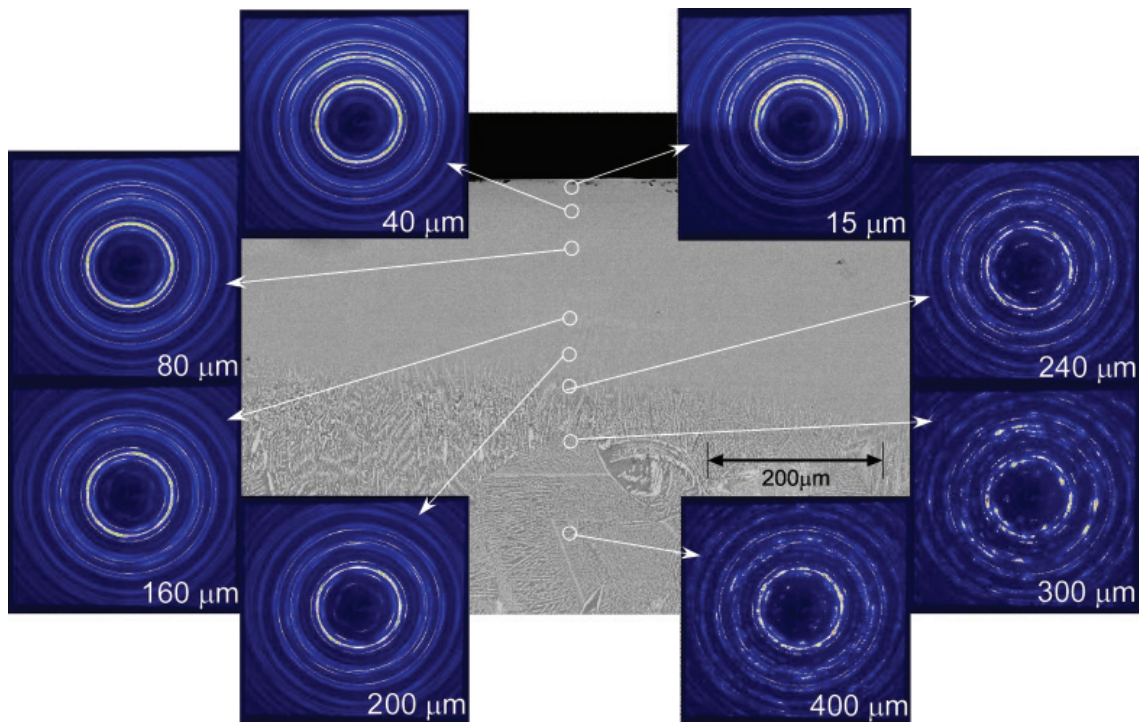
- The FDC curve with an expanded Y axis that the dynamic behavior of shearbanding includes five stages:

Initiation, acceleration, fast glide, deceleration, and, arrest

Giga-strength micro- and nano-structures “chill-zone” alloys from glass-forming alloys outside the glass-forming composition range

A. R. Yavari
(WPI-AIMR and Grenoble Institute of Technology)

E-mail: yavari@ltpcm.inpg.fr



X-ray micro-profiling using 90 keV synchrotron light in transmission on the cross-section of a Cu₉₀Zr₅Hf₅ copper mold cast slab with scratch resistant nanostructures surface layer.

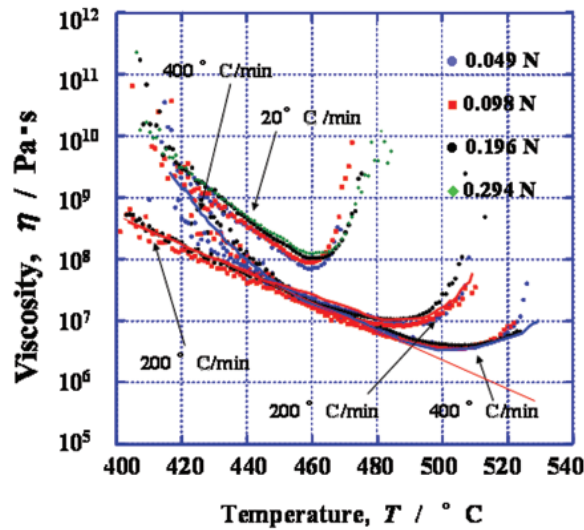
The diffraction patterns from near the surface produce continuous diffraction rings typical of small equiaxed crystals. Further into the surface layer the rings break up into discontinuous streaks then spots [from “Chill-zone copper with strength of stainless steel and tailorable color”, A.R. Yavari, K. Ota, K. Georgarakis, A. LeMoulec, F. Charlot, G. Vaughan, A.L. Greer and A Inoue, *Acta Mater.* In press]

Viscous Flow Behaviours of $Zr_{55}Cu_{30}Al_{10}Ni_5$ Bulk Metallic Glasses over the Entire Temperature Range

T. Yamasaki¹), Y. Tanimoto¹), T. Kikuchi¹), Y. Yokoyama²),
T. Ishikawa³), H. M. Kimura²) and A. Inoue²)

1) University of Hyogo, Japan, 2) IMR, Tohoku University, Sendai, Japan,
3) JAXA, Ibaraki, Japan

E-mail: yamasaki@eng.u-hyogo.ac.jp

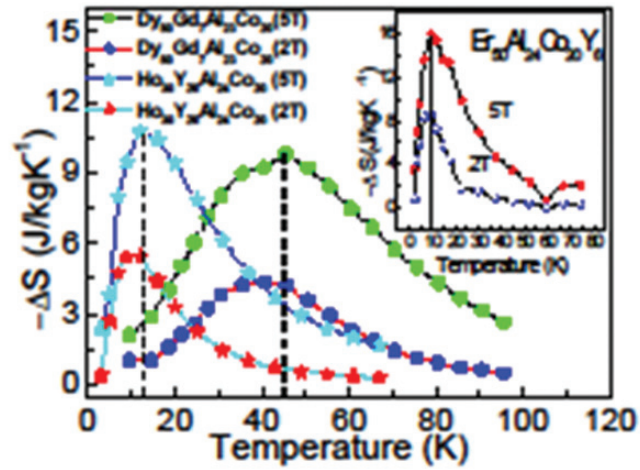


Viscosity of the $Zr_{55}Cu_{30}Al_{10}Ni_5$ supercooled liquids was quite independent of the various applied loads. However, when the sample was slowly heated at the rate of $20\text{ }^{\circ}\text{C}/\text{min}$, viscosity exhibited relatively high values that may be mainly due to the skin effects of oxides. With increasing the heating rate to $200\text{ }^{\circ}\text{C}/\text{min}$ and above, viscosity largely decreased indicating the equilibrium viscosity may be measured in these heating conditions.

Unique properties of new rare-earth-based bulk metallic glasses

W. H. Wang (Chinese Academy of Sciences)

E-mail: whw@aphy.iphy.ac.cn

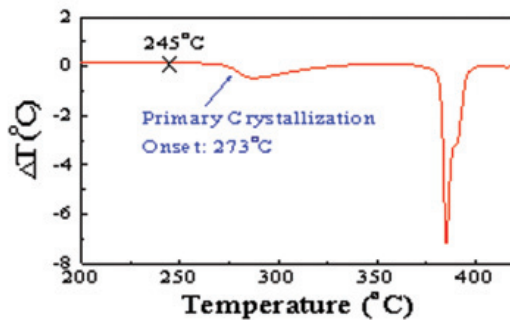
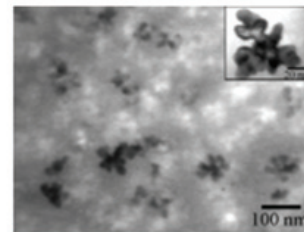
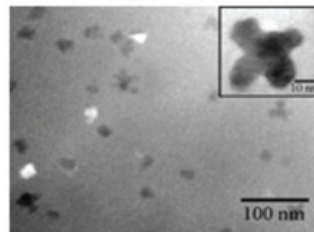
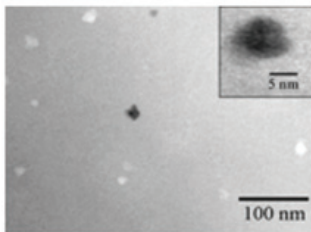
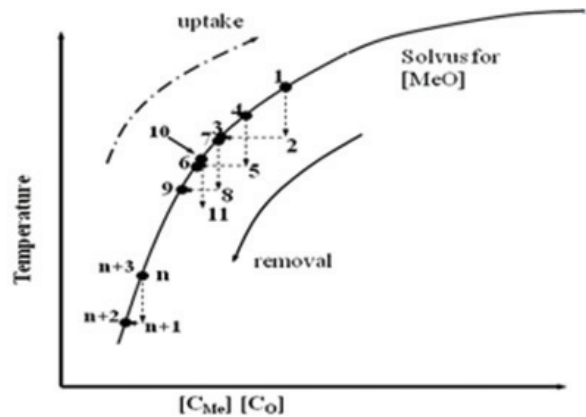


Magnetic entropy changes as a function of temperature for $\text{Ho}_{30}\text{Y}_{26}\text{Al}_{24}\text{Co}_{20}$ (triangle) and $\text{Dy}_{50}\text{Gd}_7\text{Al}_{23}\text{Co}_{20}$ (square) BMGs under 2 T and 5 T (the inset is for $\text{Er}_{50}\text{Al}_{24}\text{Co}_{20}\text{Y}_6$)

Bulk Liquid Undercooling and Nucleation Kinetics Analysis

J. H. Perepezko (Univ. of Wisconsin-Madison)

E-mail: perepezk@engr.wisc.edu



Crystallization of α -Al nanocrystals occurs at temperatures below 273 $^{\circ}C$ and the growth of the nanocrystals is impeded when the diffusion field impingement occurs

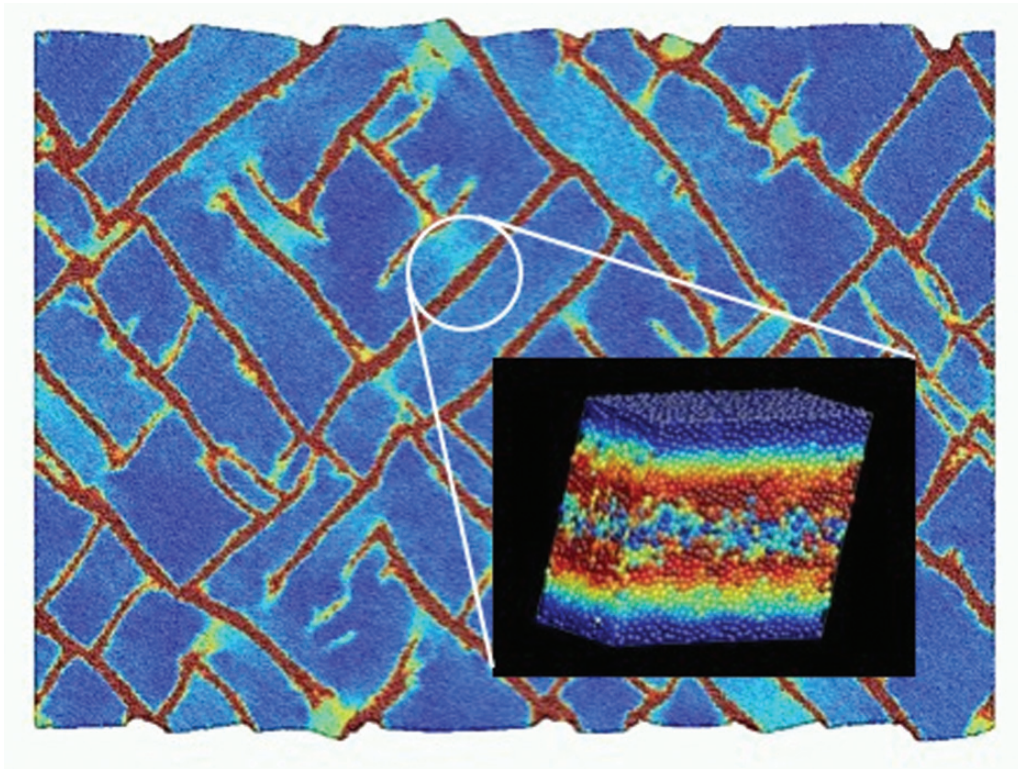
■ Annealing of Melt-Spun $Al_{88}Y_7Fe_5$

Metallic glass formation requires a large liquid undercooling that is controlled by heterogeneous nucleation. Rapid cooling is often used to achieve metallic glasses, but a new analysis of undercooling shows that nucleant refining can be effective. In addition, a number of useful properties can be obtained by annealing metallic glass to develop nanocrystalline materials.

Deformation-Induced Free Volume Evolution of Computational Binary Amorphous Alloys

Y. Shibutani (Osaka Univ.)

E-mail: sibutani@mech.eng.osaka-u.ac.jp



This figure indicates the multiple shear banding of binary amorphous alloy under the uniaxial loading by molecular dynamics simulations. The localized deformation can be achieved by the 2-D model with plane-stress condition, while the 3-D model as the small illustration realizes the main band with the finite width.

Theory of Scanning Probe Microscopy and Transport for Nano-Structures

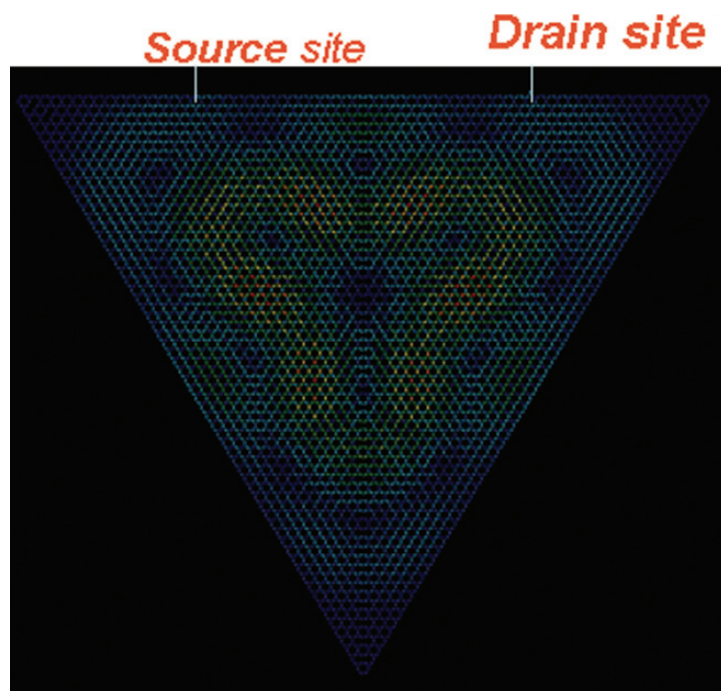
M. Tsukada (WPI-AIMR and Waseda Univ.)

E-mail: tsukada@cms.nano.waseda.ac.jp



Professor Masaru Tsukada

Theory of Scanning Probe Microscopy and Transport of Nano-Structures

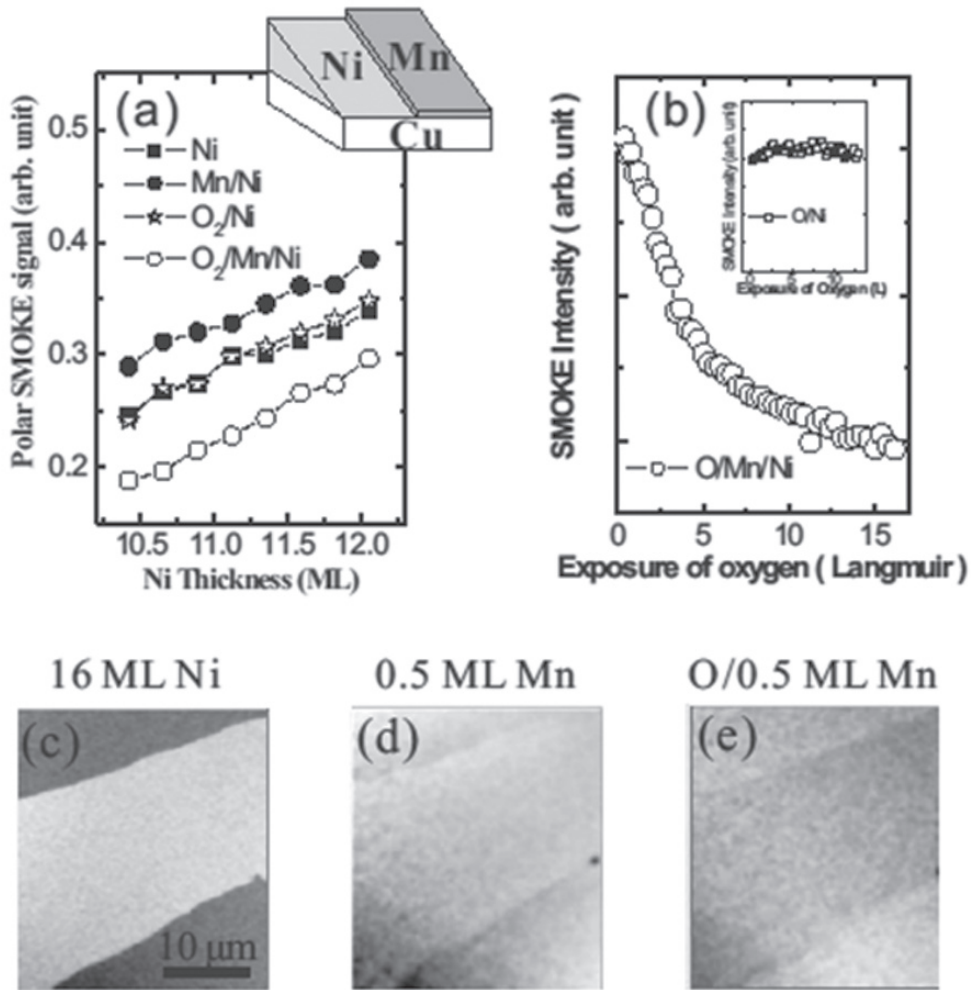


Theory predicts that a strong loop current is induced by a small bias voltage inside the triangular graphene enclosing a wide area. The current strength is by more than ten times larger than the source drain current. This type of the quantum current is predicted for various nano-scale structures including the donuts of carbon nanotube, and some organic molecules.

Interfacial Spin Frustration at Mn/Ni/Cu(001)

X. F. Jin (Fudan Univ.)

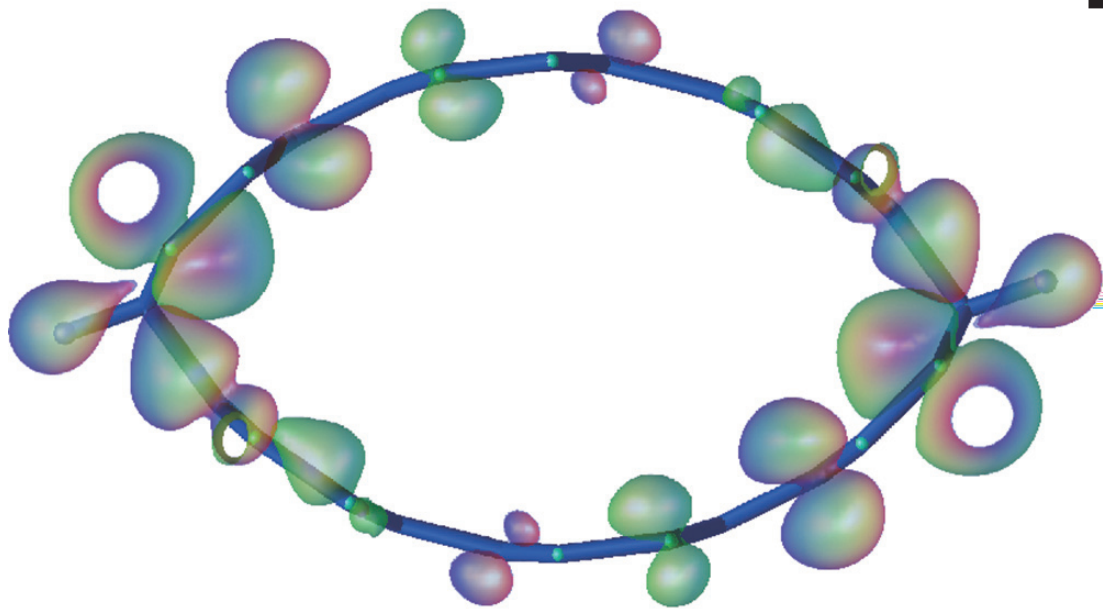
E-mail:xfjin@fudan.edu.cn



Islands and roads at the nanoscale: Universal trends in the theory of two-dimensional growth (of SAMS) and one-dimensional bisection (of nanotubes) on substrates

V. Crespi (Penn State Univ.)

E-mail: vhc2@psu.edu



A nanotube bisected by two opposing rows of chemisorbed hydrogen atoms bisects the low-energy electronic states and so generates a new physical regime wherein vibrational energy scales exceed electronic energy scales.

LEEM study of organic molecular film growth

A. Al-Mahboob, J. T. Sadowski, Y. Fujikawa and T. Sakurai
(WPI-AIMR)

E-mail: almahb-0@imr.tohoku.ac.jp

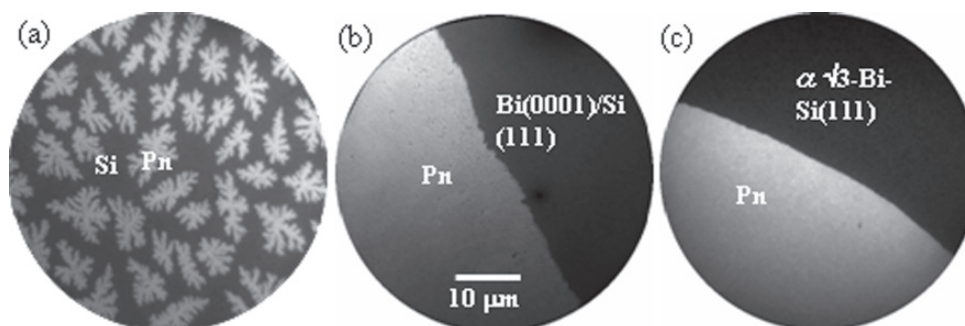


Fig.1. (a)-(c) LEEM images showing (001)-oriented Pn growth (bright contrast) on various substrates (dark contrast): (a) Fractal growth on clean Si(111)-7x7 surface – disordered wetting layer is formed before nucleation of standing-up structure; Pn film is textured; (b)-(c) Step flow-like growth of compact Pn island on Bi(0001)/Si(111) and $\alpha\sqrt{3}$ -Bi-Si(111) are observed; The first layer single crystalline domain size are exceeding 200 and 100 μm in diameter respectively; Pn grown on Bi(0001)/Si(111) is the first reported (001)-oriented epitaxial film.

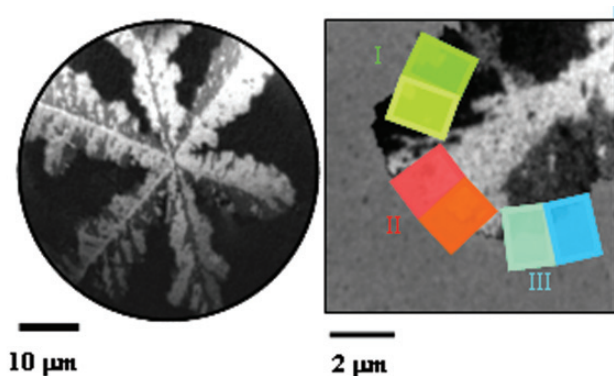


Fig.2. (a) Tilted-bright-field LEEM image showing microstructure within a Pn island on H-Si(111) and (b) tip of the one of the branches in Pn island with three distinctive contrasts (I, II, III) visible; Pn 2D crystal alignment depicted from μ -EED patterns are outlined in (b), shorter and longer sides of each rectangle corresponds to a - and b -axes respectively; A Pn island is textured inside, even it evolved from a single nucleus.

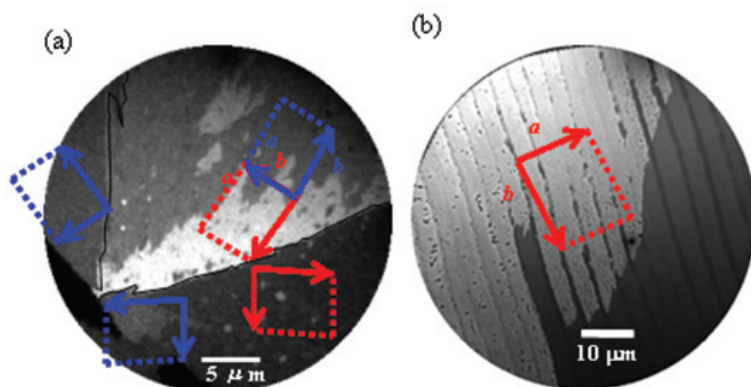


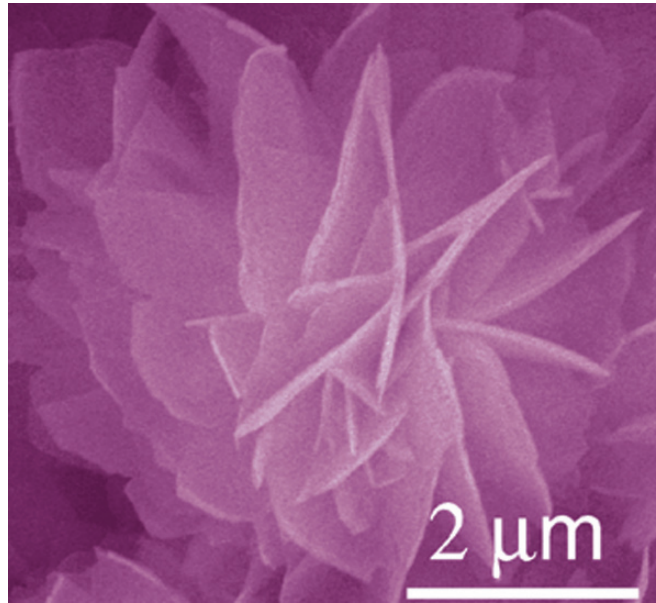
Fig.3. LEEM images of Pn domains: (a) Tilted dark-field LEEM image showing rotational Pn domains on trigonal Bi(0001)/Si(111) substrate, additional

contrast of chiral twin is visible within a rotational domain; each domain is directed along their b directions; (b) Pn (bright contrast) on self patterned Bi(0001) substrate (grey contrast), separated by disordered Bi region (dark contrast) which limits Pn molecule's diffusion across it (dark contrast), having Pn b -axis closely parallel to strip direction over the surface within the limit of epitaxial relation; Outlined is the unit cell orientations depicted from μ -LEED patterns.

Nanostructured Metal Oxides: Facile Synthesis methods and Promising Applications

W. Song (Chinese Academy of Sciences)

E-mail: wsong@iccas.ac.cn



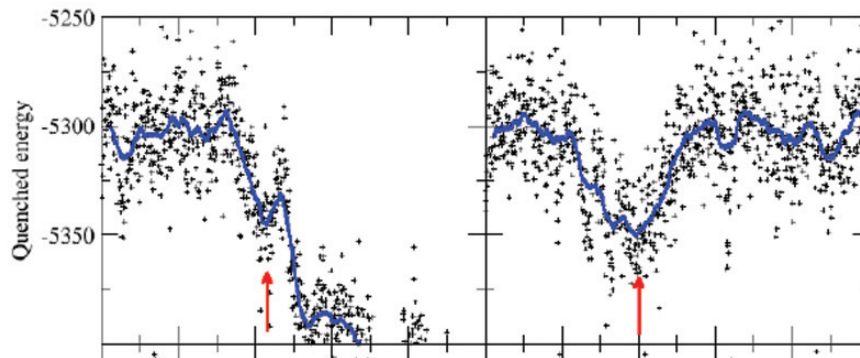
Nanostructured Metal Oxides: Facile Synthesis methods and Promising Applications

Hierarchically structured metal oxides have two or more levels of structures that respectively satisfy our requirements for desired materials. Facile synthesis methods are developed for various metal oxides, which show promising potentials in water treatment and nano catalysis.

The Geometry and Composition of Long-Lived Structural Fluctuations in Supercooled Alloys: Simulations Studies

Peter Harrowell(University of Sydney)

E-mail:peter@chem.usyd.edu.au

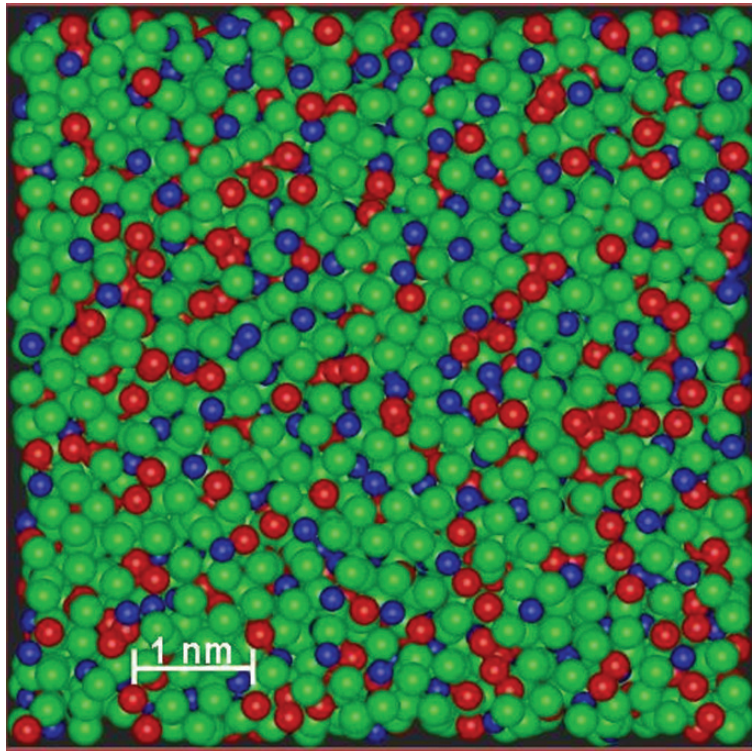


Plots of the potential energy (after a steepest decent minimization) vs time for two different simulations of a supercooled binary liquid mixture. On the left we see the steady drop in energy associated with crystallization. On the right, we observe the supercooled liquid experiences many large fluctuations in the quenched potential energy. These are associated with structural fluctuations characterized by imperfect crystal order.

Dynamical heterogeneity in glass forming NiZr melts. - Molecular dynamics results.

H. Teichler

(Institute for Materials Research and SFB 602, University of Goettingen, Germany)



Atomic arrangement in the bulk glass forming Al₁₅Ni₂₅Zr₆₀ melt from computer modeling.

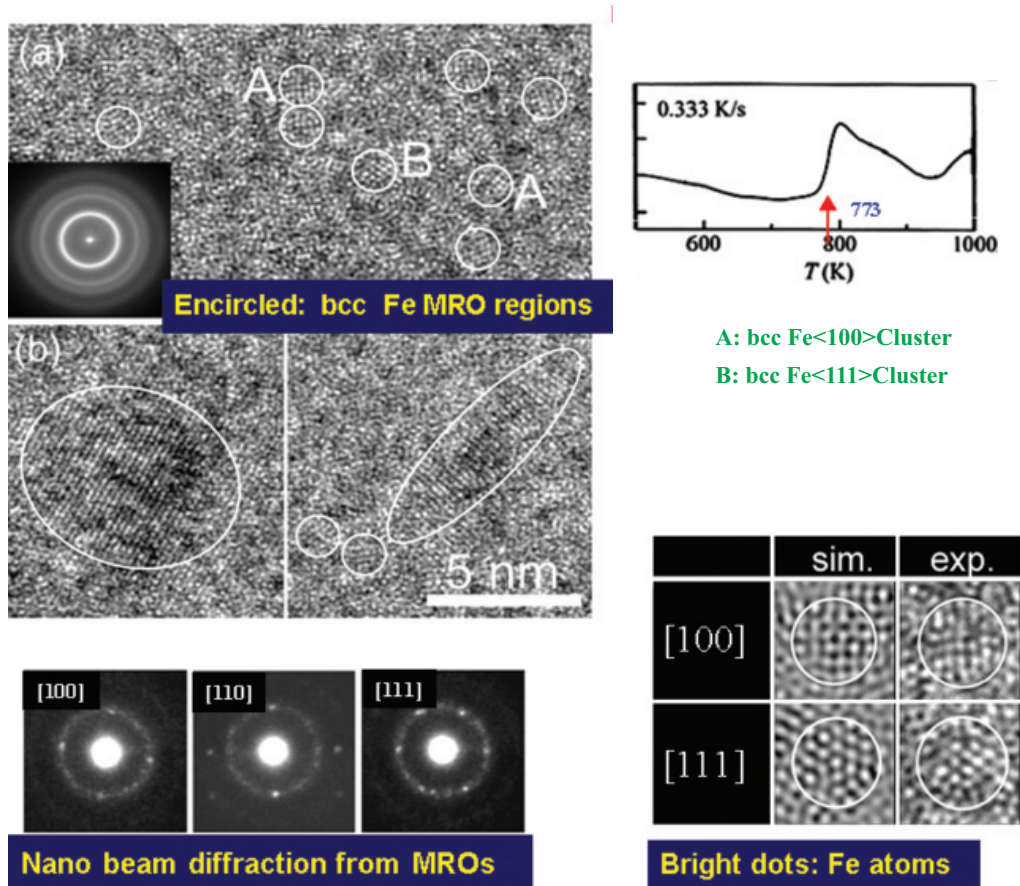
(M. Guerdane and H. Teichler, Phys. Rev. B, 014203 (2001))

The cross-section displays a marked medium range order in the structure, consisting of chains of Al-atoms (red) within the Zr-matrix (green), and Ni-atoms (blue) immersed in between, the latter avoiding direct Ni-Ni contacts. The structure is the result of thermal relaxation processes taking place as heterogeneous dynamics in form of correlated motions of whole chains of atoms. It means a highly complex, rather stable amorphous arrangement significantly different from crystalline nuclei.

“Medium Range Order Structures and their Changes in the Course of Primary Crystallization in some Metallic Glasses” Y. Hirotsu

(Osaka Univ.)

E-mail: yhirotsu@sanken.osaka-u.ac.jp



MRO structures extended in alloys of low-glass-forming-ability have strong structural similarities to the primary phases in crystallization, and have potentials to become nuclei in the course of the primary crystallization. In $\text{Fe}_{84}\text{Nb}_7\text{B}_9$ glass, MROs with the bcc-Fe structure are formed in the glass formation and are grown gradually in the course of annealing to become nuclei of the primary α -Fe crystals. After annealing at 773K, bcc-MROs are clearly observed by high-resolution TEM(a). Occasionally, we observe α -Fe crystals among the bcc-MROs (b). Simulated images of bcc-MROs along the beam directions of [100] and [111] are compared with MRO images at A and B indicated in (a), respectively. Also shown are nano-beam diffraction patterns from the bcc-MROs.

Nanocrystallisation of high-strength Al-based metallic glasses

D. V. Louzguine-Luzgin (WPI-AIMR)

E-mail:dml@imr.tohoku.ac.jp

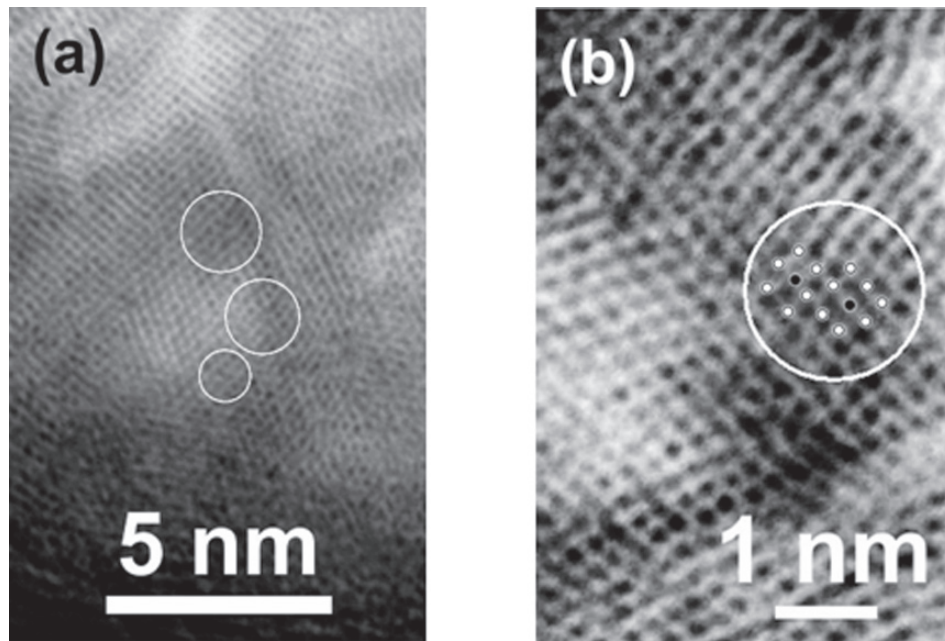


Fig. (a) and (b) high-resolution transmission electron microscopy images revealing dislocations and other defects (encircled) observed in Al nanoparticles below 10 nm is size (with extremely high number density in the order of 10^{24} m^{-3}) which were crystallized on rapid solidification of the $\text{Al}_{85}\text{Y}_4\text{Ni}_5\text{Co}_2\text{Pd}_4$ glassy alloy. The sources of these dislocations and the distortions of the crystalline lattice are believed to be impingement of the growing particles and possibly the difference in the thermal expansion coefficients of crystalline Al and the multicomponent amorphous phase. Both factors lead to stresses on cooling in a solid state. The observed dislocations are attracted to the grain boundaries but did not annihilate on them possibly owing to a high cooling rate in the order of 10^6 K/s during melt spinning.

Fracture Toughness and Fatigue Strength in Bulk Metallic Glasses

Kazutaka Fujita^{1*}, Yoshihiko Yokoyama², Wei Zhang², Baolong Shen²,
Kenji Amiya², Nobuyuki Nishiyama³, Hisamichi Kimura² and Akihisa Inoue⁴

¹ Ube National College of Technology, Department of Mechanical Engineering,
Ube 755-8555, Japan

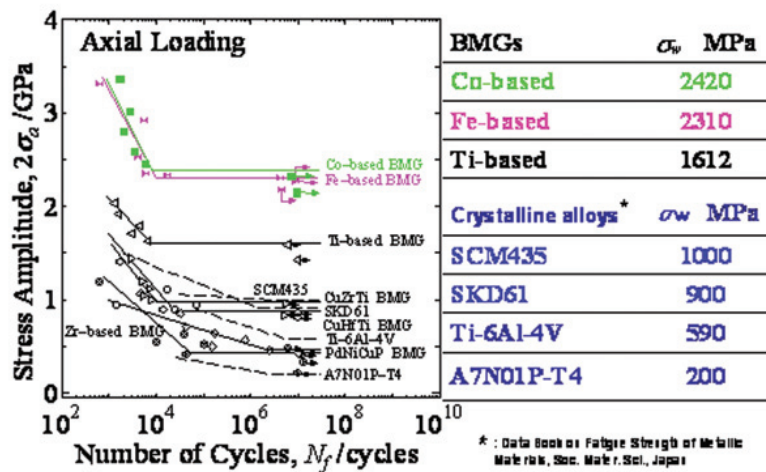
² Tohoku University, Institute for Materials Research, Sendai 980-8577, Japan

³ R&D Institute of Metals and Composites for Future Industries (RIMCOF),
Sendai 980-8577, Japan

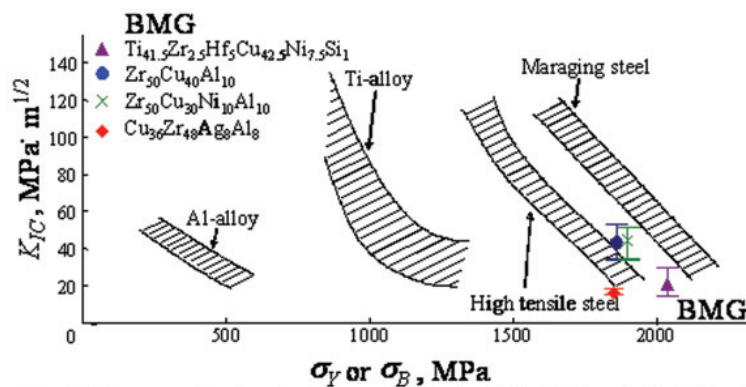
⁴ Tohoku University, Sendai 980-8577, Japan

E-mail: fujita@ube-k.ac.jp

S-N Diagrams in Fatigue Test fatigue limit(σ_w)



Comparison between Plane-Strain Fracture Toughness (K_{IC}) in BMGs and Crystalline Alloys



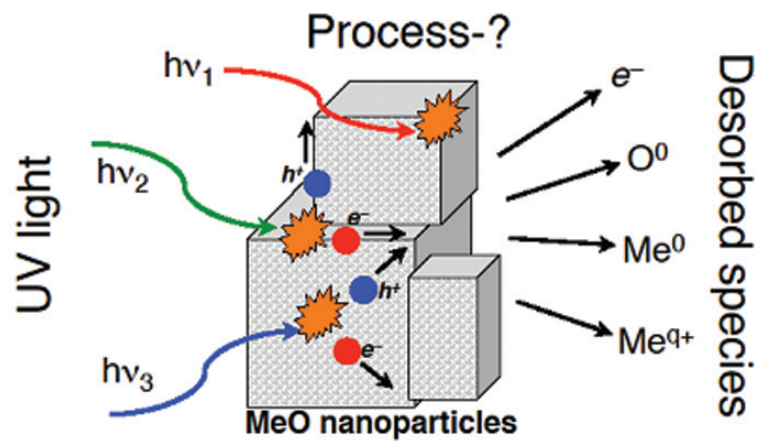
D. Broek, Elementary Engineering Fracture Mechanics, Sijthoff & Noordhoff, 1983, p.301.

Electronic excitations, charge trapping and defect formation in oxides and oxide nanostructures

P. V. Sushko

(WPI-AIMR and Univ. College London)

E-mail: p.sushko@ucl.ac.uk



Schematics of photo-induced electronic excitations, charge trapping, and desorption of atoms and ions in oxide nanoparticles exposed to ultra-violet light.

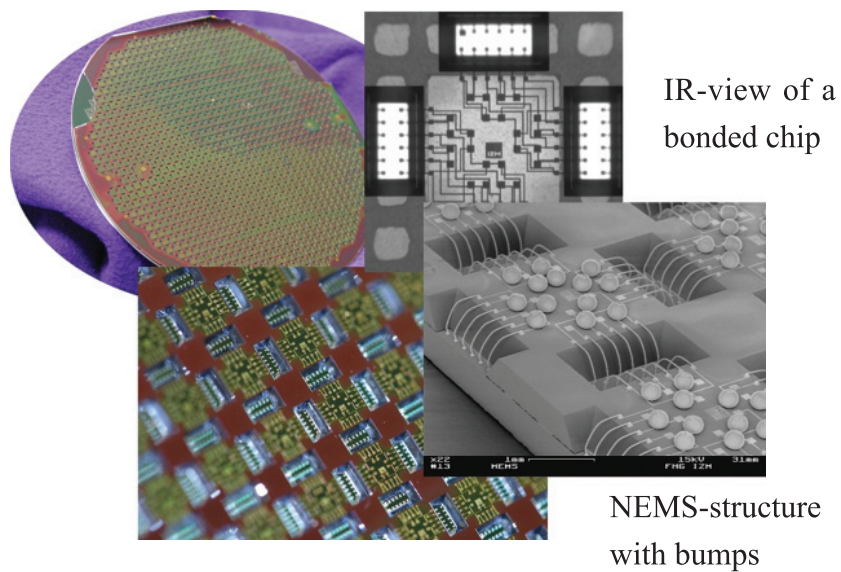
NEMS, MEMS - issues of smart systems integration

T. Gessner

(WPI-AIMR, Fraunhofer Institute for Reliability & Microintegration and Chemnitz Univ. of Technology)

E-mail: thomas.gessner@che.izm.fraunhofer.de

Wafer level integration of MEMS/NEMS



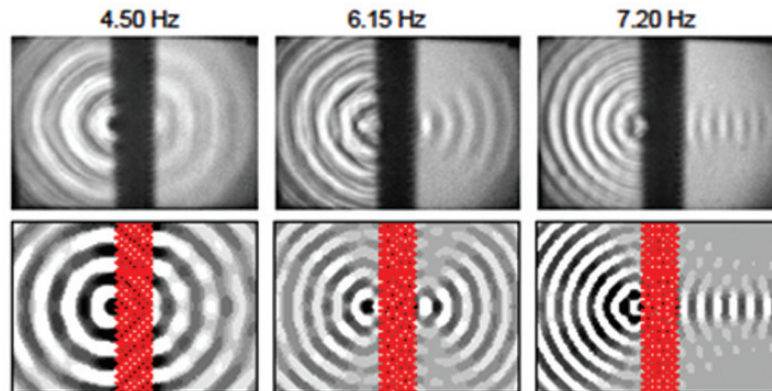
The integration of MEMS/NEMS with electronics to smart systems requires new approaches for wafer level packaging. This concerns material as well as technology aspects. The application of nano structures for interconnects is described.

“Propagation of liquid surface waves in periodic structures”

Jian Zi(Fudan University)

Email: jzi@fudan.edu.cn

Collaborators: Jiong Yang, Xiaohan Liu, Xinhua Hu, and Yunfei Tang



Observation of superlensing in liquid surface waves:

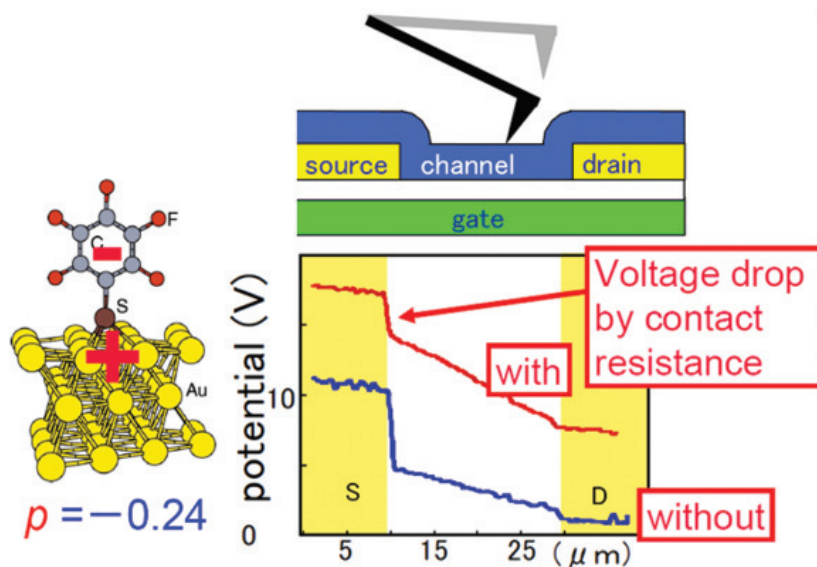
A slab of arrays of copper cylinders, arranged in a square lattice, is placed in the middle of a vessel. A point source is placed on the left side of the cylinder arrays. Top (experiment) and lower (theory) panels represent the snapshots of liquid surface wave patterns. At low frequencies (e.g. 4.5 Hz), the transmitted wave patterns are circular-like, with their centers located inside the slab, forming a virtual image. At around 6.15 Hz, an image appears outside the slab, forming a real image (middle panels). This is caused by negative refraction at the slab surfaces. With the further increase in frequency, the image shifts further to the right and becomes elongated, eventually leading to a nearly directive emission (right panels).

Interface of organic devices by Scanning probe microscopy

T. Hashizume

(WPI-AIMR, Hitachi, Ltd. and Tokyo Institute of Technology)

E-mail: tomihito.hashizume.qb@hitachi.com

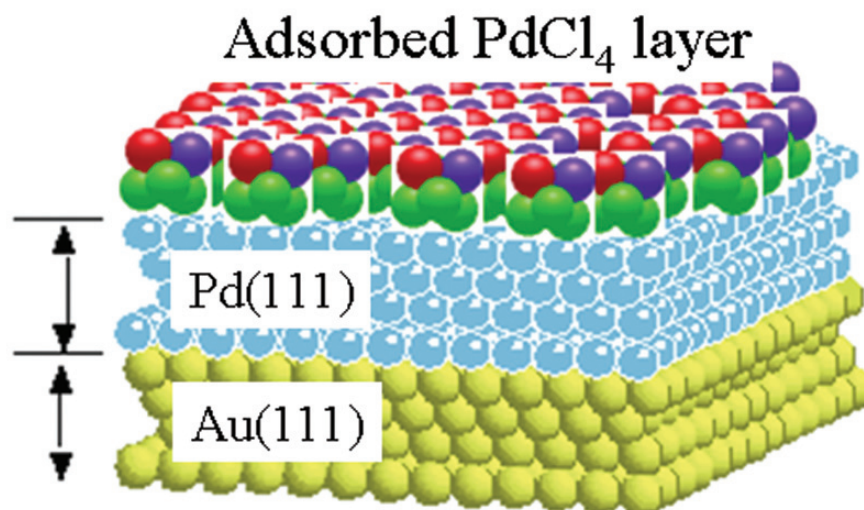


The effect of self-assembled monolayer (SAM) at the metal- semiconductor interfaces was characterized by examining voltage drops by Kelvin probe microscopy while the OTFTs were in operation.

Formation of Two-dimensionally Ordered Atomic/molecular Layers at Solid/liquid Interfaces as New Functionality Materials

K. Uosaki (Hokkaido Univ.)

E-mail: uosaki@pcl.sci.hokudai.ac.jp



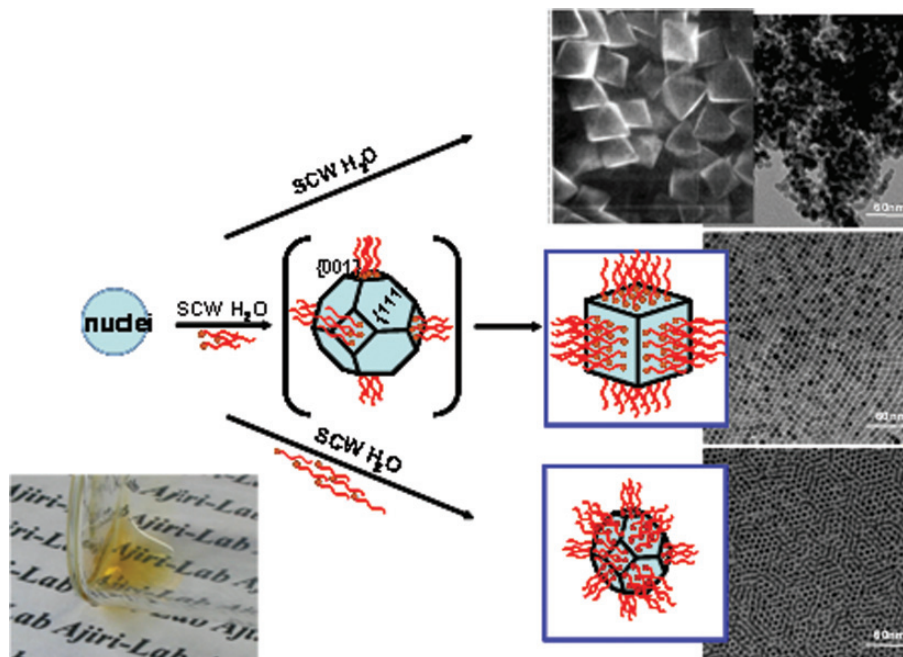
Structure of Au(111) surface during electrochemical atomic layer epitaxial growth of Pd

XRD patterns showed that Pd(111) and Pd(100) were deposited on Au(111) and Au(100), respectively. STM measurements showed the adsorption of Pd complex on both the substrate gold and deposited Pd, inhibiting the three dimensional growth of the deposits.. Surface x-ray scattering

Supercritical hydrothermal synthesis of organic inorganic hybrid nanocolloids

Tadafumi Adschiri
(WPI-AIMR)

E-mail: ajiri@tagen.tohoku.ac.jp

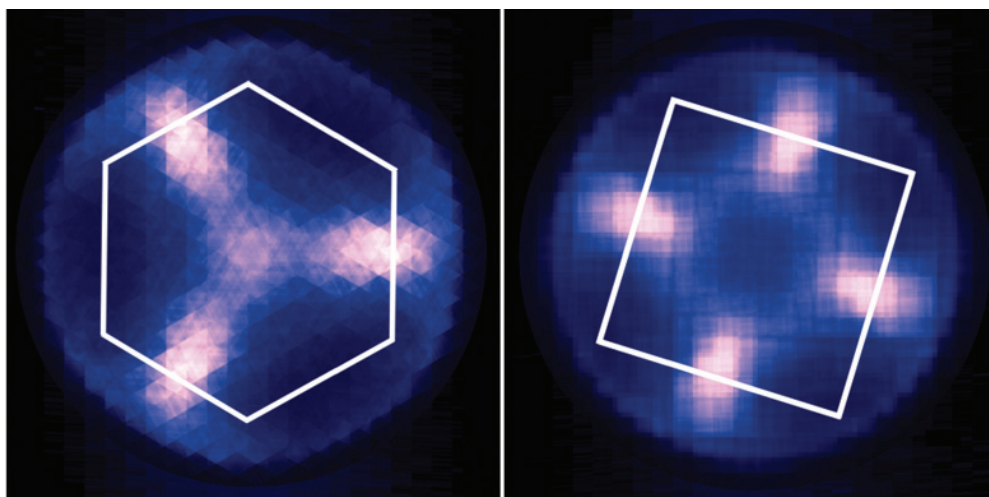


In supercritical water, organic-inorganic hybrid nanocrystals can be synthesized.

Five-Dimensional Spectromicroscopy Probing Slow Electrons

Y. Fujikawa (Tohoku Univ.)

E-mail: fujika-0@imr.tohoku.ac.jp



He-I photoelectron distributions in the 2D reciprocal space obtained from Ag microstructures formed on Si substrate, selecting Ag(111) (left) and Ag(100) (right) areas with a 4-micron aperture.

Nanofishing of a Single Polymer Chain

K. Nakajima (WPI - AIMR)

E-mail: knakaji@polymer.titech.ac.jp

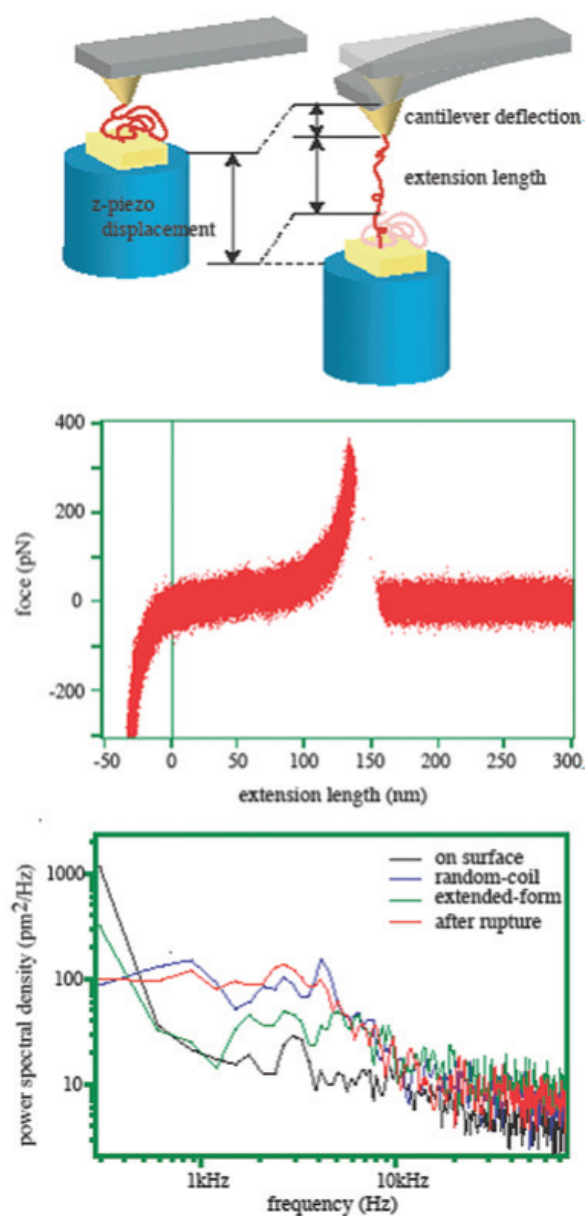


Figure (upper) The concept of nanofishing, (b) the original nanofishing data for a single polystyrene chain with high-speed data capter mode, and (c) the power spectral density calculated from nanofishing data. Four PSD signals are corresponding to four different conditions as indicated in the legend.

Interviews



Prof. Yoshinori YAMAMOTO

機構長 山本 嘉則

Interview with Yoshinori Yamamoto, Institute Director of the WPI-AIMR

In "WPI-AIMR News Vol. 1" issued on December 24, 2007, the concept/background, purpose, personnel composition, and joint research system, etc. of this research institute were clearly illustrated. Its main target is to create innovative substances or new materials through cooperation between researchers from three different disciplines of materials science, physics, and chemistry. Thirty principal investigators (PIs) are to be scouted from both inside and outside the country, and in addition we will recruit associate professors, assistant professors, and post-doctoral researchers. This will become an intelligence group where materials are researched (including basic and applied research) from the atomic level to the molecular level by a total of around 200 researchers over a 10 to 15 year period. This research institute holds the lofty ideal of contributing to the betterment of humankind by producing world-leading original and outstanding research results.

Practically, the first pillar is to achieve outstanding research results in materials science and technology, which receive attention from all over the world. The second pillar is to reform the negative elements in Japan's traditional promotion system, and to enable young researchers who can submit excellent proposals to carry out research independently and freely. Generally, young researchers in Japan have had to wait too long before pursuing their own researches independent from their supervisors. The last pillar is to destroy the barrier to communication. Since there are many participants from overseas countries, the official language we use is English. Even those of you whose mother tongue is not English are requested to carry on all communication in English, regardless of your English skills. To make a leap forward to the international stage, a precondition for all of us is that we are able to communicate in English without hesitation.

Personal exchange within the research institution is very important outstanding research results, because researchers may cooperate with each other while making the best use of their own expertise. To discover new materials and new processes and to develop new systems it is necessary to combine multidisciplinary ideas. It often happens that "common sense in specialty A is not common sense in specialty B." There are many examples where a new discovery with good prospects for the future has been produced by an approach that appeared to be contrary to common sense. For example, the use of laser ionizing for measuring the mass of a protein would probably not appear to be productive to an expert in this research field, because he/she knows that a protein is easily broken up. However, it was Koichi Tanaka, a newcomer to this research field who combined

laser ionizing of protein with TOF, an experiment which led to his winning a Nobel Prize.

It is increasingly found that specialists in their own fields are so fixated on standard knowledge that they find it difficult to take a drastic leap. In making a leap forward, youth is often the catalyst. There are a lot of examples when a productive combination of a newcomer and an old-timer has produced significant results.

This institute is encouraging daily teatime discussions, monthly meetings, and mini symposia with outside joint researchers to promote exchange between persons of different specialties. We want to improve creativity dramatically by cooperative research based on various free, large and small discussion formats.

I think it will be better for us to remove fixed ideas by having open discussion with specialists in different fields at least once a day. In particular, asking questions to PIs from different specialties may present opportunities for learning. And at the same time, it will present opportunities for senior PIs to throw away preconceptions and to think through things from their foundations again.

The advantage this institute has from the personnel aspect is that it is free to employ people from an international viewpoint. It will be good for young researchers to become aware of their international rivals, and this may stimulate their research.

In the future, administrative staff will have to handle international correspondence. A system to support administrative work in English has already been established at NIMS in Tsukuba, and I have heard that the WPI at Tokyo University is also going to adopt the system.

We have nothing equivalent to a so-called faculty council, either. It is also important to reduce the time spent on administrative work to ensure that as much time as possible is spent on research.

This concludes my explanation of the internal operation of the center.

For external operation, the first thing I have in my mind is dissemination of the research results and external evaluation. It is normal to make research results available on the Internet. But it is also important to periodically communicate research activities at this institution to people on the outside through quarterly newsletters, etc. and to facilitate the feedback of information. "Outside" here refers to three parties: universities, the private sector, and the general public. As far as the general public is concerned, there is a trend for students to stay away from science, and we'd like to make cutting edge information available to them, including high schools and liberal arts universities. Aside from deep specialist studies, receiving feedback and questions on aspects of daily life will surely be useful for researchers.

So that we can receive feedback from the outside at any time, the email address and fax number of the WPI office are open to the public. We also welcome direct verbal feedback from actual companies, etc. We want to expand our news editing to avoid one-way communication. We must aim at reforming the development of materials science, while keeping in mind the tendency

of a university to conduct research for the sake of the research itself, and not let our researchers slip into self-complacency.

We ask for your continued support and cooperation.

(Interviewed in the Institute Director's Office of WPI on the Katahira Campus on January 23, 2008.)

by Hiroshi Komatsu

原子分子材料科学高等研究機構（WPI – AIMR）の山本嘉則機構長にきく （Interview with Yoshinori Yamamoto – Japanese version）

2007年12月24日発行の「WPI-AIMR News vol. 1」でこの研究機構の構想と背景、目的、人的構成、共同研究体制などがわかり易く図解されています。材料科学系、物理系、化学系の3つの異専門分野の研究者が共に協力し合って、革新的な材料や新物質を生み出すことが大目標です。30人の主任研究者（PI）をそれぞれ国内外からスカウトし、さらに准教授、助教、ポスドクを募集します。全体で200人ほどの研究者が10年ないし15年にわたって基礎から応用までにまたがり、材料を原子・分子レベルから研究する知能集団になります。本研究機構は世界をリードする独創的な研究成果を挙げ、人類社会に貢献するという高い理想を持っています。

具体的には、材料科学及び材料工学の分野で世界中から注目される卓越した研究成果をあげることが第一の柱です。第二の柱は日本の旧来の閉鎖的な講座制がもっていた負の部分を変え、きちんとしたプロポーザルを出せる若手も独立して自由に研究を展開できるように計られます。日本ではこれまで、若手が待機する時間が長すぎました。最後の柱はコミュニケーションのバリエーション破壊です。国外から参加する研究者も多勢いますので、公用語は英語になります。英語を母国語としない人たちも、broken English でかまいませんので、とにかく英語で物事をすすめます。全員が気後れすることなく、英語でコミュニケーションが出来るようになることは、今後、国際的な飛躍をする上でも必須条件になります。

研究機関内の人的交流は素晴らしい研究成果を達成するために重要なことです。なぜなら、互いの専門を活かしながら共同研究し協力することで融合研究を行い素晴らしい成果へと実を結ぶことが多いからです。新材料、新しいプロセスの発見、システムの開発などには多面的な考え方が組み合わせられることが必要です。「A 専門分野の常識は B 専門分野の非常識」ということは多々あります。将来性豊かな新発見が、常識をはずれたところで生れた例はたくさんあります。たとえばタンパク質の質量測定をするのにレーザーによるイオン化を使うことなどは、タンパク質の壊れ易いことを知っているその道のベテランはまず手を出しません。ところが、レーザーによるタンパク質のイオン化と TOF を組み合わせたのが、その道の新人だった田中耕一さんで、実験結果がノーベル賞のきっかけになっています。

その道の専門家の中には標準的な知識にしばられる余り、思い切った冒険をしない人が多くなっています。飛躍するには常に若いバネが必要です。新人とベテランが上手く組み合せて、大きな成果が出た例は多いです。

本機構では専門の異なる人同士の交流を促進するため、日常的なティータイム、月ごとの討論会、外部の共同研究者とのミニシンポジウムなども推奨しています。大小様々な自由な討論を元にした研究協力により創造力を飛躍させたいです。

1日に1回は異分野の専門家と自由討論して、頭の中の枠をはずすようなこともできればよいと思います。特に異専門のPIに質問をぶつけることは、自分の勉強になると同時に、先輩のPIにとっても、ものごとを先入観なしで再び根本から考え直すチャンスになることもあります。

本機構の人事面のメリットは、かなり自由に国際的な見地から人を採用できることです。若手も良い意味で国際的なライバルを意識するようになり、研究のよい刺激になるでしょう。

これからは事務の方も国際対応ができることが望まれます。つくばのNIMSでは既に英語による事務支援体制ができていますし、東京大学のWPIもその体制をとるようにすると聞きました。

いわゆる教授会に相当するものもありません。事務的な時間をすくなくし、研究する時間が出来るだけ潰れないように計らうことも大切です。

以上、内部の運営についてお話ししました。

外部に関しては、研究成果の伝達や外部評価がまず思い浮かびます。研究成果をネットで見ることができるようにすることは当然ですが、季刊ニュースなどで定期的に本機構の研究活動状況を外部に伝え、情報のフィードバックを円滑にすることも大切です。外部とは「大学、企業、および一般」の3者を指します。「一般」については理科離れが出ている現在、高校や文系の大学までも含めて、最先端の情報を送りたいです。専門を深く追求することはもちろんですが、同時に、日常生活の視点からコメントや質問をもらうことも研究者にとって有用になるはずです。

外部からの反響をいつでも受信できるように、WPI オフィスのメールアドレスとファックス番号を公開します。企業などの現場の声が素直にはいってくることも歓迎します。一方通行にならないようにニュースの編集も工夫したいです。ともすれば研究のための研究となり、自己満足に陥りやすい大学の傾向を、常に意識して材料科学の革新的発展を目指すように心がけます。

皆様のご声援・ご支援をお願いします。

(2008年1月23日 片平キャンパス WPI 機構長室にてインタビュー)

小松 ^{ひろし} 啓 記



Prof. Masashi KAWASAKI

主任研究者 川崎 雅司

Interview with Professor Masashi Kawasaki, Principal Investigator , WPI-AIMR

Personal History, Encounter and Breakthrough

—Three pillars: chemistry, solid state physics and electronics—

An epoch-making research achievement by Professor Masashi Kawasaki of the Institute of Materials Research at Tohoku University was released across Japan on Valentine's Day in 2005. It was presented under the title “A visionary light opens into the future—Impactful light-emitting diode” on an infotainment program by NHK (Japan Broadcasting Corporation), “Today's Close-Up.” The light-emitting diode (LED) that was the subject of the program was developed using zinc oxide and gives out ultraviolet radiation. This ultraviolet light-emitting diode is said to be leading the illumination revolution. Differing from its predecessor, the blue-light-emitting diode based on GaN, the material for the new diode is found in abundance in the environment around us and thus can be obtained at a low cost. Moreover, the LED has very low energy consumption and is expected to have a semi-permanent life.

What brought about this world-leading research result, and what developments can be expected from it? We asked Professor Kawasaki directly.

Readers will be interested to hear about the professor's life history, and this may enable us to see the motivations behind his research activities. Of course he was gifted with the intuition needed to be a leading researcher, but at the same time it seems that his vigorous and unique attitude which is characterized by a fearlessness and a tendency to push down the boundaries comes from the success that he experienced at an early stage in his research career. His background reveals that since that time, he has maintained a proactive stance toward challenges, and has been fortunate enough to have good instructors that encouraged him to establish his own original procedures through actual experience. What is more, within his own realm of expertise, he attempted to engage in joint research with top-level researchers in different fields. I hope that you can see what lies behind his distinguished career, including the various painstaking efforts and attempts he made that led to his successes.

Now let's listen to Professor Kawasaki's story.

“I encountered the energy crisis or so-called “Oil Shock” when I was an elementary

schoolboy. This was the original experience that made me concerned about energy issues. When I was a junior high school student, I read “Suiso Enerugi (Hydrogen Energy)” (*Blue Backs*, Kodansha Ltd.) written by Professor Tokio Ohta of Yokohama National University and began to form the desire to be a researcher who fights against future energy crises. In my high school days, I read a lot of books published by Simul Press Inc. that published books with shocking titles like “Netsuosenn (Thermal Pollution),” and began to think more and more about the mission of scientists including energy issues. At the time, global warming had not emerged as a topic, but I naturally understood that once we had burned up all the oil and fossil fuels, the Earth would revert to the climate that existed at the time those fuels were being stored. When I had to decide my future career, I wrote to Professor Ohta to ask for advice on which university I should attend in order to study hydrogen energy. He told me that I could choose Yokohama National University; at this time Professor Kenichi Honda of the Faculty of Engineering at the University of Tokyo was conducting active research. I entered the Science I of the University of Tokyo in 1980 and found out that the scores in the exams at the College of Arts and Science, Junior Division required to enter the Department of Industrial Chemistry were not high, because not many students wanted to get into the Department. So I devoted myself to training both body and spirit by playing American Football and learning about society through after-school jobs in liquor shops. I went on to the Department of Industrial Chemistry in the Faculty of Engineering, where I actually visited laboratories and joined the laboratory of Professor Kazuo Fueki who had been studying hydrogen energy.

In the summer of my fourth year, when I gave a presentation at one of the laboratory’s seminars on the theme of my undergraduate thesis and what I had found out about the future of hydrogen energy, then associate professor of the Fueki Laboratory, Dr. Hideomi Koinuma, provoked me by saying, “Hydrogen energy has no future. Instead, you had better study the amorphous silicon cell.” Docile as I was, I thought he was right after listening to his account in detail and decided to commit myself to Dr. Koinuma for my postgraduate studies.

That was the time of new materials, with high hopes for amorphous silicon and many companies entering the market. For Japan, which has no crude oil resources, an energy policy directly linked to the survival of the state has always been a central issue, and government projects on photovoltaic power generation such as the Sunshine Project were just being launched. Amorphous silicon, in particular, had attracted people’s attention for thin film transistors for displays as well as for use in solar cells. Spin-off research from this currently contributes to Japan’s technical competitiveness and trade balance with the development of large screen televisions. At the time, however, I had many opportunities to listen to young researchers giving presentations at technical exhibitions on liquid crystal displays full of defects. This allowed me to learn about the future and diversity of materials research from a wide point of view.

By the way, Dr. Koinuma, my postgraduate instructor, requested his students to ask questions in a conference. My first experience of an academic conference was when I attended a

session on amorphous silicon at the Japan Society of Applied Physics. In the session, an engineer from a company was giving a presentation on the characteristics of amorphous silicon created by silicon electrolysis (anodic oxidation). Since I knew nothing about it, I plucked up the courage to ask him what “anodic oxidation” meant. The researcher fobbed me off, saying, “The technique has been around for many years.” Just as I was feeling embarrassed and frustrated, the chairman, Dr. Kuwano (later president of SANYO Electric Co., Ltd.), said to him, “Since it appeared sometime around the time the young man asking the question was born, he asked because he did not know. Would you kindly answer his question in full?” I was saved by those words. I continued to feel deeply that it is important to answer questions even after I became an expert. Dr. Kuwano is the person who commercialized amorphous silicon solar cells for use in devices such as electronic calculators. I always keep in mind that I will attract ambitious young people if I respect that kind of free-wheeling atmosphere.

At that time, we were making amorphous silicon by decomposing silane by discharging ultraviolet rays or plasma. Silane is a gas generated by combining silicon and hydrogen. Inspired by Dr. Junichi Nishizawa’s method to control reactions by light, I considered that repeatedly and alternately discharging ultraviolet light and plasma in silane and methane made from a combination of carbon and hydrogen would generate two substances; the reaction initiated by the light would decompose silane into amorphous silicon, while the reaction initiated by the plasma would decompose the methane as well into an amorphous semiconductor in which silicon and carbon are mixed (silicon carbide). I noticed that by using this, a new superlattice of amorphous silicon and silicon carbide could be generated. “Amorphous” indicates that the atoms do not show a regular alignment, but I created a structure in which irregularly-aligned atoms were forced into regular alignment using nanoscale technology. Dr. Reona Ezaki proposed this concept for crystal semiconductors and named it a “superlattice,” while I adopted the concept of the superlattice for noncrystal substances and achieved it chemically. I published the results in the journal *Nature*, and later developed them in my doctoral thesis [*Nature* Vol. 331, 153-155 (1998)].

In 1986, when I was continuing with my studies and had established the general direction of my thesis, an unexpected and life-changing event happened to me. An IBM researcher in Switzerland discovered high-temperature superconductivity in oxide ceramics made mainly of copper. A large number of scientists rushed into research related to the discovery. I have unconsciously acquired the habit of being a top runner in major trends, and experienced both the joys and severity of global cutting-edge research while leading a fairly busy life working day and night in the frontiers of research at the Koinuma Laboratory. I gradually became fascinated by the Bell Laboratory and IBM Laboratory, the key places for superconductivity studies, and developed the desire to study abroad to try out my skills.

Thanks to an introduction by Dr. Koichi Kitazawa, then associate professor at the Fueki Laboratory, I was fortunate enough to be accepted by Dr. Praveen Chaudhari (a senior of Dr.

Kitazawa's in his MIT days) at the IBM Watson Research Center. Conversant in both chemistry and solid physics, Dr. Kitazawa was a prominent figure in studies into a new material physics called ceramics super conductivity. I vaguely began to think that this combination of chemistry and solid physics had already been covered by him and that I would thus place myself on the borders of chemistry and electronics. After taking a doctorate, I spent several months at the Hitachi Laboratory where I learned things that were a bit different from what I had learned so far, such as writing patents for electronic devices and how to use clean rooms. In the high-thermal conductivity group at IBM, I succeeded in developing an ultrasensitive magnetic sensor called SQUID. I also studied the physics of superconductive devices intensively for two years, freely handling the top-in-the-world device that I had developed myself.

Immediately after I returned home (1991), a new major project called "PRESTO (Precursory Research for Embryonic Science and Technology)" was launched by the young technology project group under the umbrella of the Science and Technology Agency. I applied for the project with my proposal for emitting light from a high-temperature superconductor, and was selected as a member of the inaugural staff. I participated in the "light & material" project led by Dr. Kenichi Honda and again had an important encounter.

One of the members in the project, who was then a young researcher at Mitsubishi Electric Corporation, developed a theory predicting that the non-linear effect caused by excitons would become extremely great due to the interference effect when the thickness of the thin film and the wavelength of the light were arranged in a certain relationship. In order to verify this through experiment, young researchers of the "PRESTO" gathered and negotiated with Dr. Honda, the general manager. As a result, it was decided that we would select ZnO as the material, buy a new device for my laboratory to make thin films, and then Dr. Yuzaburo Segawa of RIKEN would make an optical assessment. In the course of the experiment, by chance we discovered ultraviolet laser oscillations at room temperature. [Proc. 23rd International Conference on the Physics of Semiconductors, 1453-1456 (1996)]. Light was emitted, not from a superconductor but from ZnO, a white powder used in cosmetics. In the "PRESTO" there was a climate of respecting unexpected achievements more than promised ones, and so I preserved my pride even though I could not keep my promise.

Immediately after our discovery, efforts to develop a light emitting diode (LED) by combining n-type ZnO, which is negatively charged, with p-type ZnO, which is positively charged, became active all over the world. While many dubious theses announced that they had succeeded in making p-type ZnO, no one in the world was able to make an LED using ZnO. We were also involved in painstaking efforts. The breakthrough was an idea based on chemistry to challenge how far we could weaken the n-type instead of adding, without any firm conviction, additives that appear to turn ZnO into p-type. ZnO naturally tends to turn into n-type. We succeeded in making the first p-type ZnO in the world through a procedure to emit ultraviolet light from a pn-joint LED. This was

announced in December 2004 [*Nature Materials* Vol. 4, 42-46 (2005)]. Eight years had passed from the discovery of the ZnO laser, where we succeeded in synthesizing genuine and authentic p-type ZnO, to creating the LED. This achievement was presented later in an NHK's special program of "Today's Close-up."

The thesis in *Nature Materials* that introduced this success with the LED was ranked first in the world in the materials & science field as the most frequently cited paper in the subsequent two years. As a result of this, the reports on p-type ZnO that had been published before virtually disappeared. Now, we are working jointly with businesses on studying applications for the LED based on ZnO.

Compared with GaN, which uses materials that exist only in certain areas of China and some other countries, ZnO is superior in that it can be obtained easily in any country. Moreover, the GaN is made via a special buffer layer using a sapphire substrate, since the GaN crystal substrate cannot be synthesized easily. Differing from GaN, the process can be simplified for ZnO since a large single-crystal substrate can be made easily. Since a substrate made of ZnO, unlike a sapphire substrate, allows electricity to flow, it does not have the weak point of GaN, which does not allow electric poles to be created on the surface or reverse side of the LED.

I have just completed the basic research on the ZnO-based LED and am looking for my next target. I have a dream to expand the potential of oxidative products. The textbooks say that the mobility of the electrons in ZnO is approximately $200 \text{ cm}^2/\text{Vs}$, but when I investigated the nature of pure ZnO, I found that the mobility of the electrons in ZnO is approximately $500 \text{ cm}^2/\text{Vs}$. So I confined the n-type ZnO electrons in a very thin space to generate a secondary electron gas and measured the Hall resistance. As a result, I succeeded in monitoring the quantum Hall effect, a macro quantum effect [*Science* 315, 1338 (2007)]. This is the first macro quantum effect in oxidative products found besides superconductivity. I am glad that oxidative products have at last reached this stage. In the background to this success lies the over ten years of joint research with Professor Hideo Ohno of the Research Institute of Electrical Communication at Tohoku University on transparent transistors and transparent ferromagnetic materials. I always feel stimulated when I talk about my research with Professor Ohno, who is an expert in electronics. However, I am not so interested in orthodox semiconductors. What attract me are non-orthodox things that do not attract other researchers, such as amorphous and oxidative products. I also discovered that adding a little bit of magnetic impurity to oxidized titanium would turn the semiconductor into a magnet [*Science* 291,845 (2001)], which I believe is an important achievement that clearly indicates a bright future for oxidative products. I now harbor the desire to contribute to bringing about an energy-saving, energy-creating and environmentally harmonized society by further expanding the range of my research targets and discovering new functional devices for strongly-correlated electronic oxidative products related to high-temperature superconductivity.

The motivating force driving this research is, above all, our unique procedure for

synthesizing oxide thin films. In fact, the synthesization procedure for amorphous superlattices during my university days and the procedure for the later p-type ZnO are based on almost the same concept. I control ZnO at the atomic level; to be more intuitive, I design processes while thinking seriously from the viewpoint of the atom how I wish to freeze the solid. Nevertheless, it is not easy to find out the optimum conditions, and we have to search for the conditions on a “carpet-bombing” basis when dealing with non-orthodox materials such as oxidative products. Here I have also invented a unique procedure called the “combinatorial method” to synthesize 100 to 10000 different samples in one experiment. I wish to add a modern touch to “manufacturing,” which is the essence of chemistry, and use my unique skills to make further discoveries one after another. My future target is to study how the three attributes of the electron (electrical charge, spin and orbit) behave and create a paradigm for a new materials science via functional development using the new mutual relationship between their impacts and responses (cross-correlation).

(Interviewed by Hiroshi Komatsu, in Professor Kawasaki’s office at the Institute of Materials Research, Tohoku University, February 8, 2008)

WPI-AIMR PI 川崎雅司教授にきく

(Interview with Professor Masashi Kawasaki – Japanese version)

「生い立ち・出会い・ブレイクスルー」 —化学・固体物理学・電子工学の3本柱—

東北大学金属材料研究所の川崎雅司教授による画期的な研究成果が2005年のバレンタインデーに全国報道された。NHKの「クローズアップ現代」で、「夢の光が未来をひらく～発光ダイオードの衝撃～」と題して。照明の革命を導くとされる紫外光を出す発光ダイオード(LED)を酸化亜鉛(ZnO)で作製したのである。先行の窒化ガリウム(GaN)青色発光ダイオードとは異なり、原材料は身近に大量にあり、安く得られる。しかもLEDのエネルギー消費はごく少なく、寿命も半永久的である。

このような、世界をリードする研究はいかにして生まれたか、そして今後どのように発展するのか。今回、川崎教授から直接お聞きした。

生い立ちからうかがうことで、研究活動の裏にある動きが見え、一般読者の方々も興味を持たれると思います。研究を進める上でのカンの良さには先生の天性もありますが、研究者として育つ初期に巡り会った成功体験を通して、物怖じしなくなり、いらぬ束縛から解放された面もあるように見えます。それ以後は困難に挑戦する姿勢を持ち続け、良い指導者にめぐまれ、実体験から独自の手法を確立してゆく姿が浮き彫りにされます。さらに、自分の得意分野を武器として、異分野の第一級の研究者と共同研究を展開するなど、成功に至るさまざまな苦心や工夫など隠れた部分を感じ取っていただければ幸いです。

では、早速、川崎先生の話をお聞かせください。

小学生の時、エネルギー危機、いわゆる“石油ショック”に出会いました。これがエネルギー問題に関心を持った原体験です。中学生の頃、横浜国立大学の太田時男先生が書かれた「水素エネルギー」(講談社・ブルーバックス)を読んで、将来はエネルギー危機に立ち向かう研究者になりたいと思うようになりました。高校生時代には「熱汚染」などショッキングなタイトルの本を出すサイマル出版の本を数多く読み、ますますエネルギー問題など科学者の使命について考えるようになりました。当時は、地球温暖化など話題にはなっていませんでしたが、石油など化石燃料を燃やし尽くすと、それを蓄えたころの気候に戻ると自然と納得していました。将来の進路を考える頃、太田先生に手紙を出して、水素エネルギーの研究をするにはどの大学へ進学するのが良いかについて助言をいただきました。横浜国大も良いが、東大工学部の本多健一先生が活発な研究を行っていると教えてもらいました。1980年に東大へ入学して色々調べると、当時学科としては人気なかった応用化学への進学には、教養学部での試験で大して点数が必要でないことがわかり、アメフトの部活動や水商売のアルバイトを通じた社会勉強で徹底的に心身を鍛えました。工学部の応用化学へ進学し、実際に研究室を見学して、同じく水素エネルギーについて研究していた笹木和雄先生のところにお世話になることになりました。

大学4年の夏頃、卒業論文研究の構想と水素エネルギーの将来性について調べた内容を研究室のセミナーで発表したところ、笹木先生の助教授であった鯉沼秀臣先生が「水素エネルギーに将来はない、それよりもアモルファスシリコン太陽電池の研究をやるべきだ」と挑発されました。素直な私は、鯉沼先生のお話を詳しくうかがって、「なるほど」と思い、

大学院からは鯉沼先生の指導を頂くことになりました。

当時は新素材ブームで、アモルファスシリコンへの関心が高く、多くの企業が参入していました。原油資源を持たない日本にとって、国家の存続に直結するエネルギー政策は中心的な課題であり、サンシャインプロジェクトなどの太陽光発電に関する国家プロジェクトが推進されている最中でした。特にアモルファスシリコンは、太陽電池だけでなく、ディスプレイ用の薄膜トランジスタとして注目されるようになりました。副産物とも言えるこの研究が、今では大型テレビを可能にして日本の技術競争力と貿易収支に貢献していますが、当時は、欠陥だらけの液晶ディスプレイを若い研究者が技術展で発表するのを勉強して、材料研究の将来性と多様性について広い視野から学べる良い機会でした。

話は変わりますが、大学院で指導を受けた鯉沼先生は、学会では毎日一つは質問をするようにと学生に命じていました。初めて学会に出席したのは、応用物理学会のアモルファスシリコンのセッションでした。そのときのセッションで、ある企業の方がシリコンを電気分解（陽極酸化）して作製したアモルファスシリコンの特性について発表していました。私は何も知らなかったのが、勇気を出して「陽極酸化」はどういうことかと質問をしたところ、もう何年も前からわかっていることだ・・・と、切って捨てるような返答を受けました。とても恥ずかしいような悔しいような気持ちになった瞬間に、座長であった桑野さん（後の三洋電気社長）が『質問した若い人が生れた頃のことで、知らないからこそ質問している。きちんと説明すべきです。』と注意されました。このときは救われました。そして、どんなにえらくなくても質問にはきちんと答えることが大切だと身に沁みて感じました。桑野さんは、電卓などについているアモルファスシリコン太陽電池を事業化した方です。そういう闊達な雰囲気や尊重して、志のある若い人を惹きつけたいと常に思っています。

当時、シリコンが水素と結合してできるシランというガスを紫外線やプラズマ放電で分解してアモルファスシリコンを作っていました。西澤潤一先生の「光で反応を制御する方法」にヒントを得て、シランと炭素が水素と結合したメタンを入れて紫外光とプラズマ放電を交互にくりかえすと、光によって進行する反応ではシランが分解されて、アモルファスシリコンが生じ、プラズマだとメタンも分解してシリコンと炭素が混じったアモルファス半導体（シリコンカーバイド）ができると思いました。これを使えば、アモルファスシリコンとシリコンカーバイドの新しい超格子が作製できることに気づきました。アモルファスというのは原子が規則的に並ばないことを示しているのですが、それを無理矢理ナノスケールで規則的に並べた構造を作ったのです。江崎玲於奈先生が結晶半導体でこの概念を提案され超格子と名付けられましたが、わたしは、結晶でない物質に超格子の概念を取り入れ、化学のセンスでそれを実現したのです。この結果を Nature 誌に発表し、後に博士論文にまとめました [Nature vol.331, 153-155 (1998)]。

研究も進み、博士論文の方向性も見えだした 1986 年に、突如として人生が変わるできごとが起こりました。銅を主成分とする酸化物セラミックスで、スイスの IBM の研究者が高温超伝導を発見したのです。どっと大勢の研究者がその関連研究に流れ込みました。大きな流れの中では、先頭の方に立とうという習性がいつからか身につけていて、鯉沼研の核弾頭として昼も夜もない生活を送りながら世界の最先端研究の楽しさと厳しさを味わいました。当時、超伝導研究のメッカであったアメリカのベル研究所や IBM の研究所に心を惹かれるようになり、留学して腕試しをしてみました。

幸い、笛木研の助教授であった北澤先生の紹介で IBM ワトソン研究所のチャウドリーさん（北澤先生の MIT 時代の先輩）が採用してくれました。北澤先生は、化学と固体物理学の両方に精通しておられ、セラミックス超伝導という新しい材料物理の研究で存在感を持っておられ、何となくこの組み合わせは取られちゃったからわたしは化学と電子工学の境目で勝負しようと考え始めました。博士を取った後、出発までの数ヶ月を日立中研で過ごし、電子デバイスの特許書きやクリーンルームの使い方など、これまでと少し違ったことも教わりました。IBM では、高温超伝導グループで

SQUID という超高感度磁気センサーの開発に成功し、世界最高性能の自作デバイスを突っつき回して2年間ミッチリと超伝導デバイスの物理も勉強しました。

帰国直後(1991年)、科技厅傘下の新技術事業団で“さきがけ研究”という若手が主体で行う新しい大型プロジェクトがスタートし、高温超伝導体から光を出すという提案を応募したところその第1期生に選ばれました。本多健一先生が主宰する「光と物質」プロジェクトに参画し、また新しい出会いに巡り会いました。

そのプロジェクトに参画した当時三菱電機の若手研究者であった理論家が、薄膜の厚さと光の波長をある関係にそろえると干渉効果で励起子による非線形効果が極度に大きくなると予言しました。それを実験で検証しようと“さきがけ研究”の若手が集まり、統括の本多先生に談判して、材料としてZnOを選び、わたしのところに新しい装置を買ってもらって薄膜を作って、理化学研究所の瀬川勇三郎さんが光学評価をすることになりました。実験するうちに、なんと室温での紫外レーザー発振を発見しました [Proc. 23rd International Conference on Physics of Semiconductor, 1453-1456(1996)]。超伝導体ではなく化粧品の白い粉であるZnOから光を出したわけですが、“さきがけ研究”では約束通りの成果より思いもかけない成果を大切にする風土があり、約束を守れなかった割には偉そうにしていたと思います。

その直後からマイナスの性質を持つn型とプラスの性質を持つp型のZnOを組み合わせて発光ダイオード(LED)を作る研究が世界中で活発に展開され、p型化に成功したと主張するあやしげな論文は多数発表されるものの、世界中の誰もZnOでLEDが作れませんでした。われわれも大変苦労をしました。突破口は、天然にn型になりやすいZnOに闇雲にp型になりそうな添加物を加えるのではなく、n型の性質をどこまで弱めることができるかに挑戦しようという化学の発想でした。レーザーを使う新しいエピタキシー法で、世界ではじめてきちんとしたp型ZnO作りに成功し、pn接合のLEDから紫外光を出すことに成功し、2004年12月に発表しました。[Nature Materials vol.4, 42-46(2005)]。ZnOレーザーの発見から8年かけて真正正銘のp型ZnOの合成に成功しLEDを作成したのです。この成果が後にNHKのクローズアップ現代の特別番組として紹介されました。

このLEDの成功を伝えたNature Materialsの論文は、以後2年間の引用度数が多いホットペーパーとして材料科学分野の世界ナンバーワンになりました。これにより、それ以前に発表されていたp型ZnOの報告は事実上消えてしまうことになりました。現在、企業と共同でZnOのLEDの実用化研究をすすめています。

中国など一部の国に偏在した素材を使うGaNに比べ、ZnOはどの国でも簡単に得られる点ですぐれています。さらに、GaN結晶基板が簡単には合成できないためにサファイア基板を使って特殊なバッファ層を介して作るGaNと違って、ZnOは単結晶の大型基板が簡単に作れるためにプロセスが単純化されます。またZnOの基板はサファイアとは異なり電気が流れるため、LEDの表と裏で電極が取れないGaNの弱点もありません。

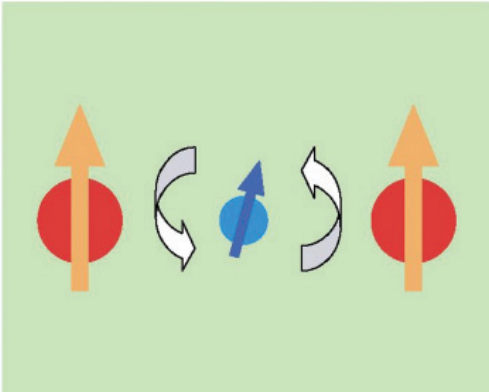
ZnOのLEDに関する基礎研究が終ったところで、今は次のターゲットを探しています。酸化物の可能性を拡げることにも夢をもっています。ZnOは電子の移動度が $200\text{cm}^2/\text{Vs}$ ぐらいと教科書に書いてありましたが、p型をつくる研究の途中で純粋なZnOの性質を丹念に調べたところ、電子の移動度が $500\text{cm}^2/\text{Vs}$ ぐらいあることがわかりました。そこで、n型ZnOの電子を非常に薄い空間に閉じこめた二次電子ガスを作製し、そのホール抵抗をしらべた結果、マクロな量子効果である量子ホール効果の観測に成功しました [Science 315, 1338 (2007)]。これは超伝導以外で見つかった、酸化物における最初のマクロな量子効果です。酸化物もいよいよここまで来たという感想です。この成功の背景には、東北大学通研の大野英男先生との10年来の透明トランジスタや透明強磁性体に関する共同研究がありました。電子工学がご専門の大野先生と研究の相談をするといつも刺激を受けるのですが、わたしは由緒正しい半導体には興味がなく、アモルファスだとか酸化物だとか、いわゆるゲテモノにしか興味がありません。酸化チタンに少し磁性不純物を加えることで半導体が磁石になることも発見しましたが [Science 291, 845 (2001)]、酸化物の明るい未来を明示する貴重な成果だと

思っています。これからは、さらに研究対象を広げて、高温超伝導体に関連する強相関電子酸化物でも新しい機能デバイスを発見して、省エネルギーやエネルギー創出・環境調和型の社会に貢献したいと夢を膨らませているところです。

この研究を推進する原動力は、なんと言っても独自の酸化物薄膜合成手法です。学生時代のアモルファス超格子と後の p 型 ZnO の合成方法は、実はコンセプトがほとんど一致しています。原子のレベルで制御して、もっと直感的には、自分が原子になった気持ちでどう固体として凍りつきたいか、真剣に考えてプロセスを設計しています。とは言え、最適な条件を見つけ出すのは簡単ではありませんし、酸化物というゲテモノが相手では、それこそ絨毯爆撃的に条件を洗い出すことになります。ここでも独自手法をあみだして、100 ~ 10000 個ぐらいの異なる試料を一度の実験で合成する手法、「コンビナトリアル法」を実現しています。化学の神髄である「ものづくり」を現代風に味付けして、独自技術で次々に新しい発見をなすとげたいと思っています。今後の対象は、光・電圧・磁界などの環境下で、電子の電荷・スピン・軌道といった三つの属性がどう振る舞うかを調べ、その相互の新しい刺激と応答の関係（交差相関）を活用した機能開発を通じて新しい物質科学のパラダイムを構築したいと思っています。

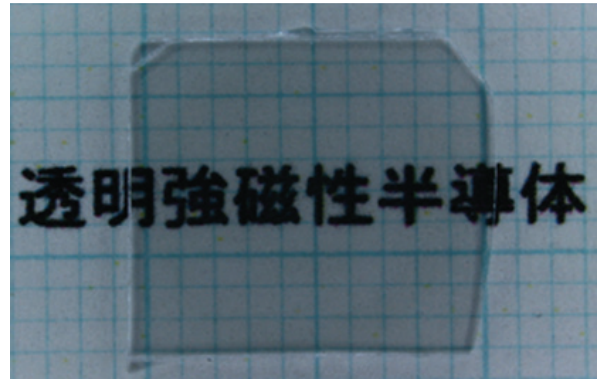
(2008 年 2 月 8 日 東北大学金研川崎教授室にて 小松 啓 記)

Spin



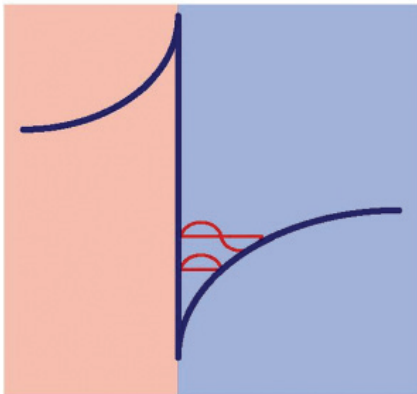
Transparent Magnet Memory
(透明磁石透明メモリ)

$T_c > 400\text{K}$ (TiCo)O₂

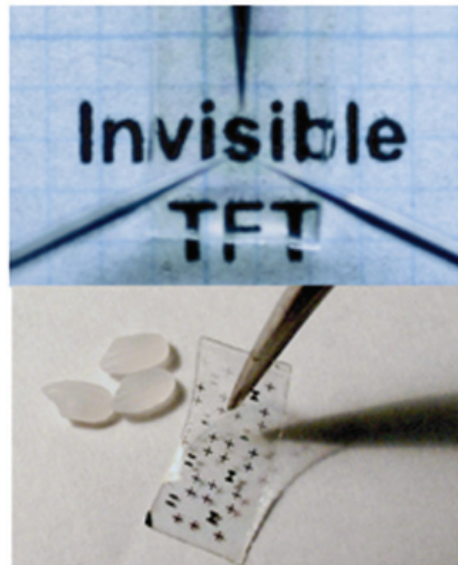


Science 2001
Nature Mater. 2004

Electron

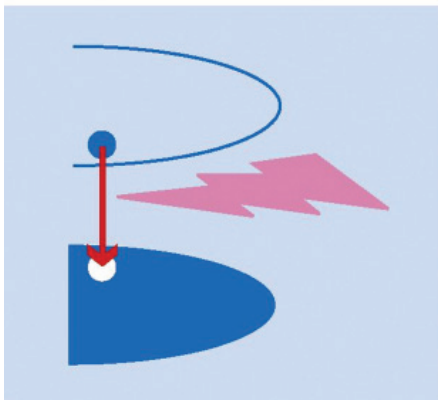


Transparent Transistors, Circuit
(透明トランジスタ透明電子回路)

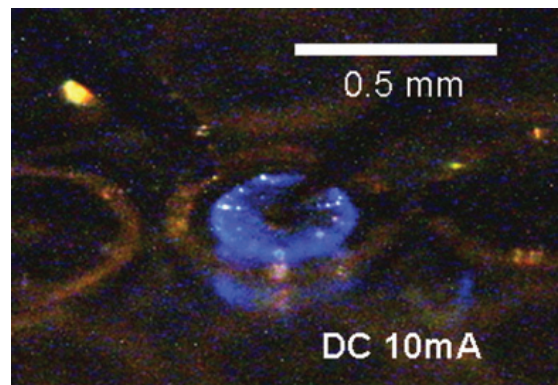


Adv. Mat. 2004
Science 2007

Photon



ZnO Ultraviolet LED, laser
(酸化亜鉛 LED 紫外レーザー)



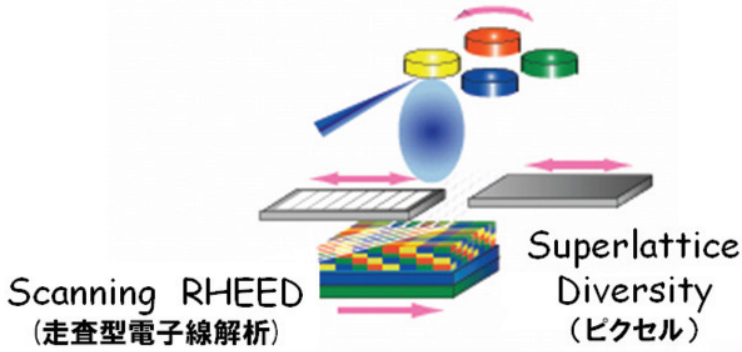
Nature Mater. 2005

Combinatorial Lattice Engineering: Integrated Scheme

コンビナトリアル固体化学：薄膜集積化のスキーム

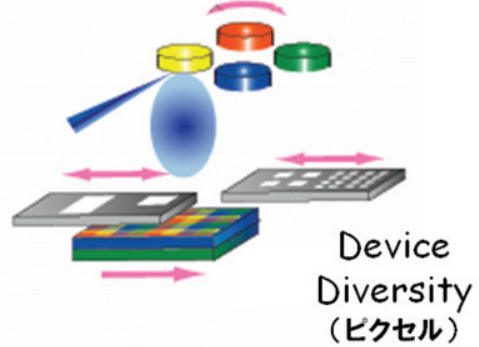
Superlattice Integration

(超格子パラレル集積化)



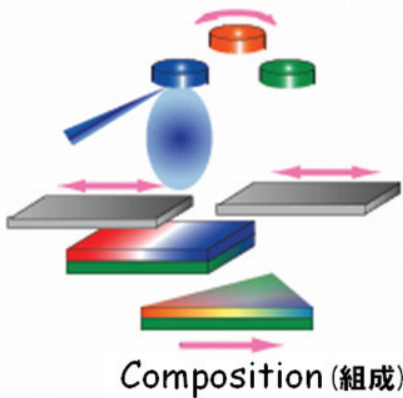
Device Integration

(デバイス構造集積化)



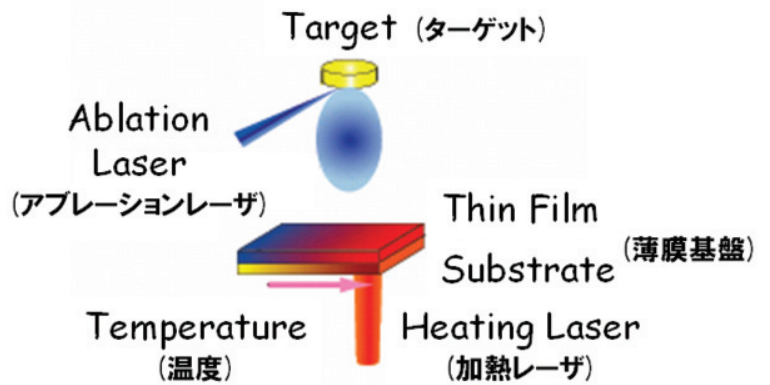
Composition Spread

(組成傾斜)



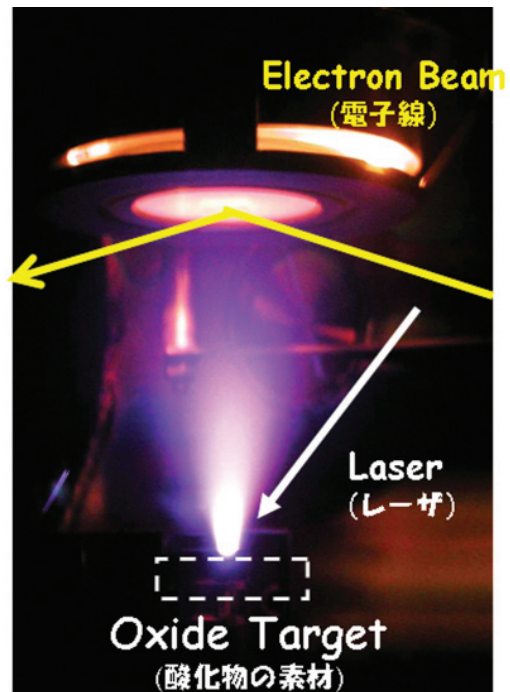
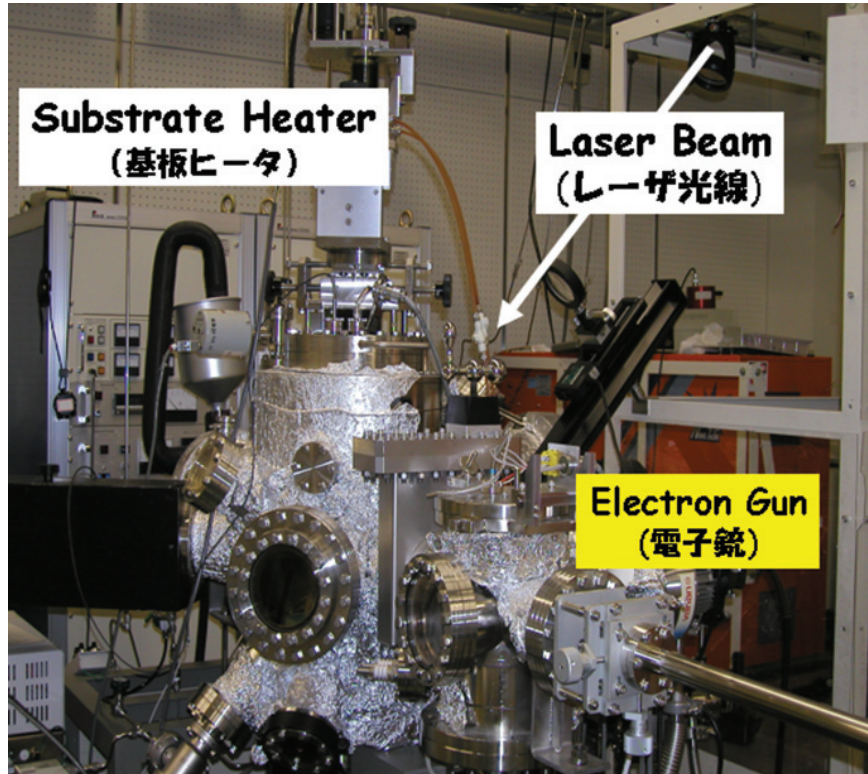
Temperature Gradient

(合成温度傾斜)



Evaporate Oxides by Laser Pulses

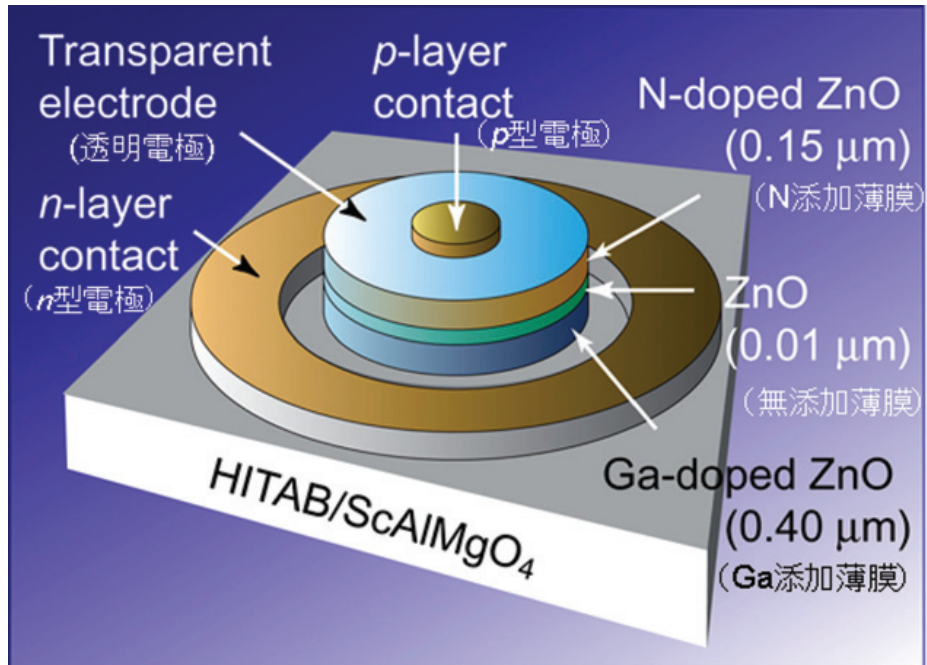
レーザで酸化物を蒸発して薄膜を作る



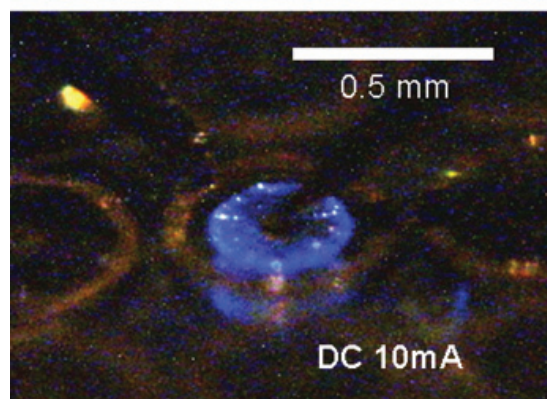
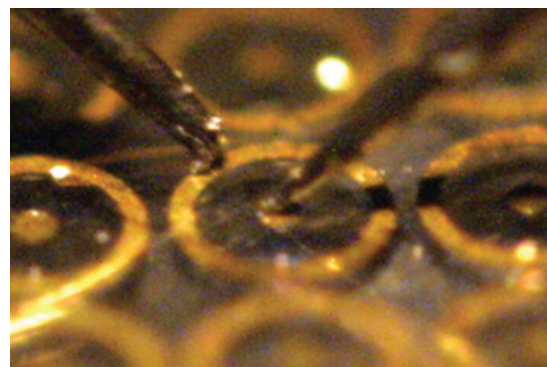
Pulsed Laser Deposition: PLD

Blue Light-Emitting Diodes Based on ZnO

(初めて酸化亜鉛 pn 接合が電流で光いました)

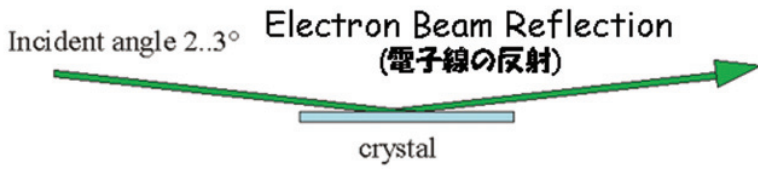


Tsukazaki et al.
Jpn. J. Appl. Phys. (2005)

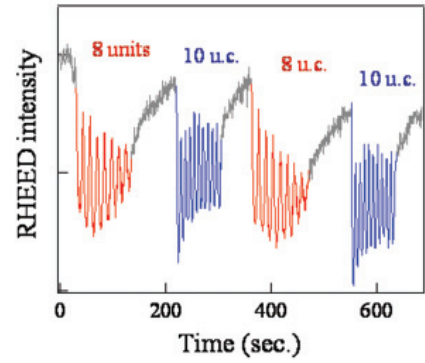
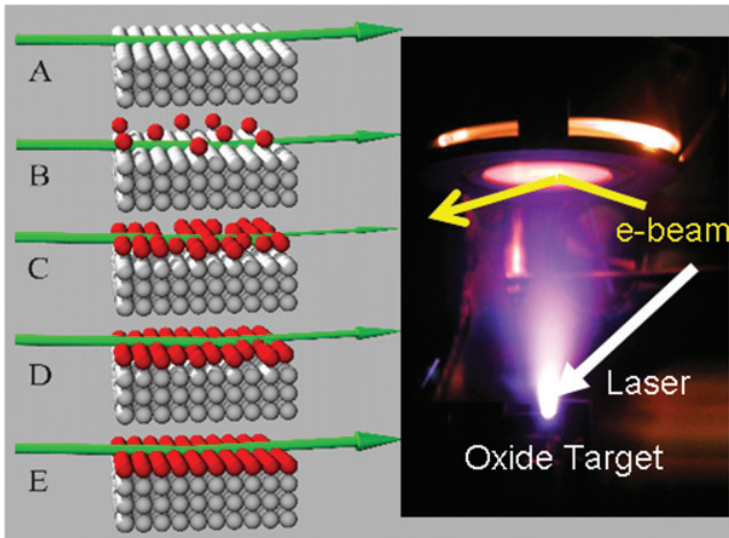
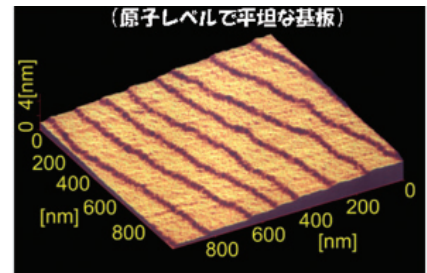


Atomically Controlled Oxide Epitaxy

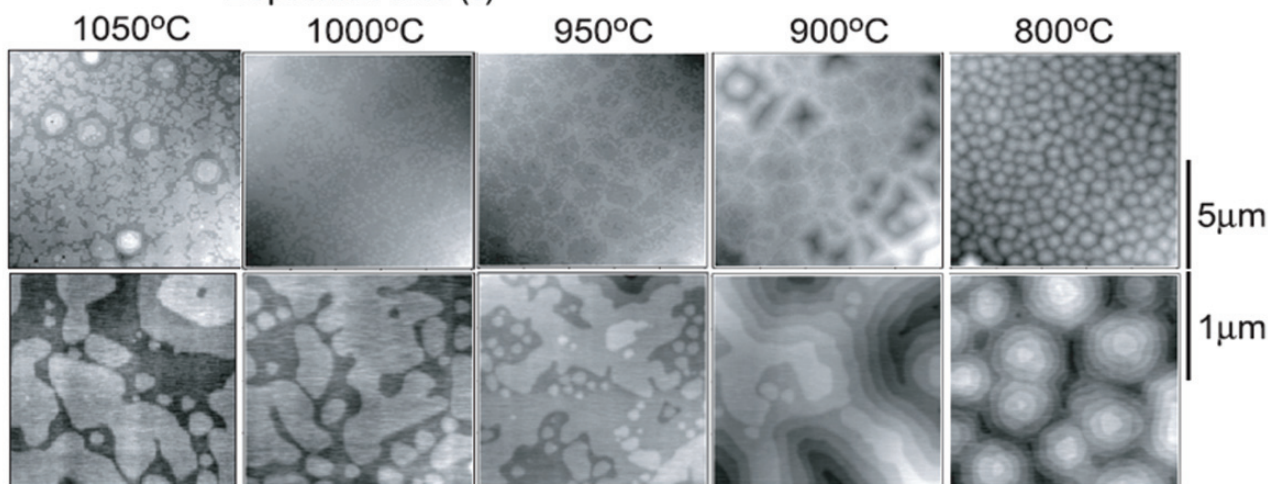
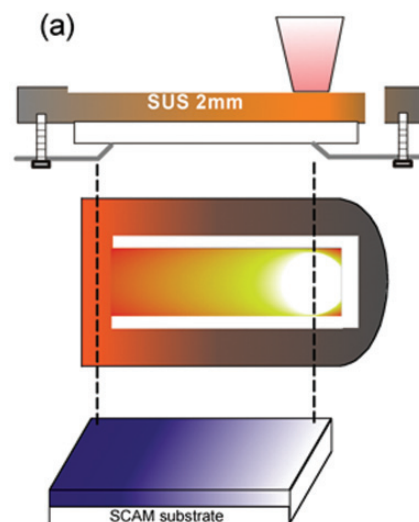
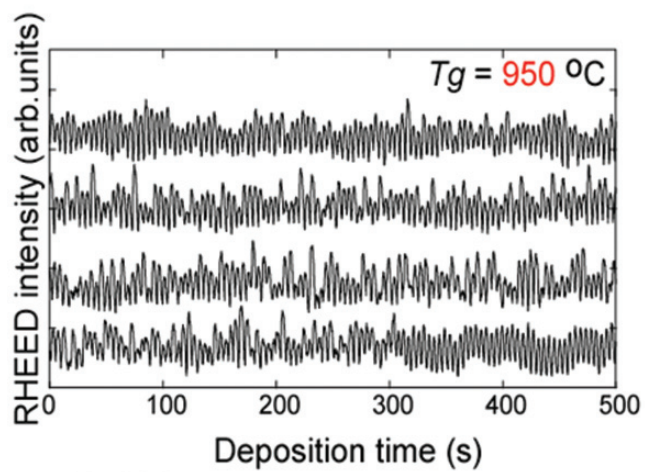
(酸化物エレクトロニクス用のフレクスルエピタキシーの精密化)



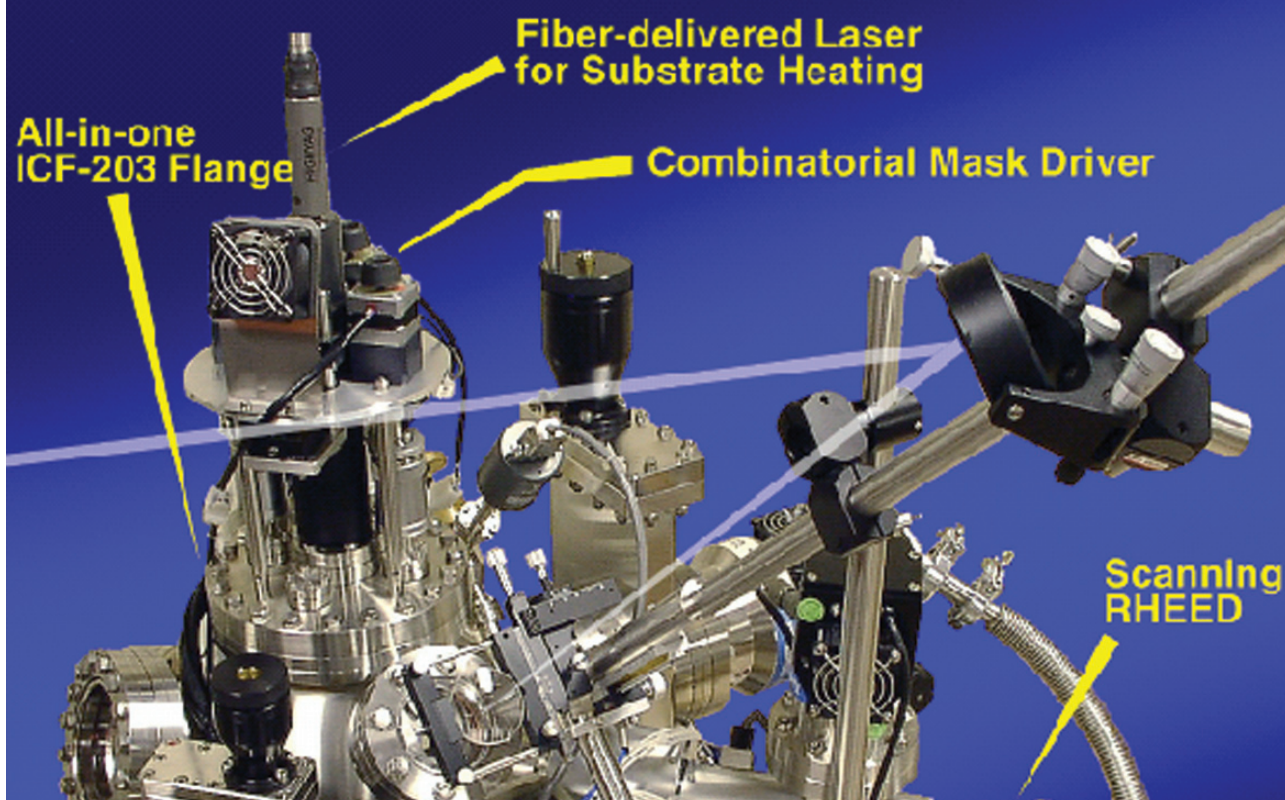
Flat Surface of Oxide



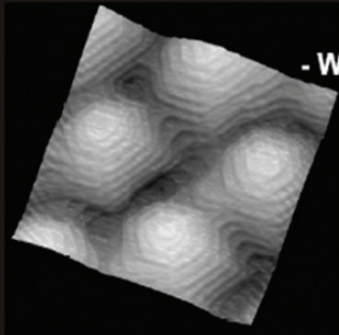
Temperature Gradient Epitaxy (温度傾斜法で楽々最適化)



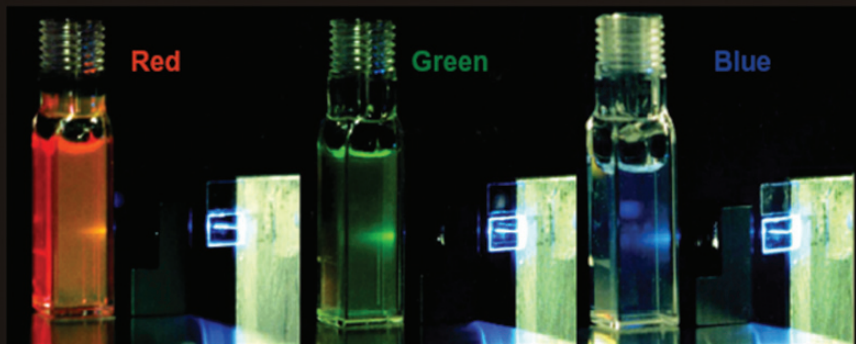
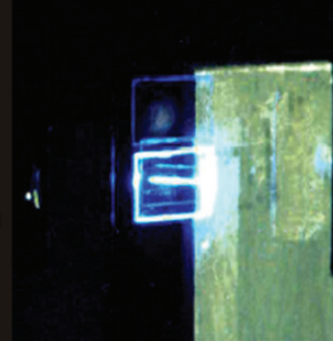
Mobile Combi-PLD



Room Temperature UV Lasing from ZnO



- Widegap Oxide Semiconductor
- Very Large Exciton Binding Energy
- Honeycomb Structure
- Excitonic Recombination
- Very Low threshold
- Natural Cavity



特許登録2996928号(1999)、USP6,057,561(2000)

HKUST and TIT (1996)

Announcement

Junior Faculty/Post-doctoral Positions

Tohoku University WPI-AIMR

Effective October 1, 2007, Tohoku University created a new Research Institute, the Advanced Institute for Materials Research (AIMR), based on an initiative of the Japanese Department of Education (MEXT) for World Premier International Research Center Initiative (WPI) to bring together scientists involved in research on nano-science and technology.

In the 21st century, material science, broadly defined as the study of how complex/novel properties arise in matters/materials from the interactions of individual components, will comprise of inter-discipline collaboration.

([HTTP://WWW.WPI-AIMR.TOHOKU.AC.JP](http://www.wpi-aimr.tohoku.ac.jp)).

Over the next few years, as many as one hundred new appointments at the levels of post-doctoral fellows and junior faculty will be available. All innovative researchers are welcome as active promoters of basic/applied sciences in the fields of physical metallurgy, physics, chemistry, precision mechanical engineering and electronic / informational engineering.

We are continuously looking for excellent applicants throughout the year.

Please submit

- 1) a curriculum vitae,
- 2) research proposal (<3,000 words),
- 3) summary of previous research accomplishments (<2,000 words),
- 4) copies of 5 significant publications, and
- 5) 2 letters of recommendation

by email to yoshi@mail.tains.tohoku.ac.jp,

sakurai@imr.tohoku.ac.jp, and

wpi-office@bureau.tohoku.ac.jp.

All files must be submitted electronically in pdf or Word format.

Applications from, or nominations of, women and minority candidates are encouraged.

Tohoku University WPI-AIMR is an affirmative action / equal opportunity employer

Graduate Student scholarship In Materials Science/Engineering

WPI-AIMR Graduate Student scholarship

Effective October 1, 2007, Tohoku University created a new Research Institute, the Advanced Institute for Materials Research (AIMR), based on an initiative of the Japanese Department of Education (MEXT) for World Premier International Research Center Initiative (WPI) to bring together scientists involved in research on nano-science and technology.

In the 21st century, material science, broadly defined as the study of how complex/novel properties arise in matters/materials from the interactions of individual components, will become an essential and most important research topic

([HTTP://WWW.WPI-AIMR.TOHOKU.AC.JP](http://www.wpi-aimr.tohoku.ac.jp)).

TU WPI-AIMR is now looking for young motivated Ph.D. graduate student candidates in the fields of physical metallurgy, physics, chemistry, mechanical engineering and electronic / informational technology. All innovative M. S. students are welcome as active promoters of basic/ applied sciences in these fields.

Applications are continuously screened throughout the year.

Please submit

- 1) a curriculum vitae,
- 2) research proposal (<1,000 words),
- 3) 2 letters of recommendation,

by email to

yoshi@mail.tains.tohoku.ac.jp,
sakurai@imr.tohoku.ac.jp, and
wpi-office@bureau.tohoku.ac.jp.

All files must be submitted electronically in pdf or Word format.

WPI-AIMR Workshop Guideline

Tohoku University's new Research Institute, the Advanced Institute for Materials Research (WPI-AIMR) solicits several applications per year for International Workshops in the field of "broadly defined Materials Science."

Guidelines:

1) Organizers

Qualified research staff of academic institutions and public or private research establishments can submit the application for an international workshop to be held at WPI-AIMR or its Satellite branches, jointly with the WPI-AIMR principal investigator(s) whose research interest overlaps with the scope of the workshop.

2) Financial support

Under normal circumstances, WPI-IMR supports up to 2/3 of the workshop budget, while the organizer is expected to cover the rest.

3) deadline

The application must be received at least four months in advance to

yoshi@mail.tains.tohoku.ac.jp,

sakurai@imr.tohoku.ac.jp, and

wpi-office@bureau.tohoku.ac.jp.

All files must be submitted electronically in pdf or Word format.

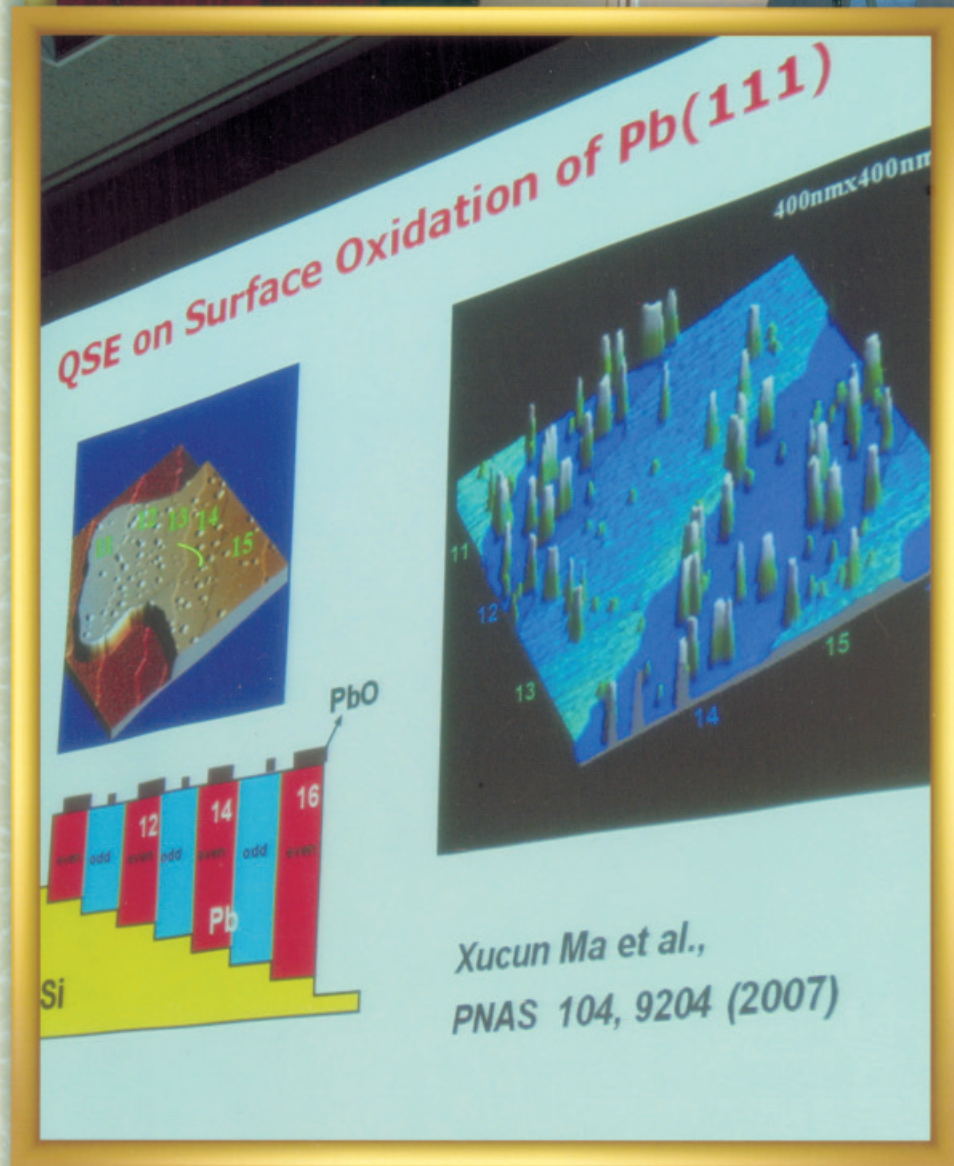
Appendix

WPI & IFCAM Joint Workshop snapshots









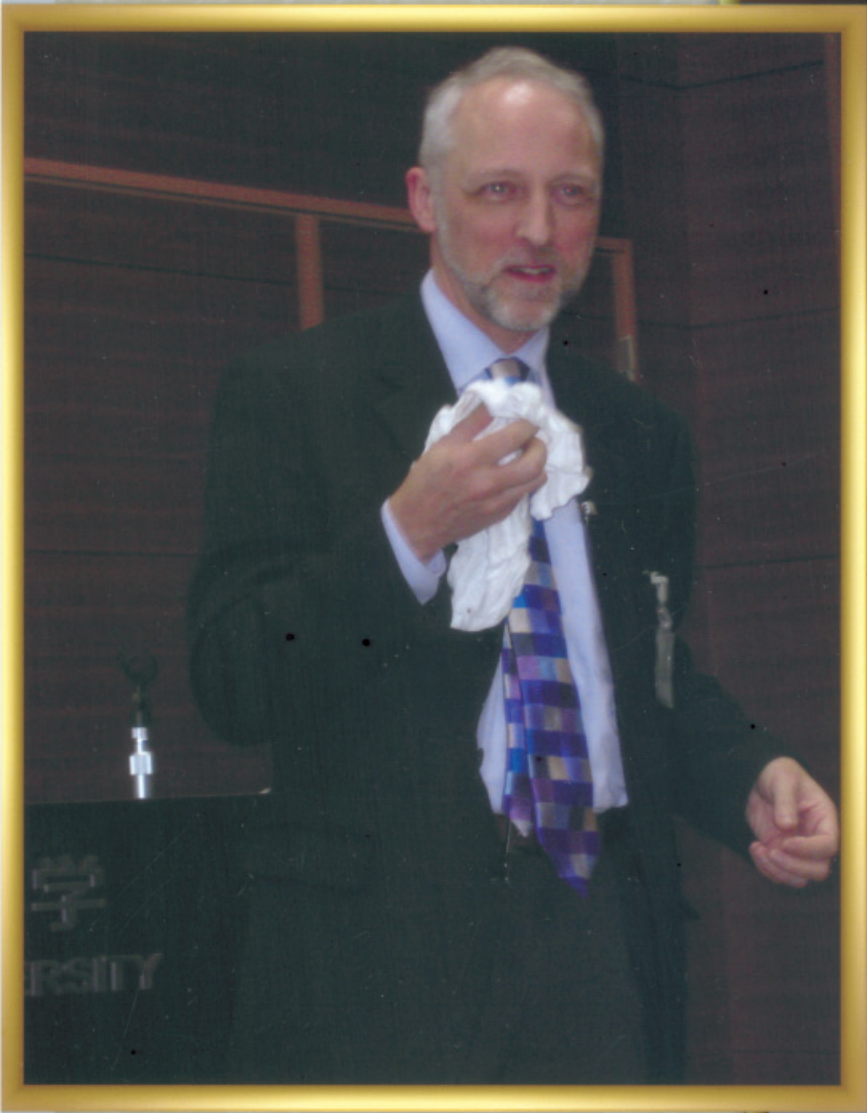








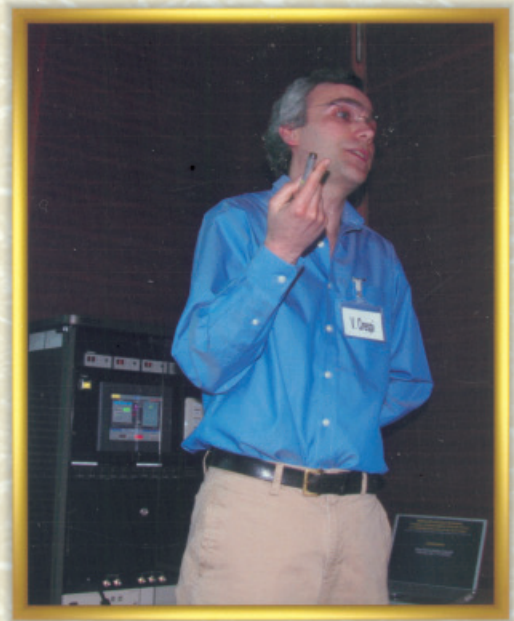












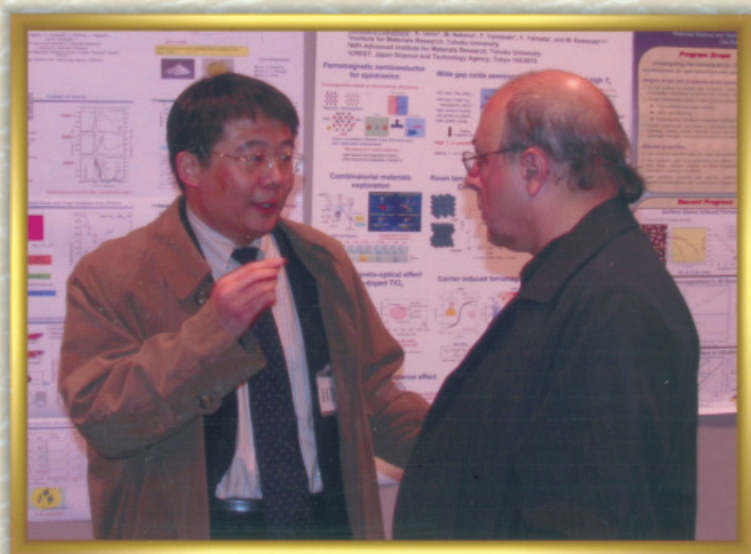






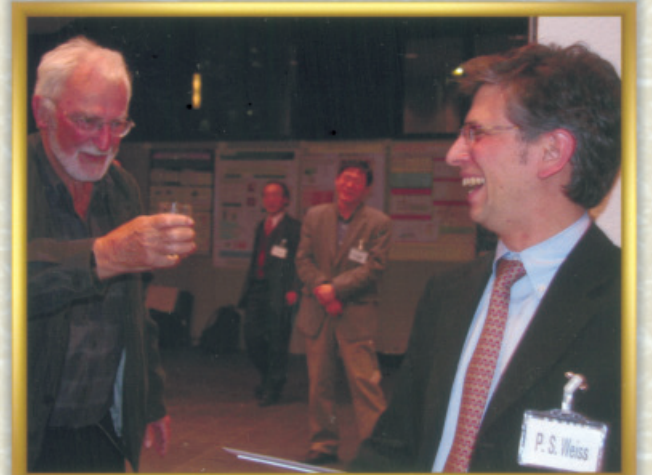
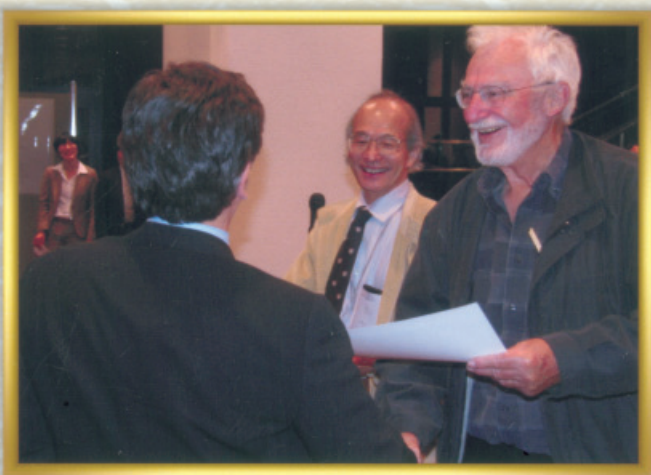


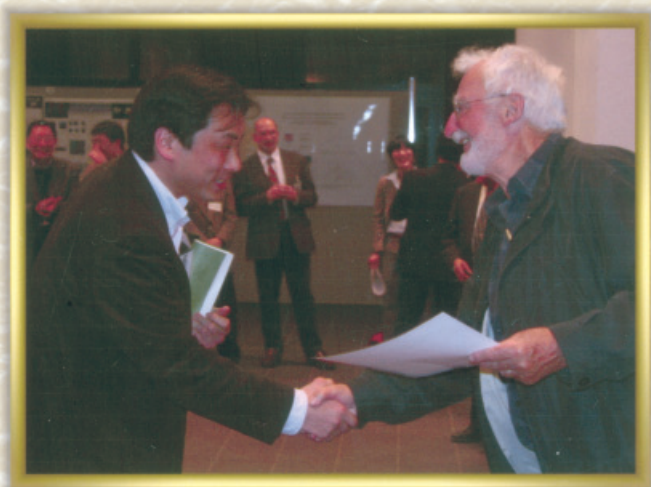
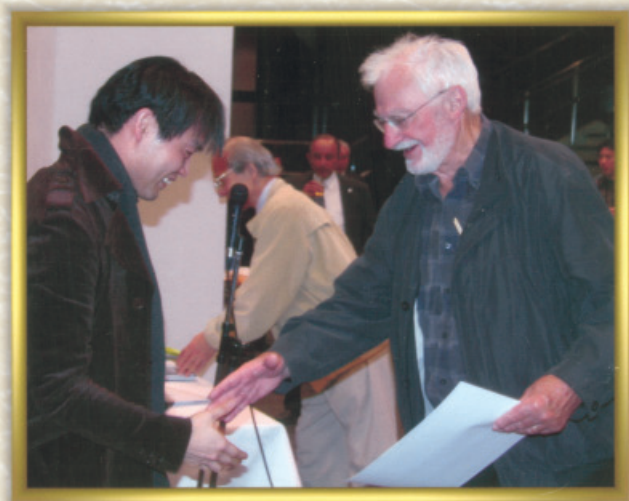


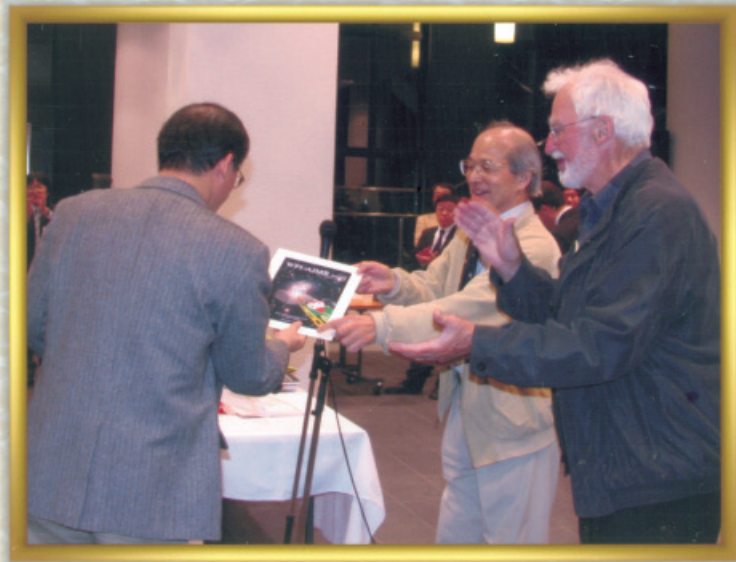










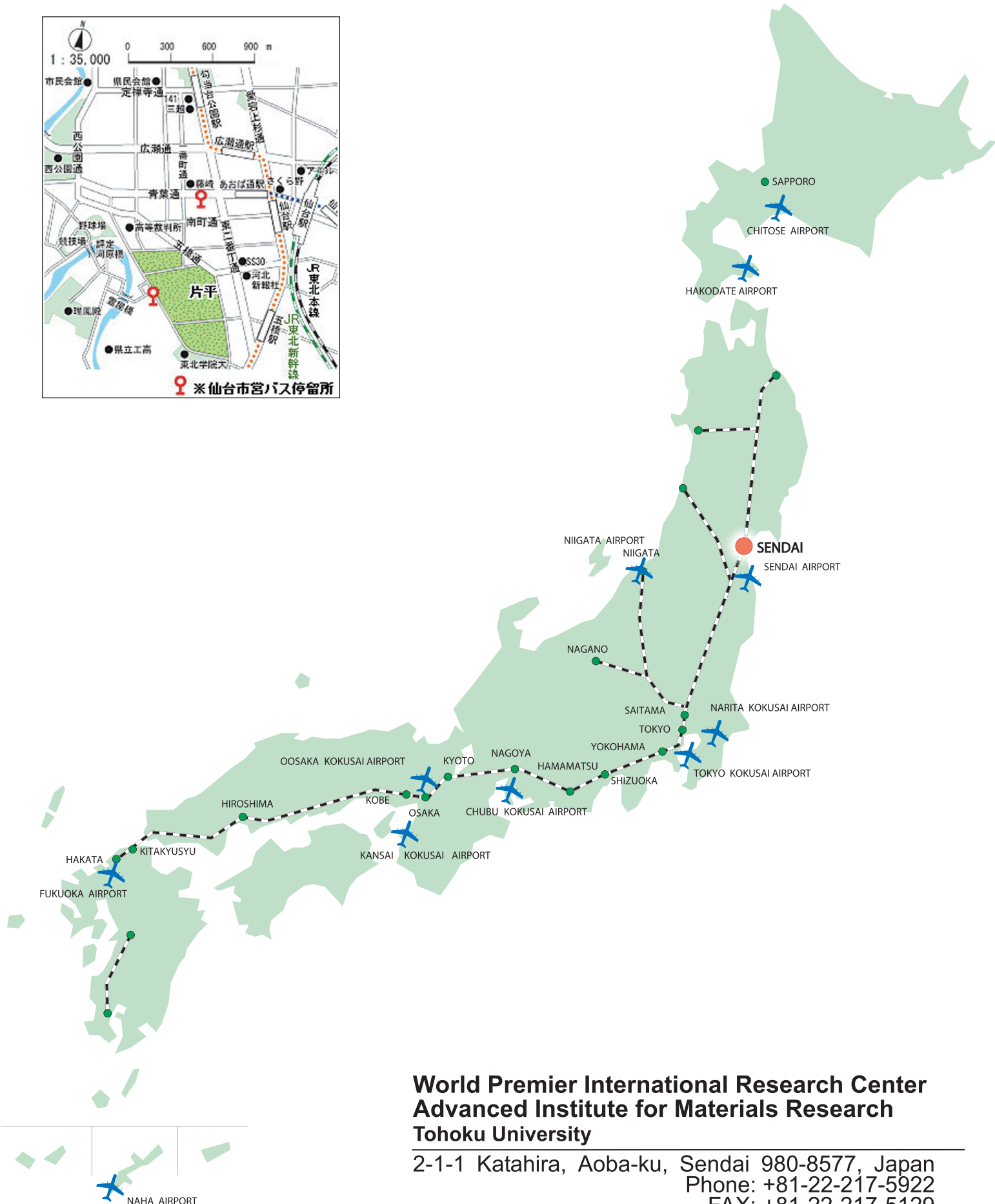












**World Premier International Research Center
Advanced Institute for Materials Research
Tohoku University**

2-1-1 Katahira, Aoba-ku, Sendai 980-8577, Japan
 Phone: +81-22-217-5922
 FAX: +81-22-217-5129
 E-mail : wpi-office@bureau.tohoku.ac.jp
 URL: <http://www.wpi-aimr.tohoku.ac.jp>



**World Premier International Research Center
Advanced Institute for Materials Research
Tohoku University**



2-1-1 Katahira, Aoba-ku, Sendai 980-8577

Japan

Phone: +81-22-217-5922

FAX: +81-22-217-5129